Scientific/Technical Report No. 420103

Proceedings of the
24th Scandinavian Symposium on
Physical Acoustics
Ustaoset 28 January – 31 January 2001
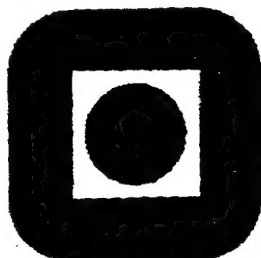
edited by
Ulf R. Kristiansen

NORWEGIAN UNIVERSITY OF SCIENCE
AND TECHNOLOGY
DEPARTMENT OF
TELECOMMUNICATIONS
ACOUSTICS

REPORT DOCUMENTATION PAGE

Form Approved OMB No. 0704-0188

1. AGENCY USE ONLY (Leave blank)	2. REPORT DATE June 2001	3. REPORT TYPE AND DATES COVERED Scientific/Technical Report

4. TITLE AND SUBTITLE

Proceedings of the 24th Scandinavian Symposium on Physical Acoustics Ustaoset 28 January – 31 January 2001

5. FUNDING NUMBERS

6. AUTHOR(S)

edited by: Ulf R. Kristiansen

7. PERFORMING ORGANIZATION NAME(S) AND ADDRESS(ES)

Norwegian University of Science and Technology
Department of Telecommunications
O.S. Bragstads plass 2B, N-7491 Trondheim   NORWAY

9. SPONSORING/MONITORING AGENCY NAME(S) AND ADDRESS(ES

Office of Naval Research, Ballston Centre Tower, 800 North Quincy Street Arlington, VA 22217-5660

10. SPONSORING/MONITORING AGENCY REPORT NUMBER

ISSN 1501-6773, June 2001

11. SUPPLEMENTARY NOTES

This work relates to the department of the Navy Grant N00014-1-1007 issued by the Office of Naval Research International Field Office. The United States Government has a royalty-free license throughout the world of all copyrightable material contained. 111 pages.

12a. DISTRIBUTION/AVAILABILITY STATEMENT

Approved for public release; distribution is unlimited.

12b. DISTRIBUTION CODE

ABSTRACT (Maximum 200 words)

The proceedings contain 18 of the presentations. They appear in the order they were presented during the symposium. A separate index for the papers has been added. There was no page limitation for the manuscripts.

BEST AVAILABLE COPY

14. SUBJECT TERMS

ONR, Navy, Scandinavia, Telecommunications, Acoustic propagation, Ultrasonic scattering, Reflection properties, Synthetic Aperture Sonar, Secondary grating lobe phenomenon, Acoustic streaming,

15. NUMBER OF PAGES

16. PRICE CODE

17. SECURITY CLASSIFICATION OF REPORT UNCLASSIFIED	18. SECURITY CLASSIFICATION OF THIS PAGE UNCLASSIFIED	19. SECURITY CLASSIFICATION OF ABSTRACT UNCLASSIFIED	20. LIMITATION OF ABSTRACT UL

NSN 7540-01-280-5500

Standard Form 298 (Rev. 2-89)
Prescribed by ANSI Std. 239-18
298-102

Scientific/Technical Report No. 420103

Proceedings of the
24th Scandinavian Symposium on
Physical Acoustics

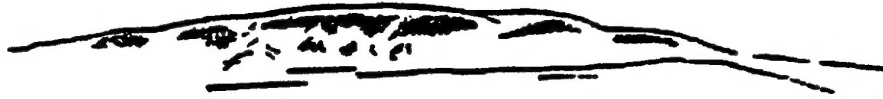Ustaoset 28 January – 31 January 2001

edited by
Ulf R. Kristiansen

Department of Telecommunications
Norwegian University of Science and Technology
O.S.Bragstads plass 2B, N-7491 Trondheim
Norway

24th Scandinavian Symposium on Physical Acoustics

Ustatoset 28 January – 31 January 2001

Preface

The Scandinavian Symposium on Physical Acoustics was held at Ustaoset, Norway in the period 28th of January to the 31st of January 2001. The meeting represented the 24th in a series of Scandinavian co-operation meetings in acoustics/hydrodynamics, and was arranged by the acoustics and optics group of the Norwegian Physical Society. The symposium was financially supported by the Office of Naval Research International Field Office (Navy Grant N00014-01-1-1007). For this we are most grateful. [*]

52 participants from Canada, Denmark, England, Lithuania, Sweden, the United States of America, and Norway attended the meeting. A total of 27 papers were presented. They covered a wide range of topics: underwater acoustics, new solutions to sound propagation problems, interaction of sound and porous media, non-linear acoustics, transducer technology, and applications of ultrasound in industry. The papers were presented in 5 oral sessions. The presentation time allowed for each presentation was 25 minutes.

A tradition in these symposia has been to leave some time around noon to go skiing, so also this year. The weather was good, and the nearby "løyper" and downhill slopes at Geilo offered possibilities at all levels of ambition. This, followed by lunch, allowed the participants to meet fresh for the afternoon sessions.

It is the aim of the organisers to attract students at master and doctoral levels to present their work. The Office of Naval Research International Field Office and The Norwegian Physical Society must be acknowledged for their financial support to students who attended the meeting.

The proceedings contain 18 of the presentations. They appear in the order they were presented during the symposium. A separate index for the papers has been added. There was no page limitation for the manuscripts.

The organisers would like to thank sincerely the speakers and participants for making the meeting an interesting and enjoyable event. Special thanks to the session chairpersons, who prevented the sessions to stray too far from the time schedule.

The Acoustics and Optics Group of the Norwegian Physical Society plans to organise a new meeting in the year 2002. This will be the 25th in the series! Invitations will be sent early in the autumn of 2001.

Ulf Kristiansen was the co-ordinator of the Ustaoset 2001 meeting.

Contents

24th Scandinavian Symposium on Physical Acoustics

Norlandia Ustaoset Hotell 28 January - 31 January 2001

A symposium sponsored by
OFFICE OF NAVAL RESEARCH INTERNATIONAL FIELD OFFICE

List of Participants

Andrew Baker CMR AS, Bergen,
andrew.baker@cmr.no

Helge Balk Dept. of Physics,Univ.of Oslo
helge.balk@fys.uio.no

Bjarte Berntsen, SIMRAD AS, Horten
bjarte.berntsen@simrad.com

Irina Bjørnø, Dept. Ind. Acoustics, TUD
ikb.utech@get2net.dk

Leif Bjørnø, Dept. Ind. Acoustics, TUD
prof.lb@get2net.dk

Helge Bodholt, SIMRAD AS, Horten
helge.bodholt@simrad.com

David Bradley, Pennsylvania State University
dlb25@psu.edu

Ivar Bratberg, , Dept. Telecommunications, NTNU
ivar.bratberg@fys.uio.no

Alex Cederholm, Royal Institute of Technology, Stockholm
alexc@fkt.kth.se

Eva Dalberg, FOA, Stockholm
eva.dalberg@sto.foa.se

Hefeng Dong, Dept. Telecommunications, NTNU
dong@tele.ntnu.no

Ellen Johanne Eidem, FFIBM, Horten
ellen-johanne.eidem@ffi.no

Rune Fardal Dept. of Physics, Univ. of Bergen
rune.fardal@fi.uib.no

David Farmer, Institute of Ocean Sciences, Canada
farmerd@dfo-mpo.gc.ca

Helge Fjellestad, IFI, Universitetet i Oslo
hfjelles@ifi.uio.no

Kjell-Eivind Frøysa, CMR, Bergen
kjellef@cmr.no

Karl Hjelmervik Dept. of Physics, Univ. of Bergen
karl.hjelmervik@fi.uib.no

Roy Hansen. Forsvarets Forskningsinstitutt, Kjeller
roy-edgar.hansen@ffi.no

Amir Hashemi, Bergen College, Dept. Eng., Bergen
amir.hashemi@hib.no

Viggo Henriksen, SINTEF, Trondheim
viggo.henriksen@informatics.sintef.no

Halvor Hobæk, Dept. of Physics, Univ. of Bergen
hobak@fi.uib.no

Lars Hole, Forsvarets Forskningsinstitutt, Kjeller
lars-r.hole@ffi.no.

Sverre Holm, IFI, Universitetet i Oslo
sverre@ifi.uio.no

Jens Hovem, Dept. Telecommunications, NTNU, Trondheim
hovem@tele.ntnu.no

Sven Ivansson, FOA, Stockholm
sveni@sto.foa.se

Vibeke Jahr, Dept. of Physics, Univ. of Oslo
vibeke.jahr@fys.uio.no

Trond Jenserud, Forsvarets forskningsinstitutt, Horten

trond.jenserud@ffi.no

Jarl Johnsen, Forsvarets forskningsinstitutt, Horten
jkj@ffi.no

Remi Kippersund, Dept. of Physics, Univ. of Bergen
remi.kippersund@fi.uib.no

Morgan Kjolerbakken, Dept. of Physics, Univ. of Oslo
morgan.kjolerbakken@fys.uio.no

Rolf Korneliussen, Institute of Marine Res., Bergen
rolf@imr.no

Kyrill Korolenko, Office of Naval Research, London
kkorolenko@onrifo.navy.mil

Ulf Kristiansen, Dept. Telecommunications, NTNU
kristian@tele.ntnu.no

Victor V. Krylov, Nottingham Trent University
victor.krylov@ntu.ac.uk

Nick Langhorne, Office of Naval Research, London
nlanghorne@onrifo.navy.mil

Torfinn Lindem, Dept. of Physics, Univ. of Oslo
torfinn.lindem@fys.uio.no

Even B. Lunde, SIMRAD AS, Horten
even.borten.lunde@simrad.com

Per Lunde, CMR, Bergen
per@cmr.no

Audun Pedersen, Dept. of Physics, Univ. of Bergen
audun.pedersen@fi.uib.no

Geir Pedersen, Dept. of Physics, Univ. of Bergen
geir.pedersen@student.uib.no

Jörgen Pihl, FOA, Stockholm,
jorgen.pihl@sto.foa.se

Arne Rønnekleiv, Dept. Physical Electronics, NTNU
arne.ronnekleiv@fysel.ntnu.no

Renaldas Raisutis, Ultrasound Institute, Kaunas Technical University, Lithuania
ulab@tef.ktu.li

Geir Helge Sandsmark, SIMRAD AS, Horten
geir.helge.sandsmark@simrad.com

Tore M. Skar, Kongsberg Offshore AS
tore.magne.skar@fmc.kos.no

Connie Elise Solberg, FFIBM, Horten
ces@ffi.no

Peter Svensson, Dept. Telecommunications, NTNU
svensson@tele.ntnu.no

Per Søderberg, FOA, Stockholm
per.soderberg@foa.se

Frank Tichy, SIMRAD AS, Horten
frank.tichy@simrad.no

Sigve Tjøtta, Fysisk Institutt Universitetet i Oslo
j.tjotta@wanadoo.fr

Magne Vestrheim, Dept. of Physics, Univ. of Bergen
magne.vestrheim@fi.uib.no

Morten Willatzen, University of Southern Denmark
willatzen@mci.sdu.dk

Program of the 24th Scandinavian Symposium on Physical Acoustics

Norlandia Ustaoset Hotell 28 january – 31 january 2001

The symposium is sponsored by

OFFICE OF NAVAL RESEARCH INTERNATIONAL FIELD OFFICE

Sunday 28 January

Arrival. Dinner is served from 19.00

21.15 Opening in the lecture hall

21.30 Meeting of the acoustics/optics group of the Norwegian Physical Society

Monday 29 January   Morning session

7.30 Breakfast

8:30 David Farmer, Institute of Ocean Sciences, Canada
     "Applications of high frequency acoustics to upper ocean physics"

9.00 David Bradley, Pennsylvania State University, USA
     "Propagation of sound through a complex bubble-filled media"

9:30

9.55 Coffee break

10.15 Halvor Hobæk[2], O.B. Johannessen[1] and Hanne Sagen[1],
      [1] Nansen Environmental and Remote Sensing Center, Bergen.
      [2] Department of Physics, University of Bergen.
      "AMOC - Stability of individual rays in the Fram Strait".

10.40 Eva Dalberg, Defence Research Establishment (FOA), Stockholm
      "Reverberation measurements and modelling in shallow waters".

11.05 Amir Hashemi, Bergen College Dept. Eng., Bergen
      " Acoustic propagation in ice-covered ocean"

11.30 Break, Lunch will be served from 13.30

Monday 29 January   Afternoon session

16.00 Victor Krylov The Nottingham Trent University, Nottingham, UK
    "Some wave propagation problems arising in theoretical modelling of ground vibrations
    from high-speed trains"

16.25 Hefeng Dong, Jens M. Hovem and Hans Olav Hygen
    Department of Telecommunications /Acoustics, NTNU, Trondheim
    "Poro-elastic effects in air and liquid saturated media"

16.50 Lars Hole, Norwegian Defence Research Establishment, Kjeller
    " A new project on acoustic and seismic modeling"

17.15 Coffee break

17.30 Viggo Henriksen[1], Morten Bjørhus[2] ,Ulf Kristiansen[3], and Gunnar Taraldsen[1]
    [1]SINTEF Telecom and informatics, Trondheim, [2]TTYL, Oslo
    [3]Department of Telecommunications/Acoustics NTNU
    "Numerical calculations of sound propagation over ground surfaces"

17.55 Ulf Kristiansen, Karim Jezzine, and Hefeng Dong
    Department of Telecommunications/Acoustics NTNU
    " Transmission Line Modelling of the Granåsen experiment"

18.20 Break, Dinner at 19.15

Tuesday 30 January   Morning session

7.30 Breakfast

8:30 Helge Bodholt, SIMRAD AS, Horten
    "Split-beam transducer with 3 sections"

8:55 Rune Fardal and Magne Vestrheim, Department of Physics, University of Bergen
    "Analyses of electric measurements on piezoelectric disks using FE modeling."

9.20 Andrew Baker, Kjell-Eivind Frøysa and Per Lunde
    Christian Michelsen Research AS, Bergen.
    "Ultrasonic scattering from liquid droplets in a wet gas"

9.45 Coffee break

10.00 Morten Willatzen MCI; University of Southern Denmark
    "Ultrasonic reciprocal transducer systems and flow measurement"

10.25 Renaldas Raisutis and Liudas Mazeika..
    Ultrasound Institute, Kaunas Technical University, Lithuania
    "Modelling and imagining echoes from complex geometry objects".

10.50 Alex Cederholm, MWL, Royal Institute of Technology, Stockholm
"Acoustic transmission and reflection properties of Alberich anechoic coatings"

11.15 Break, Lunch will be served from 13.30

Tuesday 30 January   Afternoon session

16.00 Jörgen Pihl, FOA, Stockholm
"Mine Classification by Synthetic Aperture Sonar"

16.25 Even Borten Lunde SIMRAD AS; Horten
" The Dream Sonar - A Dream Only? : PN-Coded Signals and SAS (in Bistatic Minehunting) "

16.50 Roy Edgar Hansen, Norwegian Defence Research Establishment, Kjeller
"SENSOTEK: Development of a Synthetic Aperture Sonar for AUV"

17.15 Coffee break

17.30 Sigve Tjøtta, Fysisk Institutt, Universitetet i Oslo
"On the theory of sound waves of finite amplitude in fluids."

17.55 Helge Fjellestad and Sverre Holm: Institutt for informatikk, Universitetet i Oslo
"Simulation of nonlinear fields from 2D ultrasound transducers and a new secondary grating lobe phenomenon"

18.25 Geir Pedersen and Halvor Hobæk, Department of Physics, University of Bergen
"Single burst acoustic streaming".

18.50 Break, Dinner at 19.15

Wednesday 31 January   Morning session

7.30 Breakfast

9.00 Rolf Korneliussen, Institute of Marine Research, Bergen
"Application of acoustic signatures of biological scatterers II".

9.25 Kjell-Eivind Frøysa and Per Lunde, Christian Michelsen Research, Bergen
"A ray theory approach to investigate the influence of flow velocity profiles on transit times in ultrasonic flow meters for gas and liquid"

9.50 Sven Ivansson[1] and Judith Bishop[2]

[1] Defence Research Establishment (FOA), Stockholm,
[2] Naval Undersea Warfare Center (NUWC) Newport, Rhode Island USA
"Leaky-mode and Wavenumber-integration Representations of Grazing-ray Diffraction"

10.15 Coffee break

10.25 Irina Bjørnø and Leif Bjørnø, Department of Industrial Acoustics, TUD, Lyngby
"Practical applications of resonance vibrations of liquid-filled cylinders."

10.50 Peter Svensson and Asbjørn Krokstad,
Department of Telecomminications/Acoustics NTNU, Trondheim
"Sound radiation from unbaffled loudspeakers"

11.15 Closing, Lunch is served from 12.30

AMOC - Stability of individual rays in the Fram Strait

H. Hobæk[1,2], O.M. Johannessen[2], H. Sagen[2], T. Hamre[2]
[1]Department of Physics, University of Bergen, Norway
[2]Nansen Environmental and Remote Sensing Center
Edv. Griegsv. 3A, N-5059 Bergen, Norway
e-mail: halvor.hobak@fi.uib.no

Introduction

The objective of the research project "Acoustic Monitoring of the Ocean Climate in the Arctic" (AMOC)[1] is to investigate the possibility of using acoustic methods to monitor temperature and ice thickness in the Arctic Ocean on a long term basis, with great relevance to global warming. Since main influx/efflux of water (and heat) to the Arctic Ocean is through the Fram Strait, monitoring the temperature distribution and water flux in the Fram Strait is an important issue in this respect. In this presentation we focus on certain aspects of acoustic thermometry using ray tracing. In order to apply acoustic means for monitoring temperature and flux of water masses it is essential to be able to identify arrival of individual rays at the receiver location, while the environment undergoes seasonal and shorter time scale variations. The present study is based on ray simulations using environmental data for the period 1950-1990 in terms of decadal means separated in winter (January - March) and summer (May-July) seasons. In addition a detailed data set of one passing meso scale eddy was used. The method applied is analysis of "ray fans" obtained by launching a large number of rays in a narrow fan centered about the horizontal. The main conclusion is that some rays may be identified most of the time, even during passing eddies.

Fram Strait Environment

The environmental data used in this project is prepared from the Joint US-Russian Arctic Oceanography Atlas CDs [2] and is gridded for the Fram Strait in 9 stations separated by about 2.8 degrees along the 79° N latitude, covering the longitude 11° W to 11° E. About 200 km of the 600 km wide Fram Strait between Greenland and Spitzbergen at 79° N is more than 2000m deep. The bathymetry of the strait is shown in Fig. 1, with an interpolated color map of the mean sound speed for the summer seasons 1950-1989. The width of the strait allows influx of warm water to the Arctic Ocean and outflux of cold water and ice to be separated horizontally, with the warm water flowing northwards on the Spitzbergen side and cold water flowing southwards on the Greenland side, which is ice- covered almost all year round. This results in strong horizontal sound speed gradients in addition to vertical, as clearly seen in Fig. 1. Here Greenland is at the left and Spitzbergen at the right hand side, and the origin is placed at 11° W. The seasonal variations occur mostly in the upper 600 m of the water column. From an acoustical point of view the Fram Strait is an extremely difficult environment to monitor because of the two opposing currents which is displaced horizontally. In this study we have therefore focussed on placing the sound source in the middle of the strait, and a receiver array on the the eastern flank near Spitzbergen. In the examples shown the source is located at 250 km, and the receiver at 410 km. Because of the the sound ducts which appear in the upper layers it is necessary to lower the source to 300 - 500m depth - in the examples shown 500m. The averaged environmental data contain no information of short term variations like passing meso scale eddies (time scale weeks), tidal currents or internal waves. In order to model a passing eddy data from the AOGC expedition in 1997 [3] has been used in combination with the averaged environmental data.
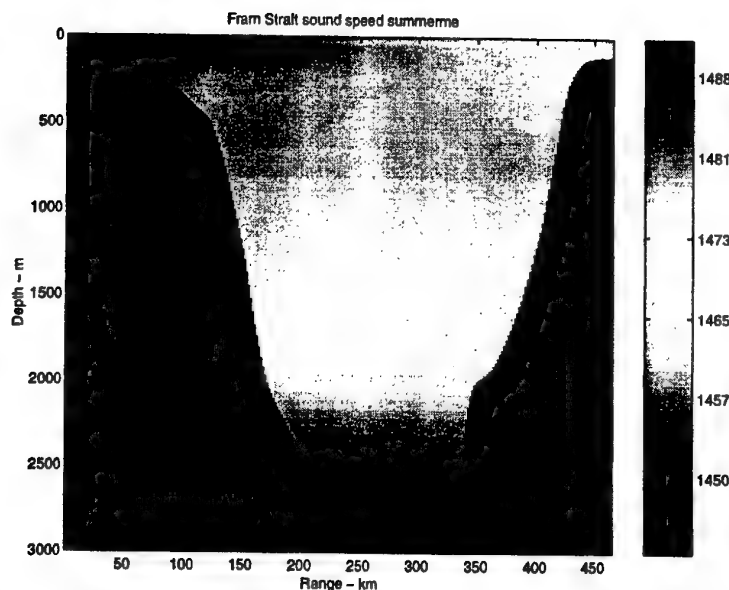
Figure 1: Bathymetry and summer mean sound speed map of the Fram Strait

Ray fans

A preliminary study was made by using the ray tracing code "RAY" [4] to search for "eigenrays" between the source and a receiver at 300m depth. For the different seasons and decades the number of eigenrays varied between 2 and 14. A study of the eigenray signatures, determined by launch angle, number of top and bottom bounces and angle at receiver, revealed a marked difference between summer and winter seasons, and a rather confusing pattern emerged. In order to investigate this further a different approach was taken. Instead of searching for eigenrays a large number of rays (1200) was launched within a narrow angle interval about the horizontal (ray fan), and the depth and travel time at the receiver range was recorded. Only rays actually reaching the receiver range was kept. A plot of the ray fan for summer 50s is shown in Fig. 3 as ray depth at receiver against source angle (negative angles point downwards), Fig. 4 as travel time against source angle and Fig. 5 as depth against arrival time (these are 3 projections of a 3-D curve in the space: source angle, ray depth and travel time - a 3-D plot is interesting, but does not really reveal important new information).

Each ray arrival is plotted as a circle, and the density of these represent the intensity of the sound. The horizontal line indicates a receiver at 300m depth. It's intersections with the curve identifies the eigenrays for this receiver. The eigenray algorithm in RAY found 5 eigenrays, corresponding to the densest intersections. Do observe that in the "depth against time" plot, Fig. 3, the deepest rays are the last to arrive! This is found to be the case in general (with only one exception), and is contrary to ordinary sound channel behavior. The fastest rays - in most cases a narrow ray fan launched almost horizontally (in Fig. 3 -1° to +0.5 °) - propagate in a narrow, undulating band about an almost straight line from the source to the receiver, which is reached at depths varying from 800 m to 50 m. The case summer 50 is shown in Fig. 5. Thus, these rays seem to follow the range dependent sound channel axis. The reason why they are the first to arrive must be due to the path length being as much shorter than for the deeper rays that it compensate for the lower sound speed.

Ray fans plotted as in Fig. 2-4 are helpful for investigating stability of eigenrays. As seasons and decades vary the patterns are deformed and shifted - a really bad case of such deformation is shown in Fig. 6, for winter 60s. Here the eigenray algorithm in RAY found only 2 eigenrays (it turns out that in this case the ray fan looks more normal if the source is shifted to shallower depths, 300-400m, but then the deepest rays penetrate only down to 600m).

In an attempt to obtain a stable reference frame for the ray fan results Fig. 7 shows a "generic plot" of this type, obtained by disregarding range dependence (using the sound speed profile at the source) for summer 60.

Evidently, the ray fan is rather symmetric about zero source angle, and shows 3 undulations to each
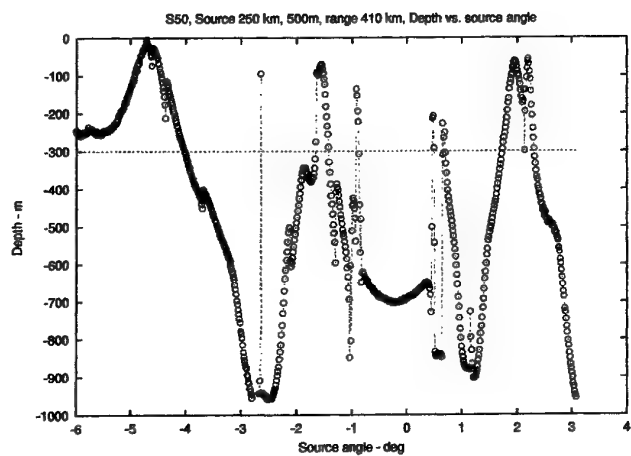
Figure 2: Ray fan results for summer 50s - Depth against source angle.
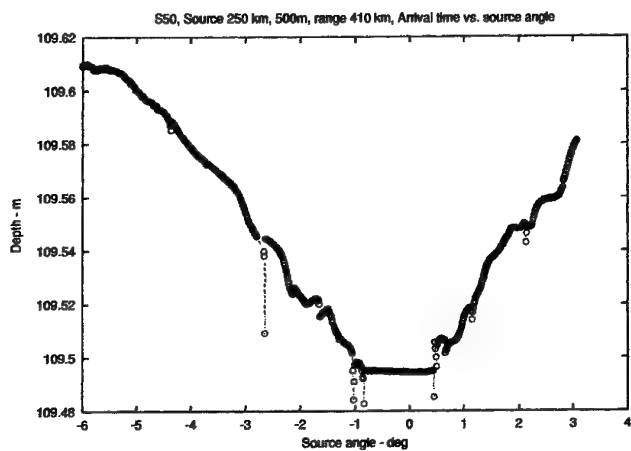

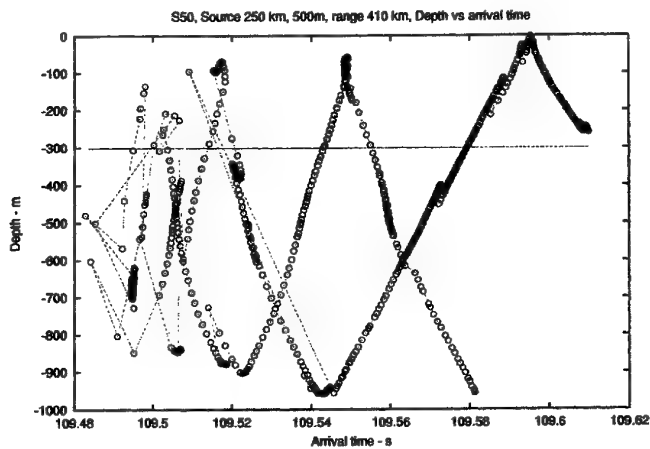Figure 3: Ray fan results for summer 50s - Travel time against source angle.

Figure 4: Ray fan results for summer 50s - Depth against travel time.
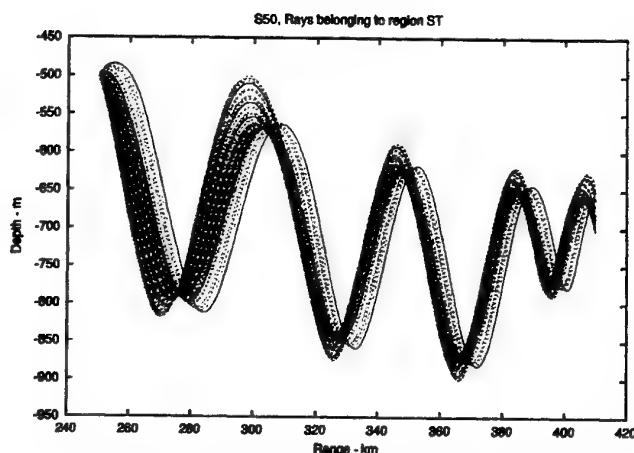
3

Figure 5: Trace of fastest rays, summer 50

side. These are narrowly peaked at the top and wider at the deep end. The outer flanks fall off steeply towards depths about 1 km. As seasons vary both amplitudes and widths of these undulations fluctuate, in particular in the region ±2°, and sometimes they are severely deformed (in Fig. 2 the rightmost undulation is actually No 2, not 3). The pattern may be shifted upwards or downwards, and some undulations may merge (in particular the central ones) or split. The trend emerging from such analysis is that the rays belonging to the outer flanks are the ones most likely to be recognizable at all times, while those launched more horizontally are less stable. Also, since the stablest rays are also the deepest, they are the most promising candidates for acoustical thermometry in the Fram Strait. For convenience these eigenrays are labeled "a,b"and "g,h", where a and h are on the outermost flanks, and b and g on the inner side of the outer undulations (in Fig. 2 only eigenray "b" is present, near −4° source angle). In Fig. 8 is shown traces of these eigenrays for all seasons (source depth 500m, receiver depth 300m). They cover the water column down to 1 km and more, and thus the dominating part of the West Spits-bergen Current.

The ray fan plots also show that one should have receivers at several depths, in order to increase the probability of finding stable eigenrays - if they fail at one depth for a period there would be some at other depths, and *vice versa*.

In order to demonstrate the sensitivity of acoustic thermometry based on the stable rays the travel times of these rays are shown in Fig. 9. There is a marked difference between summer and winter seasons; typically about 100 ms faster in the summer. Therefore the seasons are separated in the figure. Note that ray h is missing in all summer seasons. The eigenrays show basically the same trend: Slightly decreasing travel times with time, and more pronounced at the later decades. The change is small, however: Winter rays arrive 31±2ms earlier in 1980s than in 1959s, corresponding to an increase in sound speed 0.42±0.03 m/s, or an increase in temperature of roughly 0.09°C. Inversion based on details of the ray paths has not yet been performed.

Meso scale eddies

The original sound speed data for one meso scale eddy taken by the 1997 AOGC expedition [3] is shown in Fig. 10. This data set was incorporated into the environmental data in the following way. First, sound speed data was interpolated on a regular grid horizontally and vertically in terms of sound speed differences (global mean = zero). Secondly, margins were added to both sides and bottom with tapered sound speed differences, in order to avoid artifacts due to discontinuities. Finally the data set was merged onto the environmental data sets (added), with an amplitude factor adjustable between 0 and 1. In this way one could to some extent simulate a passing eddy.

As the meso scale eddy is increased the ray fans become distorted, first near zero source angle, later also on the outer undulations. An example is shown in Fig. 11 for maximum meso amplitude, summer 60. The pattern tends to become chaotic, and the number of eigenrays can become very high, but with forbiddingly low amplitude. However, the "stable" eigenrays, a,b,g and h turn out to be less influenced
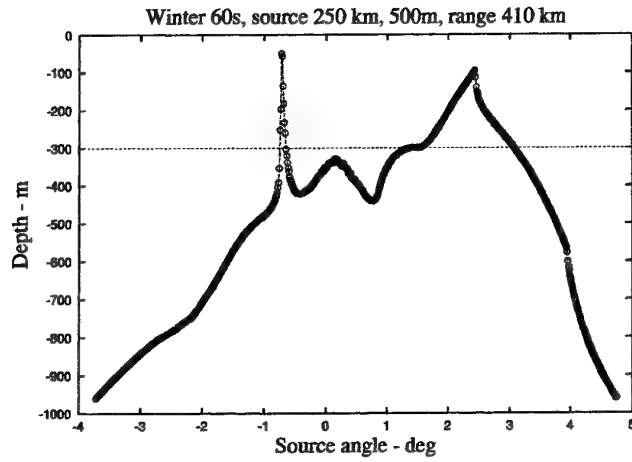
Figure 6: Ray fan winter 60, depth against source angle
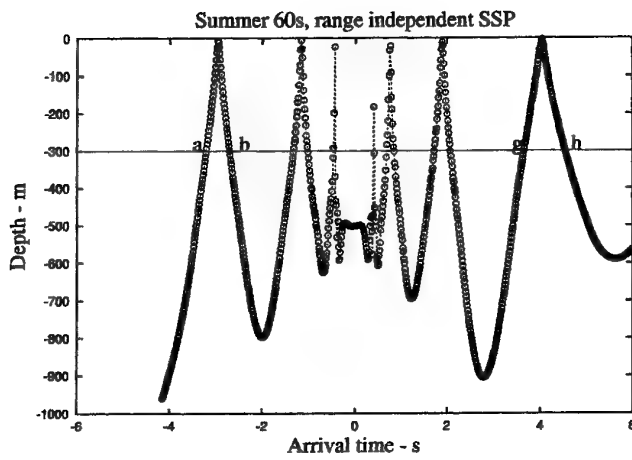
Figure 7: Ray fan summer 60, no range dependence
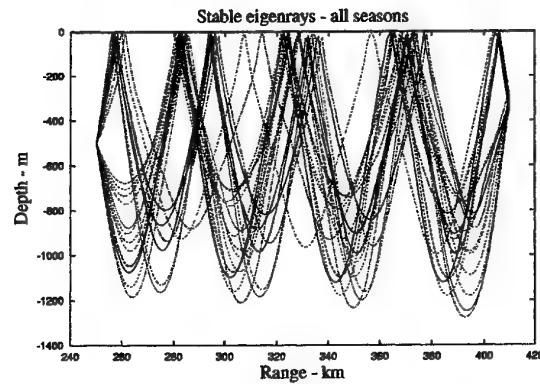
Figure 8: Trace of "stable" rays through all seasons

5
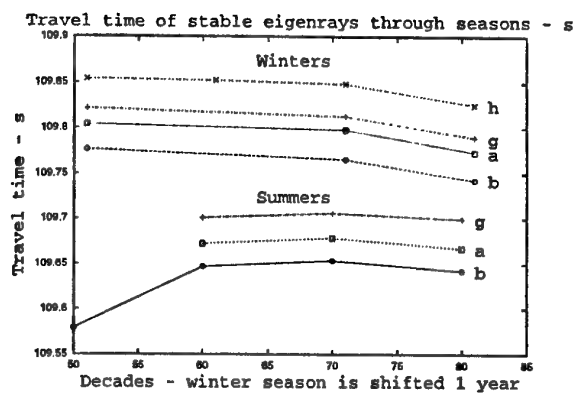
Figure 9: Travel time of "stable" rays through all seasons
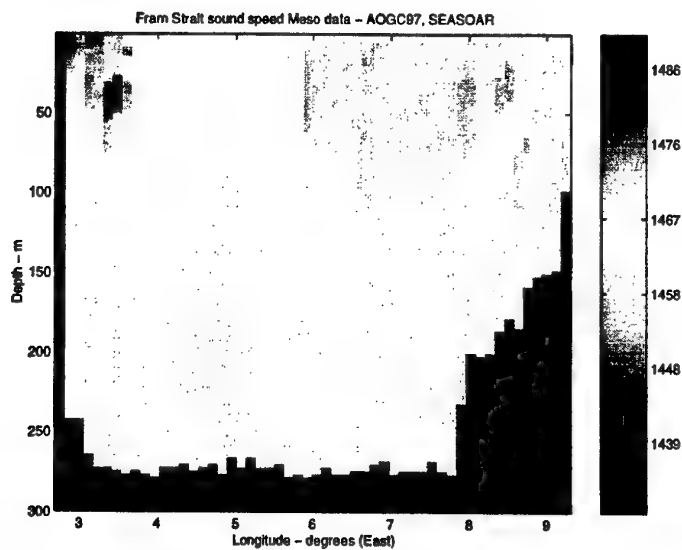
Figure 10: Map of the ssp-data for the meso scale eddy.

than the rest, and are therefore promising candidates for eigenrays for acoustical thermometry in a future experiment.
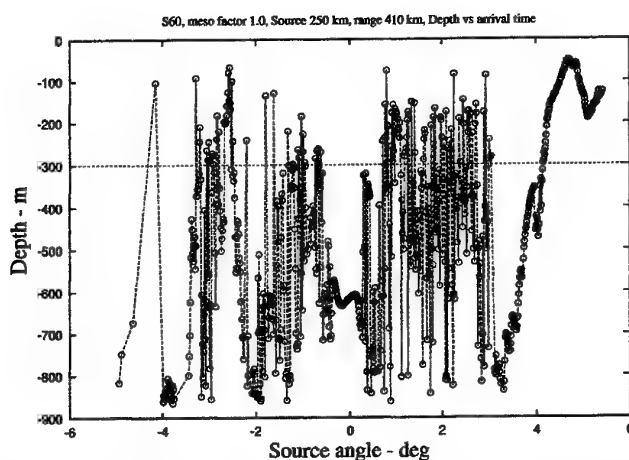
Figure 11: Ray fan meso factor 1, summer 60, depth against source angle

Conclusions

Ray fan analysis is a valuable tool for assessing eigenray stability. The steepest, deepest going rays are the most promising candidates for acoustic thermometry in the Fram Strait over a prolonged period.

References

[1] O.M. Johannessen, H. Sagen, H. Hobæk,"Acoustic Monitoring of Ocean Climate in the Arctic",*in Proc. 23rd Scandinavian Symposium on Physical Acoustics, Ustaoset, Norway, 30 Jan. - 2 Feb. 2000,* pp. 1-2, ed. U. Kristiansen, Scientific/Technical Report No. 420003, ISSN 1501-6773, Department of Telecommunications/Acoustics, NTNU, Trondheim, Norway.

[2] The Joint US-Russian Atlas of the Arctic Ocean is available from: User Services, National Snow and Ice Data Center, University of Colorado, Campus Box 449, Boulder, CO 80309-0449, USA. URL: http://www-nsidc.colorado.edu.

[3] O.M. Johannessen, V.J. Haugen, "AMOC 1997. Seasoar and CTD data in the Fram Strait". NERSC special report no 62.

[4] J.B. Bowlin, J.L. Spiesberger, T.F. Duda and L.F. Freitag, "Ocean Acoustical Ray-Tracing Software RAY", Tech. Rep. WHOI-93-10, Woods Hole Oceanographic Institution, Woods Hole, Mass. USA, 1992, 49 pp.

Reverberation Measurements and Modelling in Shallow Waters

Eva Dalberg*, Lena Frenje, Sven Ivansson & Bernt Nilsson

Swedish Defence Research Agency (FOI), Division of Systems technology, 172 90 Stockholm, Sweden
* Corresponding author, eva.dalberg@foi.se

Abstract

A field trial has been conducted in the Stockholm Archipelago in the Baltic Sea with the objective of investigating the influence of the waveform on the reverberation level. The performance of three LFM pulses of different frequency content and bandwidth and one 20 kHz CW pulse was compared after matched filter processing. The more broadband signals have, as expected from theory, a lower reverberation level. A simulation study was also performed and the agreement between experimental data and the model is satisfactory for ranges up to a few hundred meters, above which the received levels were below the noise floor of the experiment.

Shallow water reverberation

Active sonar performance is often reverberation limited in shallow waters. In the Baltic Sea a common bottom type consists of bedrock covered by soft sediments of varying thickness. The sediment can be penetrated by signals, especially of low frequency, and be reflected either in sediment layer boundaries or in the sediment-bedrock interface. The limited depth of the Baltic Sea enhances the reverberation level experienced in active sonar applications. To maximize the performance of active sonar systems, relatively high frequencies have traditionally been chosen for Baltic Sea applications.

In general, there are several parameters that have impact on the reverberation level. Some are due to the environment. This includes the bottom topography and the bottom type of the site, and the sound speed profile. There are also sonar parameters that are important, such as the lobe width. This work is a study of how the waveform, especially the pulse length, influences the reverberation level. Since we use a matched filter when processing our data, the pulse length is determined by the signal bandwidth. A field trial was conducted in a shallow bay in the Stockholm Archipelago and the measured reverberation levels from a few pulse types have been compared with a theoretical model. More details about this work is found in [1].

Field trial

The field trial was conducted in May 2000. The experiments were carried out at FOI's permanent field laboratory situated in the southern part of the Stockholm Archipelago. At this site there is a floating platform from which the transmitter was deployed. Around the transmitter a ring with six receiver hydrophones was mounted. This means that the measurements were carried out in monostatic mode. The transmitter, a TOPAS 120 from Simrad, has a narrow lobe width, typically 4 degrees at the frequencies used. The lobe width has a weak frequency dependency, and is narrower for higher frequencies. The source level of this parametric sonar is rather low, around 190 dB re 1 μPa at 1 m distance at the frequencies used. In this frequency range the ring of receiver hydrophones has an almost omni-directional response. For more details on the equipment, see [1]-[2] .

The transmitter and receiver hydrophones were kept at a depth of 1.3 m throughout the measurements. The tilt angle of the transmitter and receiver was varied from 1 degree upwards to 10 degrees downwards. Horizontally, a sector spanning 60 degrees was covered. This sector contains some variation in the bottom topography, and the influence of this was probed. The bottom type can be considered constant in the field trial area, and it consists of a smooth clay-covered seabed.

In active sonar applications it is the received signal to reverberation level that decides the performance. To have known target echoes to compare the reverberation levels with, two corner reflectors of 0.5 m dimension were deployed. One was at a distance of 100 m from the transmitter/receiver, while the second one was placed at about 330 m range. The echo from the latter reflector was in most cases too weak to be observed.

The measurements were carried out during three days with some variations in the sound speed profile. While the profile was downward refracting during the first two measurement days, it changed into iso-velocity the last. The day to day variations in the sound speed profile had a larger impact on the measured reverberation levels than the ones due to variations in the horizontal angle, and thus the seabed topography.
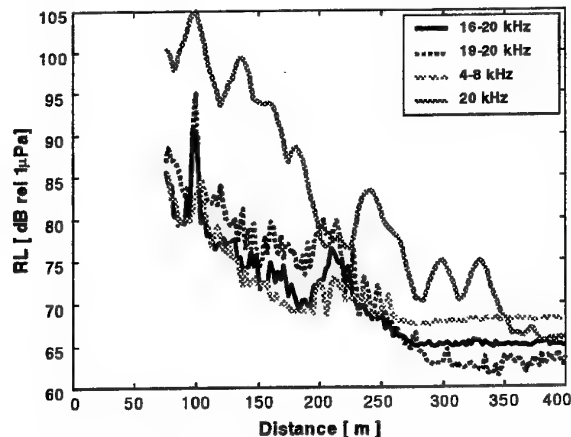
Figure 1: Received reverberation levels for the four pulse-types used in this study. The two-way travel time has been translated into an equivalent distance from the transmitter/receiver. This figure shows the combined result from all tilt angles when the transmitter/receiver was aimed towards the closer corner reflector, in total about 200 pings per pulse.

Figure 2: A close view of the echo from a corner reflector deployed to study the echo to reverberation level for the different waveforms.

Analysis of the data

The expected bottom reverberation level is proportional to the bottom area insonified by the emitted pulse [3]. This area depends on the beam width, the range, the sound speed and the pulse length. There is thus a proportionality between the received reverberation level and the pulse length, τ. The recorded data set was analysed using a matched filter, i.e. a synthetic replica of the transmitted signal was correlated with the received echoes. This process means a pulse compression in time with a factor $B\tau$, where B is the bandwidth of the emitted pulse. The result is a decrease of the reverberation level with a factor $10\cdot\log_{10}(B\tau)$. In other words, the expectation is that a wider bandwidth will have a shorter effective pulse length after the matched filter, and this will decrease the reverberation level. To investigate this hypothesis empirically, we used a few different pulses: one monofrequency (CW) 20 kHz signal, and three linear frequency modulated (LFM) pulses of varying frequencies, 4-8 kHz, 16-20 kHz and 19-20 kHz. The result of the measurements is summarized in Figure 1.

From this figure, the expected behaviour is verified. The broadband signals have less reverberation than the narrowband- and monofrequency pulses. The difference between the pulse with a bandwidth of 1 kHz and the ones with 4 kHz bandwidth is about the expected value, 6 dB.

The early part of the received pulse is not shown, since the receiving hydrophones were mounted immediately around the parametric sonar, and were saturated while the pulse was transmitted. The omitted part is slightly longer than the pulse length to avoid erroneous results.

The echo from the close corner reflector is clearly visible in Figure 1. This echo is also shown in Figure 2.
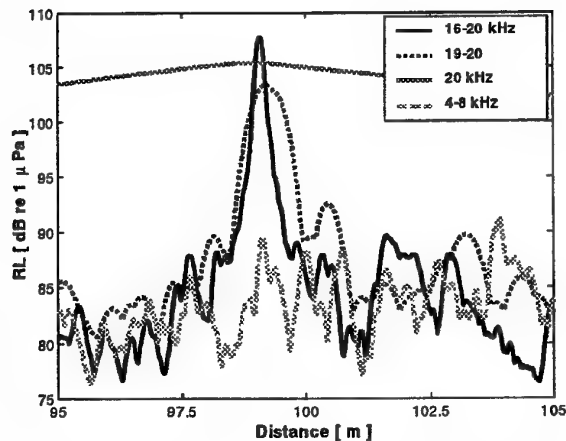
The best echo to reverberation ratio is achieved with the 16-20 kHz LFM pulse, with its narrow pulse width after the matched filter. The 4-8 kHz LFM pulse does not resolve the target. This is because the wavelength of that pulse is of the same order as the dimension of the target.

Comparison with a theoretical model

A two-dimensional ray-based model, SLOPERVB, has been used for this study. It is based on the model BIRVB [4], with the extension that range-dependent bottom topographies can be studied. The model is described in [1]. The depth profiles used in the simulations varied with the bearing angle of the transmitter/receiver. Other important environmental parameters that were adjusted to the actual experimental situation are the sound speed profile (range independent) and the bottom impedance (a value of $1.9\cdot10^6$ kg/m³ was found to be suitable).

The backscattering at the bottom was modelled following Lambert's law,

$$SS = 10\cdot\log_{10}\mu + 10\cdot\log_{10}(\sin\Theta_1\cdot\sin\Theta_2)$$

where SS is the scattering strength when the grazing angles for incidence and scattering are Θ_1 and Θ_2. The value for to the scattering strength that was found to produce the best agreement with the measured data was

$$10\cdot\log_{10}\mu = -17\text{dB}$$

It is also in agreement with other more detailed studies of the backscattering strength at the site [5].

The sonar has a lobe width with some frequency dependency, and this was considered in the computer

9
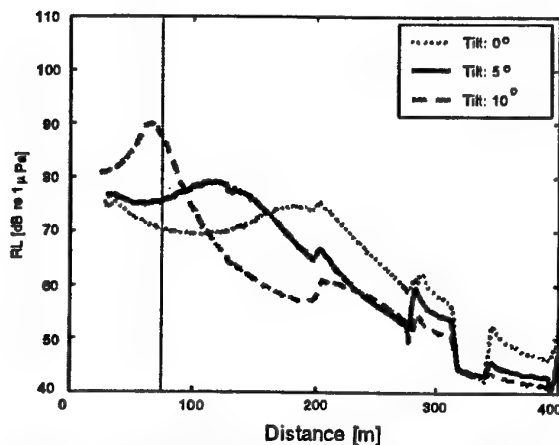
Figure 3 : Reverberation levels for the 16-20 kHz LFM signal, according to the model for three tilt angles of the transmitter/ receiver ring.
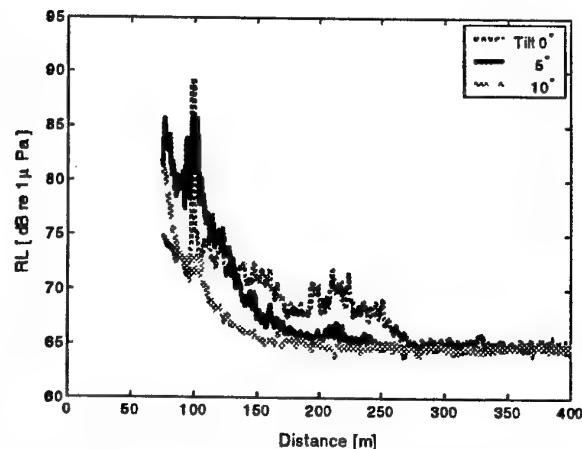
Figure 4 : Similar to Figure 3 but with experimental data. Please note that the scales are different in Figure 3 and Figure 4.

modelling. Since the results from the model are compared with data after a matched filter, the pulse length was determined by the bandwidth of the modelled pulses.

Figure 3 shows some modelling results. The pulse is a 16-20 kHz LFM pulse and the tilt angle of the transmitter/ receiver has been varied. The result can be compared with Figure 4 which shows experimental data under similar circumstances. The agreement is satisfactory, and there are some common features in the curves. Please note that the experimental data contain an echo from a corner reflector, and this was not modelled. For larger ranges, i.e. late arrival times, the model predicts lower levels than the noise floor in the experiment, and no comparison between experiment and model can be made. The absolute levels are also compatible with each other.

Conclusions

A field trial designed to study how reverberation depends on signal bandwidth has been conducted. The data have been analysed using a matched filter and the results are consistent with the theoretical expectations; LFM pulses with 4 kHz bandwidth give less reverberation than the 1 kHz bandwidth case. Data has also been compared with a model, SLOPERVB, and for ranges up to a few hundred meters the agreement is satisfactory. For longer ranges no comparison was possible to do, since with the present source the received reverberation levels were below the noise floor of the experiment. The agreement between the model and the data is encouraging and opens up the possibility to do simulation studies and comparisons of reverberation levels from other types of broadband signals in the future, such as binary phase shift keying (BPSK) signals as an example.

References

[1] Dalberg, E., Frenje, L., Ivansson, S. & Nilsson, B., Measurements and modelling of Shallow Water Reverberation, FOA-R—00-01751-409—SE
[2] Dalberg, E., Levonen, M., Nilsson, B., Olsson, M., Pihl, J:, & Söderberg, P., *Geoacoustic Sediment Properties in the Baltic*, FOA-R—00-01466-409—SE
[3] Urick, R.J., *Princpiples of Underwater Sound*, McGraw-Hill, 1983
[4] Ivansson, S., *Shallow-water reverberation computations for bistatic geometries*, FOA-R—98-00796-409—SE
[5] Levonen, M, Ivansson, S:, More'n, P., & Söderberg, P., *Bottom scattering in shallow water, measurements with a parametric sonar*, FOA-R—99-01359-409—SE

A study on acoustic propagation
in the ice-covered region of the Arctic Sea

Amir Hashemi

Department of Engineering, Bergen University College, Bergen, Norway

Abstract

The results of a numerical investigation of the acoustic propagation in the ice-covered region of Arctic Sea where the environment can be considered range-independent are presented. Environment parameters are motivated from measurements from Greenland Sea during Marginal Ice Zone Experiment, MIZEX [4].

1 Introduction

Numerical modeling of acoustic propagation in the ocean has been in continuous development throughout the last two decades. Before the early 1970, ray theory was applied for solving propagation problems in underwater acoustics, which is a computationally efficient but based on high frequency asymptotic approximation. Since early 1970 there has been an enormous expansion in computer science and this progress has stimulated acousticians to develop frequency dependent solutions for wave equation. In these numerically based techniques wave equation is solved by normal mode, fast field, and parabolic equation methods [3] . This has made it possible to compute the acoustic field in complex ocean environments.

Hydrological measurements in the Marginal Ice Zone (MIZ) of the Greenland sea reveals the need of range-dependent models in the ice edge zone, whereas a range-independent horizontal layered model can be used in ice covered regions. In this paper, the focus is on the ice-covered region of the Arctic. SAFARI numerical code [2] provides accurate transmission loss values for propagation in range-independent multi-layered horizontally stratified environments and was therefore a useful tool for this investigation.

First solution of wave equation for a range-independent environment is presented and mathematical equations for Green's function and normal stress are given for a 3 layered environment (vacuum-solid-fluid-fluid halfspace) in Sec. 2 and a numerical example (case 1) is presented to study a deep ice-covered sea, 3 other numerical examples study more complicated environments in Sec. 3. SAFARI was applied for simulations. A summary ends the discussion in Sec. 4 in which some comments are given about SAFARI.

2   Mathematical basic equations for a 3 layered model

By employing forward Fourier and Hankel transform respectively on the linear wave equation in a range independent environment , the *depth-separated* wave equation can be obtained [2]:

$$[\frac{\partial^2}{\partial z^2} - (k^2 - k_m^2(z))]G(k,z) = \frac{F(z)}{2\pi}.$$ (1)

Where k_m is medium wavenumber and $F(z)$ is forcing term. The total solution of the depth-separated equation can be expressed as a superposition of a homogeneous solution G_H, satisfying boundary conditions, and a particular solution G_P, the free field produced by a source in an unbounded medium. $G_P(k,z)$ term is added to the homogeneous solution in layers containing one or more sources:

$$G(k,z) = G_H(k,z) + G_P(k,z).$$ (2)

$G_H(k,z)$ is found by using the boundary conditions. To find the total field at any range r and the time response, we apply inverse Hankel transform.

$$g(r,z) = \int_0^\infty G(k,z)J_0(kr)kdk,$$ (3)

where J_0 is the Bessel function and k is the horizontal wavenumber.
The normal stress τ_{zz} is then given by:

$$\tau_{zz} = -\rho\omega^2 g(r,z)$$ (4)

where ρ the fluid density , ω the radial frequency and $g(r,z)$ is the potential field.

In this paper $G(k,z)$ and τ_{zz} are studied. To investigate the acoustic propagation in the ice-covered region a 3 layered model is considered (vacuum, solid, fluid, fluid half-space).

The integral representation of the homogeneous solutions in the layer 1 can be expressed as :

$$g_{l1}(r,z) = \int_0^\infty [A_1^-(k)e^{-\alpha_1 z} + A_1^+(k)e^{\alpha_1 z}]J_0(kr)kdk,$$ (5)

where $A_1^-(k)$ and $A_1^+(k)$ are the amplitudes of the upgoing and downgoing compressional field in the layer 1 and

$$\alpha_1 = \begin{cases} -\sqrt{k^2 - k_1^2}, & k > k_1, \\ i\sqrt{k^2 - k_1^2}, & k \leq k_1. \end{cases}$$

$$g_{s1}(r,z) = \int_0^\infty [B_1^-(k)e^{-\beta_1 z} + B_1^+(k)e^{\beta_1 z}]J_0(kr)kdk,$$ (6)

$$where \;\; \beta_1 = \begin{cases} -\sqrt{k^2 - k_s^2}, & k > k_s, \\ i\sqrt{k^2 - k_s^2}, & k \leq k_s, \end{cases}$$

$B_1^-(k)$ and $B_1^+(k)$ are the amplitudes of the upgoing and downgoing shear field in the layer 1, $g_{l1}(r,z)$ and $g_{s1}(r,z)$ are the potential fields in the solid corresponding to the compressional velocity and the shear velocity respectively.

Using the Sommerfeld radiation condition, the total solution in the layer 2, where the source is located, can be expressed in the form of:

$$g_2(r,z) = \int_0^\infty \{[A_2^-(k)e^{-\alpha_2(z-D)} + A_2^+(k)e^{\alpha_2(z-D)}] + G_{p2}(k,z,z_s)\}J_0(kr)kdk, \qquad (7)$$

$$where \quad \alpha_2 = \begin{cases} -\sqrt{k^2 - k_2^2}, & k > k_2, \\ i\sqrt{k^2 - k_2^2}, & k \le k_2. \end{cases}$$

$A_2^-(k)$ and $A_2^+(k)$ are the amplitudes of the upgoing and downgoing fields in the layer 2, $G_{p2}(k,z,z_s) = \frac{S_\omega e^{\alpha_2|z-z_s|}}{4\pi\alpha_2}$, S_ω is the source strength and D the thickness of the layer 1. Similarly the integral representation of the solution in layer 3 can be introduced as:

$$g_3(r,z) = \int_0^\infty A_3^+(k)e^{\alpha_3[z-(D+L)]}J_0(kr)kdk, \quad \alpha_3 = \begin{cases} -\sqrt{k^2 - k_3^2}, & k > k_3, \\ i\sqrt{k^2 - k_3^2}, & k \le k_3, \end{cases} \qquad (8)$$

where A_3^+ is the amplitude of the downgoing field in layer 3 and L thickness of layer 2. The boundary conditions for such a model are presented in [2], p. 17.

These lead to a linear equation system which can be written as matrix form:

$$C \begin{bmatrix} A_1^- \\ A_1^+ \\ B_1^- \\ B_1^- \\ A_2^- \\ A_2^+ \\ A_3^+ \end{bmatrix} = M, \qquad (9)$$

where matrices C and M are:

$$C = \begin{bmatrix} 2k\alpha_1 & -2k\alpha_1 & -K & -K & 0 & 0 & 0 \\ K & K & -2k\beta_1 & -2k\beta_1 & 0 & 0 & 0 \\ \rho_1 K e^{-\alpha_1 D} & \rho_1 K e^{\alpha_1 D} & -2\rho_1 k\beta_1 e^{-\beta_1 D} & -2\rho_1 k\beta_1 e^{\beta_1 D} & \rho_2 & \rho_2 & 0 \\ 2k\alpha_1 e^{-\alpha_1 D} & -2k\alpha_1 e^{\alpha_1 D} & -K e^{-\beta_1 D} & -K e^{\beta_1 D} & 0 & 0 & 0 \\ -\alpha_1 e^{-\alpha_1 D} & \alpha_1 e^{\alpha_1 D} & k e^{-\beta_1 D} & k e^{\beta_1 D} & \alpha_2 & -\alpha_2 & 0 \\ 0 & 0 & 0 & 0 & \rho_2 e^{\alpha_2 L} & \rho_2 e^{\alpha_2 L} & -\rho_3 \\ 0 & 0 & 0 & 0 & -\alpha_2 e^{-\alpha_2 L} & \alpha_2 e^{\alpha_2 L} & -\alpha_3 \end{bmatrix} \qquad (10)$$

$$where \quad K = 2k^2 - k_s^2, \qquad M = -\frac{S_\omega}{4\pi\alpha_2} \begin{bmatrix} 0 \\ 0 \\ \rho_2 e^{\alpha_2(D-z_s)} \\ 0 \\ \alpha_2 e^{\alpha_2(D-z_s)} \\ 0 \\ \rho_2 e^{\alpha_2[(D+L)-z_s]} \\ \alpha_2 e^{\alpha_2[(D+L)-z_s]} \end{bmatrix} \qquad (11)$$

If the determinant of the coefficient matrix, $Det[C(k)]$, vanishes, then the solutions of the Eq. (9) have poles for the corresponding horizontal wavenumber values. The poles (pole) correspond to additional modes (mode) in the wavenumber spectrum.

3 Numerical examples

To study sound propagation in the Arctic Sea 4 cases are investigated. The measurements are motivated from MIZEX 87 [4] for which an ice-layer is included. It is necessary to emphasize that the roughness and other inhomogeneous properties of ice are neglected in these calculations. For each case some comments are given for observations.

Case 1: 3 layered model, Deep waveguide (vacuum-ice-fluid-fluid waveguide)

The study begins with an ice-covered sea environment for which a half-space fluid is included to neglect the effect of bottom properties. This model can be related to mathematical equations presented at previous section. The following parameters were used to compute Green's function and normal stress shown in Fig. 1 and 2 for two different receiver depths:

Table 1.1 : Environmental parameters for the vacuum-solid-fluid-fluid waveguide.

	$c_l(m/s)$	$c_s(m/s)$	$\rho(gr/cm^3)$	depth (m)
Layer 0 (vacuum)	0	0	0	∞
Layer 1 (ice)	$c_1 = 3000$	1600	0.92	$D = 4$
Layer 2 (water)	$c_2 = 1441$	0	1.0273	$L = 90$
Layer 3 (water)	$c_3 = 1457$	0	1.0279	∞

Where c_l is the compressional sound velocity and c_s is the shear sound velocity and ρ is density.
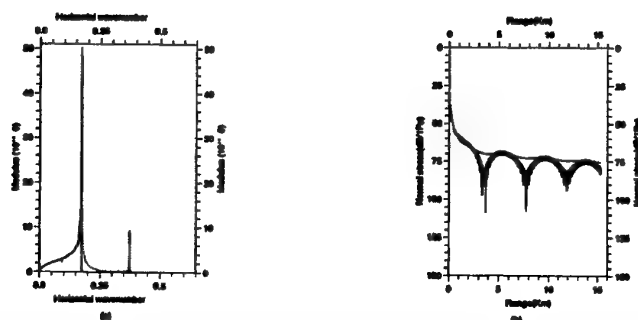
Figure 1: Results for Table 1.1 in layer 2 (RD=18 m) and layer 3 (RD=122 m) (a) modulus of depth-separated Green's function and (b) transmission loss for f=40 Hz, N=4096, contour offset[1] (ϵ)= 0.053 dB/Λ, SD=7 m, RD=18 m (dashed lines) and RD=122 m (solid lines).
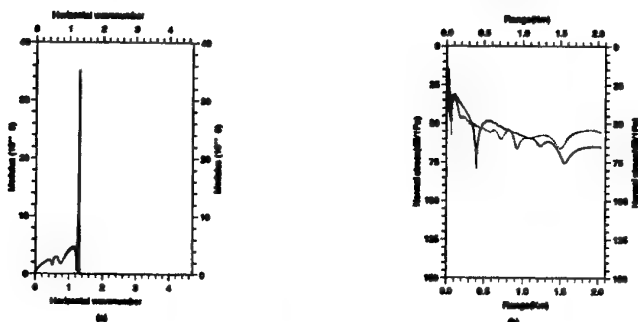

Figure 2: Results for Table 1.1 (a) modulus of depth-separated Green's function and (b) transmission loss for f=300 Hz, N=16384, contour offset (ϵ)= 0.013 dB/Λ, SD=7 m, RD=18 m (dashed lines) and RD=122 m (solid lines).

(1) See [[2], p.35].

Some comments are given for observations:

Green's function, $G_2(k, z)$

- In Fig. 1 (a) ($f = 40Hz$) the sharp peak is a discrete pole associated with the shear sound velocity in the ice.

- In Fig. 1 (a) the last peak ($k \simeq 0.37\ m^{-1}$) is an additional pole which appears in the evanescent spectrum. It is a dramatic shear effect. The pole corresponds to vanishing of the $Det[C(k)]$, C is given by Eq. (10). It belongs to the class of *leaky* waves. The peak disappears when the receiver is moved out deeper in the water (RD=122 m), because in Eq. (7) the first exponential term becomes very small as the receiver depth becomes large.

- In Fig. 2 (a) ($f = 300Hz$) The sharp peak associated with sound propagation in the ice (shear velocity) is a discrete pole. The peak at $k \simeq 0.6\ m^{-1}$ is a part of the continuous spectrum, indicating a leaky mode associated with the compressional sound velocity in the ice.

Normal stress

- In Fig. 1 (b) for $z = 18$m the transmitted field in the layer 1 from layer 2 can be both compressional and shear fields and these can be reflected from the ice-vacuum interface and can be transmitted again as compressional field in the layer 2. The interference pattern has been dominated by the evanescent part.

Case 2: 3 layered model (Vacuum, Arctic sound velocity profile)

Table 1.2: Environmental parameters for the Arctic waveguide 1.

	c_{l1} [top] (m/s)	c_{l2} [bottom] (m/s)	$\rho(gr/cm^3)$	depth (m)
Layer 0 (vacuum)	0	0	0	∞
Layer 1 (water)	1439	1441	1.0273	80
Layer 2 (water)	1441	1456	1.0278	60
Layer 3 (water)	1456	1461	1.0279	360

where c_{l1} is the compressional sound velocity at the top of the layer and c_{l2} compressional sound velocity at the bottom of the layer which is treated by SAFARI as a fluid with $\frac{1}{c_l^2(z)}$ varying linearly with depth. D is the ice thickness and ρ is density.

The modulus of the Green's function and normal stress for the environmental data given in Tables 1.2 have been calculated in the layer 1 and 2 by SAFARI and shown in figures 3 and 4 for the frequencies 40 and 300 Hz respectively.

As one can observe evanescent field is important only for low frequencies at near field (in the number of wavelength), Fig. 3 (a).

Waves with frequencies lower than cutoff frequency $f_{cutoff} = \dfrac{1}{4L\sqrt{\frac{1}{c_1^2} - \frac{1}{c_2^2}}}$ can not propagate along the layer without damping. The cutoff frequency in layer 1 is about $f_{cutoff} \simeq 85\ Hz$
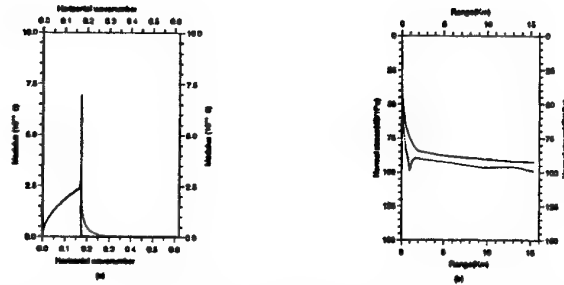
Figure 3: Arctic waveguide 1 (Table 1.2), (a) modulus of depth-separated Green's function. (b) transmission loss for f=40 Hz, N=4096, contour offset(ϵ)=0.053 dB/Λ, SD=3 m, RD=18 m (dashed lines), in the layer 1, and RD=122 m (solid lines), in layer 2.
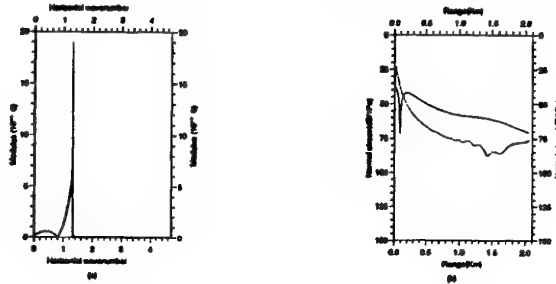
Figure 4: Arctic waveguide 1 (Table 1.2), (a) modulus of depth-separated Green's function. (b) transmission loss for f=300 Hz, N=16384, contour offset (ϵ)=0.053 dB/Λ, SD=3 m, RD=18 m (dashed lines), in the layer 1, and RD=122 m (solid lines), in layer 2.

and in layer 2 about $f_{cutoff} \simeq 16\ Hz$. Sound propagating with frequencies smaller than cutoff frequency can transmit to the next layer and if the source frequency is larger than the cutoff frequency, then the sound energy can be channeled in that layer. In Fig. 3 (b) the sound energy leaks from layer 1 into layer 2 and is channeled and concentrated in the layer 2. Therefore the transmission loss at the receiver depth z =122 m is less than that of in the layer 1 ($z = 18\ m$). This observation is in agreement with the ambient noise recording measurements made in Barents Sea during SIZEX 92 [1].

Case 3: 4 layered model: Vacuum, Arctic sound velocity profile and bottom

The modulus of Green's function and normal stress for the environmental data given in Tables 1.3, presented in case 3 (in which D, ice thickness, is zero), have been calculated and shown in figures 5, 6, 7 and 8 for frequencies 40 and 300 Hz respectively.
In the next part, results are compared with case 4 for which an ice-layer is included.

16

Case 4: 5 layered model (Vacuum, ice, Arctic sound velocity profile and bottom)

Table 1.3: Environmental parameters for the Arctic waveguide 2.

	c_{l1} [top](m/s)	c_{l2}[bottom](m/s)	$c_s(m/s)$	$\rho(gr/cm^3)$	depth (m)
Layer 0 (vacuum)	0	0	0	0	∞
Layer 1 (ice)	3000	3000	1600	0.92	D
Layer 2 (water)	1439	1441	0	1.0273	80
Layer 3 (water)	1441	1456	0	1.0278	60
Layer 4 (water)	1456	1461	0	1.0279	356
Layer 5 (gravel♣)	1800	1800	0	2.0	∞

♣ A compressional attenuation ($\gamma_l = 0.6 \ dB/\Lambda$) is introduced for the absorbing bottom.

The modulus of Green's function and normal stress for the environmental data given in Table 1.3, with an ice thickness $D = 4 \ m$, have been calculated and shown in figures 9, 10, 11 and 12 for frequencies 40 and 300 Hz respectively. Introduction of the ice has reduced the amplitude of the sharp peak. There are no significant changes in the corresponding normal stresses at the low frequencies comparing with the last model in which there was no ice at the top.

As frequency increases to $f = 300 \ Hz$, normal stresses shown in figures 11 (b) and 12 (b), have been damped at short ranges, comparing with figures 7 (b) and 8 (b). The reason is that the field can be transmitted in the ice for the short ranges. The transmitted field is mostly absorbed or trapped in the ice layer.

4 Summary and conclusions

In this paper SAFARI is applied to study acoustic propagation in an ice-covered ocean. There are several attractive features of SAFARI.

- The code is numerically stable for any number of layers.
- The field at a number of receivers can be determined by just one run (not shown here) .
- SAFARI is very useful for the treatment of interface phenomena.

However some numerical limitations have been observed.

- Numerical difficulties appear when the frequency becomes large. To handle this the number of sampling points must be made large,

- Some very short-range effects are neglected in SAFARI, because of applying the asymptotic approximation of the Hankel functions for the wavenumber integrand. This results in oscillations in the normal stress curves at very short ranges.

The study is performed in a progression from simple environments to more complicated models that simulate ocean Arctic environments. Each model introduces greater complexity so that the importance of the different parameters can be isolated. The analytic integral expressions for the field for a simple 3 layered model are obtained by using boundary conditions. In these calculations only compressional monochromatic point sources have been used. In each experiment both the source and receivers are localized in the water below the ice interface.

The computations by SAFARI are performed for source frequencies at 40 and 300 Hz. The main observations and results from the numerical study are:

- As the separation between the receiver and the interface increases, either by increasing of the frequency or for a fixed frequency by moving the receiver down away from the interface, the exponential decay makes the evanescent portion diminished.

- Sound will be transmitted into an ice layer as compressional and shear waves. There is a competition between compressional and shear waves at the ice-water boundary.

- For the incident angles less than the critical angle (corresponding to the compressional waves), there are only compressional waves in the ice layer. As the range increases the shear waves transmission coefficient increases while the transmission coefficient for the compressional waves decreases.

- At a particular range the transmission coefficients for the compressional waves and shear waves become equal and interfere destructively. This phenomena can be observed as the regularly spaced frequency resonances in reflection loss patterns and as a local minimum in transmission loss patterns.

- The subsequent shear waves are trapped in the ice and even a small shear attenuation eventually removes all the energy in the shear field. The trapped compressional waves in the ice layer are only important at short ranges.

- The elastic properties of the ice have a significant effect on the reflection, although these properties do not affect the frequency separation of the peaks in the reflection loss pattern. The strengths of the mode conversions at the water-ice boundary depend on the ice compressional and shear sound speed.

References

[1] I. Engelsen. SIZEX 92, AMBIENT NOISE MEASURMENTS DATA REPORT. Technical report, FFI / report- 93, 2006, 1993.

[2] H.Schmidt. SAFARI, report of the Seismo-acoustic Fast field Algorithm for Range-Independent environment. Technical report, SACLANT Undersea Research Centre, 1988.

[3] F.B. Jensen. *Numerical models in underwater acoustics*. edited by L. B. Felsen (Nijhoff Dordrecht), 1984.

[4] C. Geiger S. Sandven, Z. Kovacs and O. M. Johannesson. MIZEX 87, CTD DATA REPORT FROM POLAR CIRCLE. Technical report, NERSC, Report No. 13, 1988.

Figure 5: Results for Arctic waveguide 2 (Table 1.3), for $D=0$, (a) modulus of depth-separated Green's function in layer 2, $\mid G_2(k,z) \mid$, and (b) Transmission loss for f=40 Hz, N=4096, contour offset(ϵ)=0.053 dB/Λ, SD=3 m, and RD=18 m.

Figure 6: Results for Arctic waveguide 2 (Table 1.3), for $D=0$, (a) modulus of depth-separated Green's function in layer 3, $\mid G_3(k,z) \mid$, (b) transmission loss in layer 3 for f=40 Hz, N=4096, contour offset (ϵ)=0.053 dB/Λ, SD=3 m, RD=122 m .
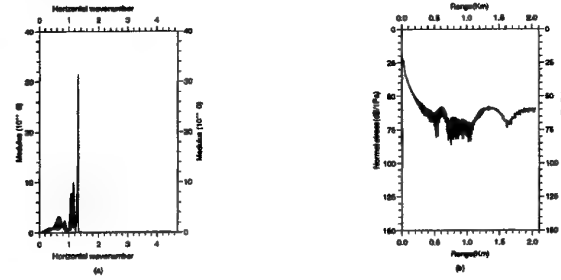
Figure 7: Results for Arctic waveguide 2 (Table 1.3), for $D=0$, (a) modulus of depth-separated Green's function in layer 2, $\mid G_2(k,z) \mid$, (b) transmission loss in layer 2 for f=300 Hz, N=16384, contour offset (ϵ)=0.013 dB/Λ, SD=3 m, RD=18 m.
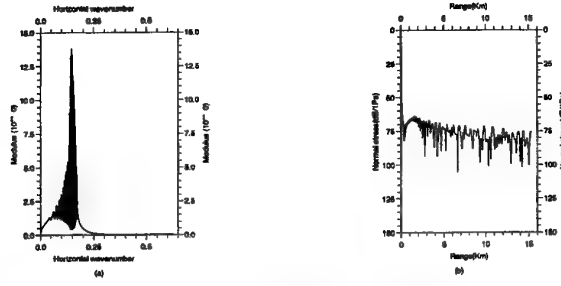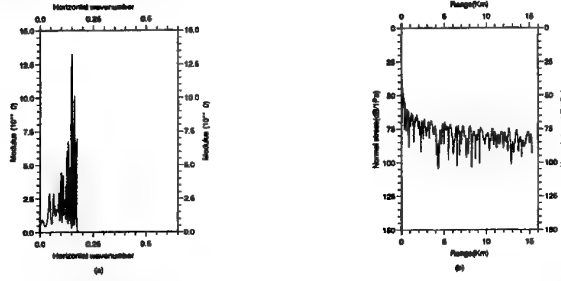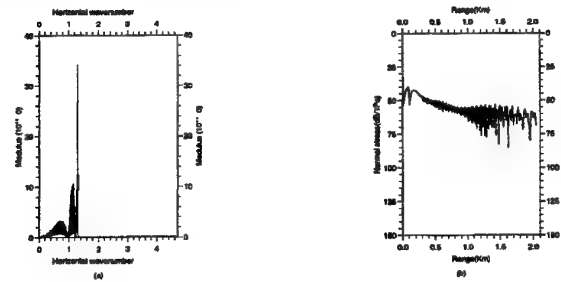

Figure 8: Results for Arctic waveguide 2 (Table 1.3), for $D=0$, (a) modulus of depth-separated Green's function in layer 3, $\mid G_3(k,z) \mid$, (b) Transmission loss in layer 3 for f=300 Hz, N=16384, contour offset (ϵ)=0.013 dB/Λ, SD=3 m and RD=122 m.

Figure 9: Results for Arctic waveguide 2 (Table 1.3), for $D=4\ m$ (ice thickness), (a) modulus of depth-separa ted Green's function , $\mid G_2(k,z)\mid$, (b) transmission loss for f=40 Hz, N=4096, contour offset(ϵ)=0.053 dB/Λ, SD=7 m, and RD=18 m.

Figure 10: Results for Arctic waveguide 2 (Table 1.3), for $D=4\ m$ (ice thickness), (a) modulus of depth-separated Green's function in layer 3, $\mid G_3(k,z)\mid$, (b) transmission loss in layer 3 for f=40 Hz, N=4096, contour offset (ϵ)=0.053 dB/Λ, SD=7 m, RD=122 m.
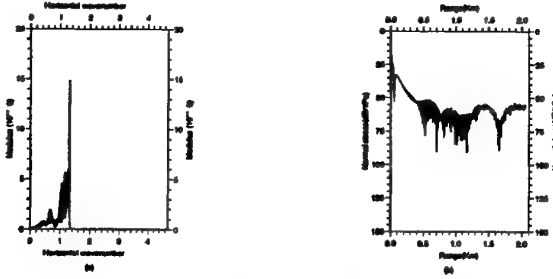
Figure 11: Results for Arctic waveguide 2 (Table 1.3), for $D=4\ m$ (ice thickness), (a) modulus of depth-separated Green's function in layer 2, $\mid G_2(k,z)\mid$, (b) transmission loss in layer 2 for f=300 Hz, N=16384, contour offset (ϵ)=0.013 dB/Λ, SD=7 m, RD=18 m.
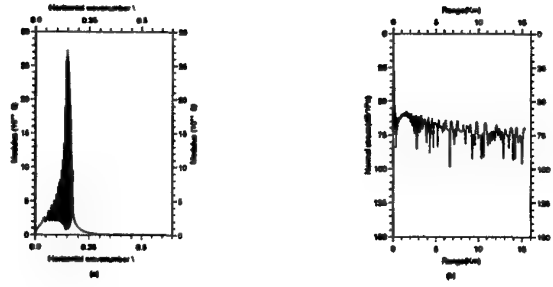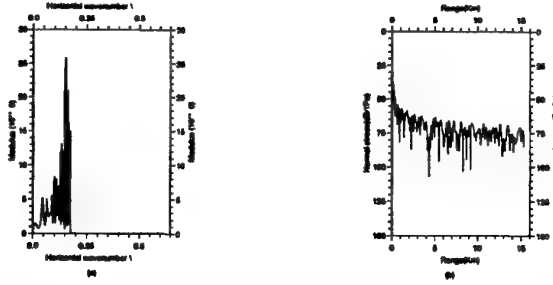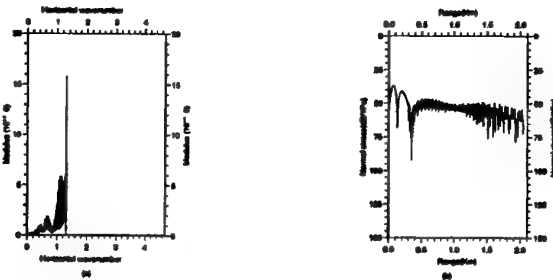

Figure 12: Results for Arctic waveguide 2 (Table 1.3), for $D=4\ m$ (ice thickness), (a) modulus of depth-separated Green's function in layer 3, $\mid G_3(k,z)\mid$, (b) transmission loss in layer 3 for f=300 Hz, N=16384, contour offset (ϵ)=0.013 dB/Λ, SD=7 m and RD=122 m.

Investigation of the compressional reflection loss in the ice-covered Arctic Sea

Amir Hashemi

Department of Engineering, Bergen University College, Bergen, Norway

Abstract

This numerical study describes reflection of plane acoustic waves from an ice-layer overlying a water halfspace. Compressional reflection coefficient and reflection loss for a simple two layered model are investigated. Results illustrated the dependence of reflection coefficient on ice thickness and source frequency.

1   Introduction

The discontinuity in the interface between two materials produces a significant influence on the wave propagating through the medium. The reflection coefficient is a mathematical formulation of the physical effect of the boundary on the incident wave field and can be mentioned as a filter on the wavenumber. A large amount of literature deals with acoustic reflection from the bottom or sea floor. The sound reflection from the ice-covered sea environment can be treated similarly. Ice can be considered as an elastic medium, which means an incident compressional plane wave can be reflected/transmitted as both compressional and shear waves. The reflection coefficient, the ratio of the amplitude of the reflected plane wave to the amplitude of a plane wave incident on the ice overlying the sea, is an important factor for investigation of the effect of the ice-cover on acoustic propagation. The roughness properties of ice are neglected in this study.

This paper focuses on the ratio of the amplitude of the direct reflected compressional plane wave to the amplitude of an incident compressional plane wave, as shown in Fig. 1:
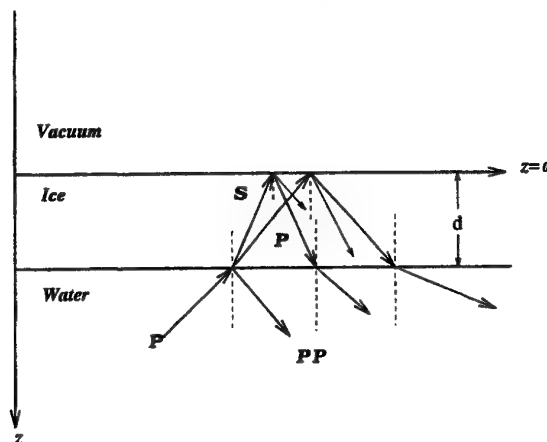
Figure 1: Reflection of an incident compressional (P) plane wave from interfaces of a vacuum-ice-water environment, PP: direct reflected P wave.

Hydrological measurements in the Marginal Ice Zone (MIZ) of the Greenland Sea reveals that the sound speed profile for the ice-covered Arctic Sea can be considered range-independent. SAFARI, which provides accurate transmission loss values for propagation in range-independent multi-layered horizontally stratified environment, can be a useful tool to study the reflection coefficient for the ice-covered region of the Arctic Sea.

In order to provide a basis for an initial investigation, the reflection coefficient formula for direct reflected P wave for a simple 2 layered environment (vacuum-solid-fluid halfspace) is presented in Sec. 2 . A parameter study of effects of compressional and shear properties of ice on the reflection loss is given by a numerical example in Sec. 3. Dependency of reflection coefficient on incident angle, frequency and ice thickness is studied in Sec. 3.2. Finally the results are summerized in Sec. 4. The simulations were performed by SAFARI [1].

2   Mathematical formulation

The compressional reflection coefficient, R_{pp}, for the 3 layered environment shown in Fig. 1 (vacumm-solid-fluid) can be expressed as:

$$R_{pp} = e^{-i\phi}, \quad \phi = 2arctan[\frac{(MZ_1)Z_3}{(MZ_1)^2 - (NZ_1)^2}], \tag{1}$$

where

$$M = \frac{1}{Z_1}[Z_2cos(2\theta_s)^2cotg(p) + Z_ssin(2\theta_s)^2cotg(q)],$$

$$N = \frac{Z_2cos(2\theta_s)^2}{Z_1sin(p)} + \frac{Z_ssin(2\theta_s)^2}{Z_1sin(q)}, \tag{2}$$

$$p = k_2dcos(\theta_2), \quad q = k_sdcos(\theta_s), \tag{3}$$

$$Z_1 = \frac{\rho_1c_1}{cos(\theta_1)}, \quad Z_2 = \frac{\rho_2c_2}{cos(\theta_2)}, \quad Z_s = \frac{\rho_2c_s}{cos(\theta_s)}, \quad Z_3 = \frac{\rho_1c_{l3}}{cos(\theta_3)}, \tag{4}$$

where ρ_1, ρ_2 and ρ_3 are densities of the layers 1,2 and 3 ($\rho_1 = 0$ for the vacuum), Z_1 and Z_3 impedances for the layer 1 ($Z_1 = 0$ for vacuum) and 3, Z_2 and Z_s are compressional and shear impedances for layer 2, θ_1 is the incident angle, θ_3 is the transmitted angle in the layer 3, θ_2 and θ_s are the transmitted angles in the layer 2 corresponding to the compressional and shear fields, k_2 and k_s are the wavenumbers in layer 2 (ice) corresponding to the compressional and shear fields [2] . The reflection coefficient is an oscillatory function of p and q.

The complex reflection coefficient R_{pp} can be expressed by modulus $\mid R_{pp} \mid$ and phase $tan^{-1}\frac{Im[R_{pp}]}{Re[R_{pp}]}$. In underwater acoustics, the modulus is usually represented by the corresponding reflection loss:

$$R_{loss} = -20log \mid R_{pp} \mid \tag{5}$$

In the next section a numerical study will be performed on the compressional reflection coefficient, R_{pp}, and reflection loss for a simple vacuum-ice-water environment in which a monochromatic point source localized just below the ice interface in the water.

22

3   Numerical example: ice-covered deep waveguide

A simple 2 layered environment was used to study an ice-covered region of Arctic Sea. Even if the chosen simulated environment is very simple, remarkable results are observed.

Table 1.1: Environmental data for vacuum-ice-water model.

	c_l (m/s)	c_s (m/s)	γ_l (dB/Λ)	γ_s (dB/Λ)	$\rho(gr/cm^3)$	depth (m)
Vacuum	0	0	0	0	0	∞
Ice	3000	1600	1.	2.5	0.92	d= 1, 2, 4
Water	1500	0	0	0	1.0	∞

Where c_l is the compressional sound velocity and c_s is the shear sound velocity, ρ is density and γ_l and γ_s are compressional and shear attenuation coefficients for ice respectively.

Fig. 2 presents the modulus of the reflection coefficient versus incident angle which confirms the dependency of reflection coefficient on frequency, f, and ice thickness, d.
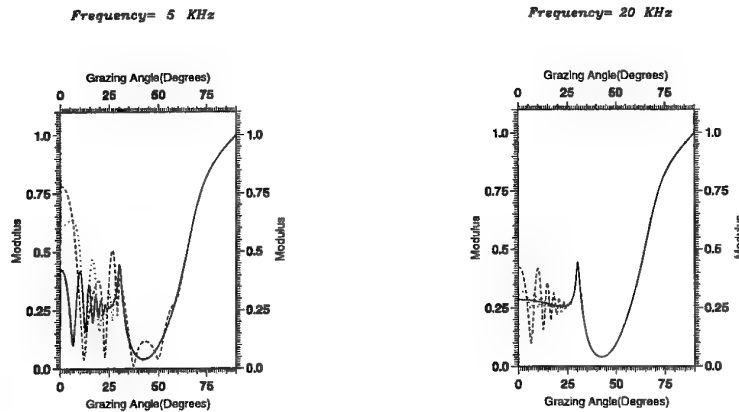
Figure 2: Modulus of the compressional reflection coefficient for Table 1.1 for ice thickness 4 m (solid curve), 2 m (dashed) and 1 m (dotted).

3.1   Interesting cases for vacuum-ice-water model

In this part reflection loss, given by Eq. (5), is studied for some important angles or different sound velocities. Reflection loss for the following angles is calculated and is shown in Fig. 3:

1) $\theta = 0°$, normal incident.

2) $\theta = 30°$ (the critical angle due to the compressional sound velocity in the ice).

3) θ=41.5° , for which the pure shear wave transmission occurs.

4) θ =69.5° (the critical angle due to the shear sound velocity in the ice).
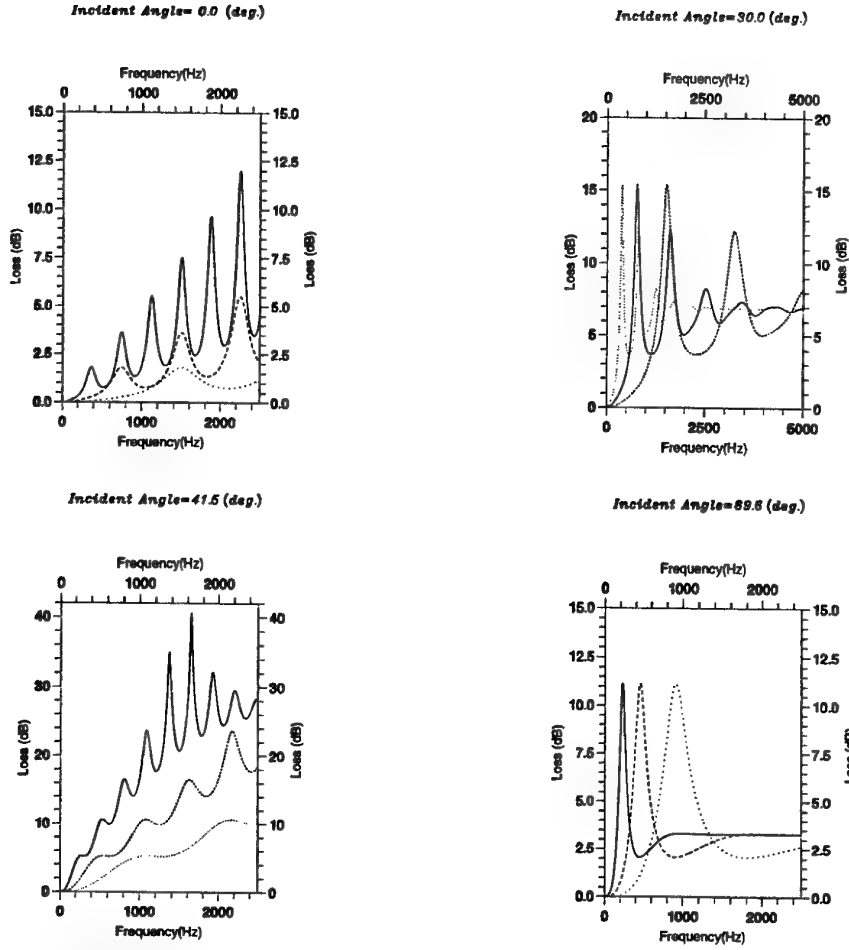
Figure 3: Reflection loss ($R_{loss} = -20log \mid R_{pp} \mid$) for vacuum-ice-water model, ice thickness d=4 m (solid curve), 2 m (dashed) and 1 m (dotted).

The frequency of the peaks corresponds to $\frac{c_a}{2dcos(\theta_a)}$, so when the ice thickness increases the spacing of the peaks decreases. These peaks appear when the reflection coefficient becomes very small, and the transmitted waves are trapped in the ice layer.

To illustrate how the variation of different parameters that describe the physical properties of environment can affect the reflection loss, the following cases are considered

a) Variation of the compressional velocity in the ice is studied in Fig. 4 (a) (c_2= 3500, 3200 and 3000 (m/s)).
b) Variation of the shear sound velocity in the ice is studied in Fig. 4 (b) (c_s=1800, 1700 and 1600 (m/s)).

The reflection loss is sensitive to the compressional sound velocity in the ice for $\theta < \theta_{cr1} = 30°$, where compressional waves dominate. For $\theta > \theta_{cr1}$, where the shear waves dominate, reflection loss increases by increasing of the shear sound velocity in the ice.
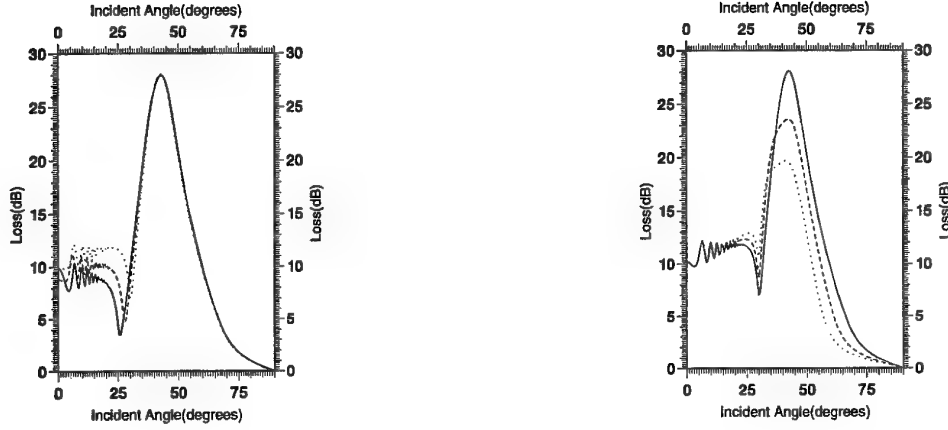
(a) c_s=1600 m/s, variation of c_2: 3500 (solid lines), 3200 (dashed lines) and 3000 m/s (dotted).

(b) c_2=3000 m/s, variation of c_s:1800 (solid lines), 1700 (dashed lines) and 1600 m/s (dotted).

Figure 4: Reflection loss ($R_{dB} = -20log \mid R_{pp} \mid$) for Table 1.1 (vacuum-ice-water), Frequency=10 KHz and ice thickness=4 m.

3.2   Numerical results

For a vacuum-ice-water environment, as shown in Fig. 1, the reflection coefficient is a function of the incident angle, source frequency and the ice thickness (R=$R(\theta, f, d)$). Contour plots can be used to demonstrate the effect of frequency for different incident angles for a fixed ice thickness on reflection coefficient. Contouring is performed for the samplings $\Delta\theta = 0.5°$ and $\Delta f = \frac{f}{200}$. Fig. 5. demonstrates contour plots for the modulus of the reflection coefficient for the parameters given in Table 1.1.

The contour plots can be discussed by the multiplication of the source frequency and ice thickness term (df) or by a relation between d and λ_2, where λ_2 is the wavelength of the compressional waves in the ice (m).

- For $df < 200$ ($d < \frac{\lambda_2}{15}$), total reflection occurs for all incident angles.

- For $200 < df < 500$ ($d < \frac{\lambda_2}{6}$), there is a phase shift at the critical angle ($\theta_{cr1} = 30°$). No shear waves have been exited in ice yet.

- For $< df < 800$ ($d < \frac{\lambda_2}{3.75}$), transmitted shear waves can be observed for $\theta > \theta_{cr1} = 30°$.

- For $df > 800$ ($d > \frac{\lambda_2}{3.75}$):

There are oscillations for $\theta < \theta_{cr1} = 30°$, where the compressional waves dominate and oscillations reduces as df becomes larger.

The reflection coefficient becomes smaller and smaller for $41° < \theta < 55°$, where shear waves dominate and corresponds to the high reflection loss region. In this interval interface waves of the *Scholte* or *Stonely* [2] type are excited.

- For $df > 4000$ ($d < \frac{4\lambda_2}{3}$) and $\theta > \theta_{cr2} \simeq 70°$, reflection coefficient does not vary any more.

- For $df > 12000$ ($d > 4\lambda_2$), the refection coefficient in the interval $41° < \theta < 55°$ has become very small and stabilized.

- The reflection coefficient becomes very small when the frequency, the ice thickness and the incident angle confirm to the relation $f = \frac{c_s c_1}{2d\sqrt{c_1^2 - c_s^2 \sin(\theta)}}$.

4 Summary

Compressional waves are divided to the shear waves and compressional waves at the boundary of the water-ice interface. These shear waves can be reflected from the ice-vacuum boundary and converted back to the compressional waves into water through the ice-water boundary. This conversion can be observed especially when the frequencies and the angles and the ice thickness coincide with shear wave resonances in the ice layer ($f = \frac{c_s}{2d\cos(\theta_s)}$), which causes the noticeable peaks in the reflection loss (see Fig. 3). The *mode conversion* coefficients are sensitive to the compressional and the shear speed in the ice.

A study is performed for different incident angles and frequencies and ice layer of thickness 1, 2 and 4 m, $d = \frac{\lambda}{2}, \lambda, 2\lambda$, which can be an interesting area for some further experiments.

At low frequencies and low angles, the transmitted compressional wave is evanescent, only the direct reflection is present and the field decays exponentially in the ice separating from the boundary. If the ice is very thin, these compressional waves can be excited as surface waves.

The shear properties of the ice dominate when the angle of incidence exceeds the critical angle related to the compressional sound velocity in ice (approximately $\theta = 30°$) and the reflection loss is very high for the interval $30° < \theta < 69.5°$. In this case sound can penetrate into the ice.

The reflection coefficient for the incidence angles larger than the critical angle regarding to the shear sound velocity in ice (approximately $\theta = 70°$) is very complicated since both transmitted angles are complex.

In the vacuum-ice-water environment, ice thickness is not important for high frequencies and large incident angles.

References

[1] H.Schmidt. SAFARI, report of the Seismo-acoustic Fast field Algorithm for Range-Independent environment. Technical report, SACLANT Undersea Research Centre, 1988.

[2] L.M.Brekhovskikh. *Waves in Layered Media.* Number Second Edition. 1989.
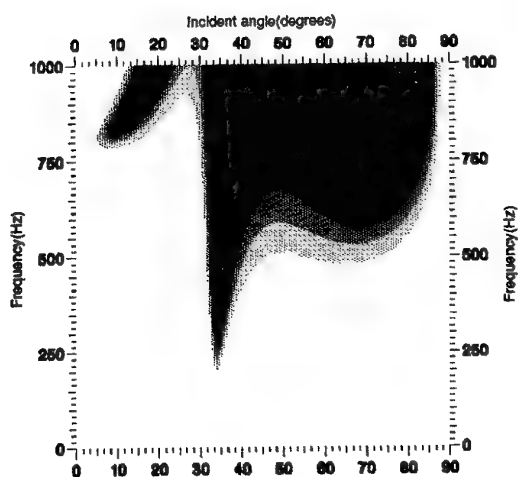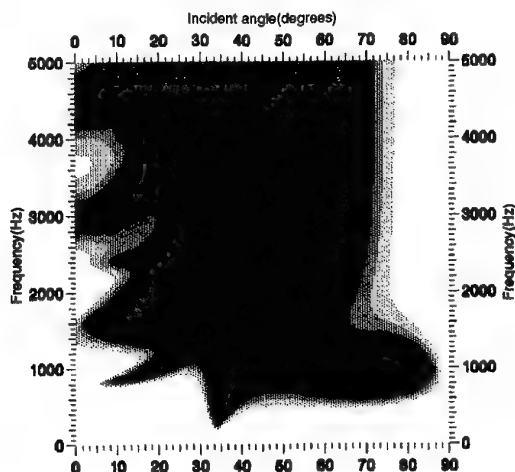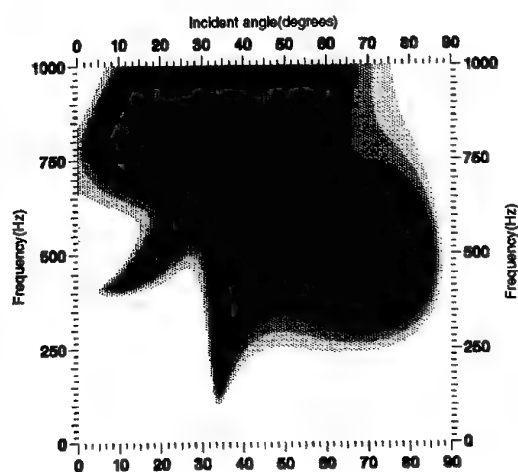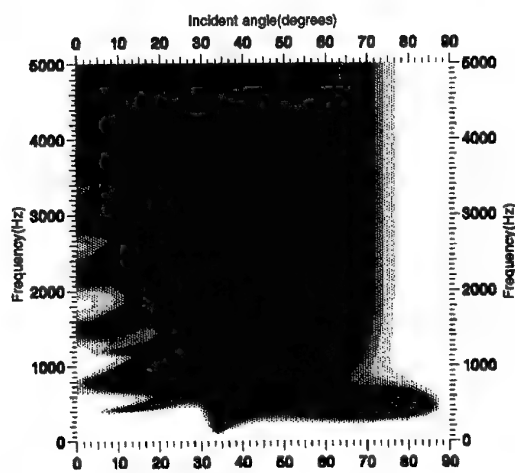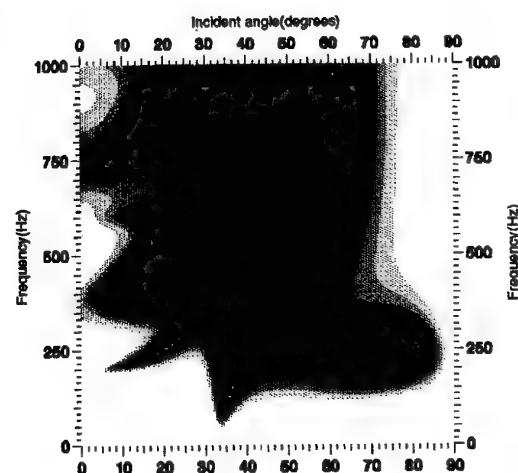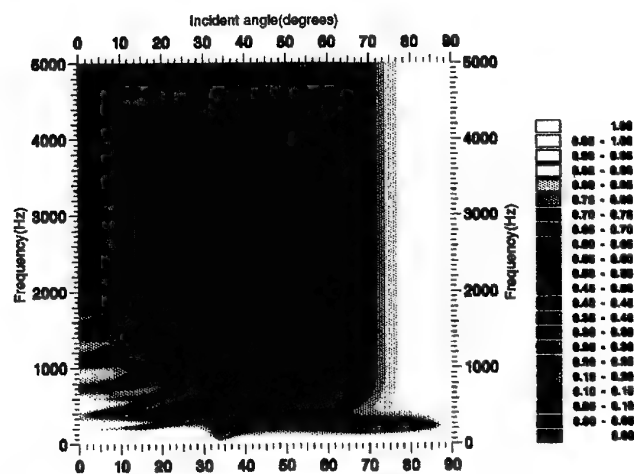
Figure 5. : Contour plot of modulus of reflection coefficient as function of incident angle and frequency for Table 5.2, ice Thickness (d) =1 m, 2m and 4m .

Numerical calculations of sound propagation over ground surfaces
Viggo Henriksen
SINTEF Telecom and Informatics

SUMMARY
The purpose of this study has been to develop a numerical model for sound propagation in both air and ground over long distances. Wave propagation in both air and ground is modeled by a set of partial differential equations for wave propagation in a porous medium with a rigid frame. By introducing Chebyshev spectral collocation in the spatial variable the equations are transformed to a set of ordinary differential equations in time. Domain decomposition is used to divide the computational domain into subdomains of manageable sizes. All subdomains are homogenous in the sense that they contain only ground or air. Some numerical examples are calculated in two dimensions and the results are compared to analytical results and to some results from outdoor measurements. These comparisons show the low dispersion and dissipation of spectral collocation, and that the suggested model gives good results for sound propagation over long distances.

THE DIFFERENTIAL EQUATIONS
Sound propagation in a porous medium with a rigid frame is modeled by the linear Eqs. (1.1) and (1.2).

$$\nabla p + \rho' \frac{\partial v}{\partial t} + Rv = 0 \tag{1.1}$$

$$\frac{\partial p}{\partial t} + \rho' c'^2 \nabla \cdot v = 0 \tag{1.2}$$

Here p is the air pressure, v a vector containing the particle velocity components and R the flow resistivity. Furthermore is ρ' the equivalent density and c' the equivalent sound speed for the porous medium and they are given by Eq. (1.3) and (1.4) respectively.

$$\rho' = \frac{\rho_0 k_s}{\varphi} \tag{1.3}$$

$$c' = \frac{c}{\sqrt{k_s}} \tag{1.4}$$

Here is ρ_0 the air density, k_s the structure factor, φ the porosity and c the sound speed in the air.

SPECTRAL COLLOCATION
If a two-dimensional Cartesian coordinate system is chosen, Eq. (1.1) and (1.2) can be written as Eq. (1.5).

$$\frac{\partial U}{\partial t} + A_1 \frac{\partial U}{\partial x} + A_2 \frac{\partial U}{\partial y} + CU = 0 \tag{1.5}$$

The vector U is defined by $U = [u\, v\, p]$ with u and v being the horizontal and vertical particle velocity components and p the air pressure. Introducing Chebyshev spectral collocation in the spatial variable leads to a discretization in space and thereby a transformation of our PDEs to ODEs in time.

$$\frac{\partial}{\partial t} u + \frac{1}{\rho'} D_x p + \frac{R}{\rho'} u = 0 \tag{1.6}$$

$$\frac{\partial}{\partial t} v + \frac{1}{\rho'} D_y p + \frac{R}{\rho'} v = 0 \tag{1.7}$$

$$\frac{\partial}{\partial t} p + \rho' c'^2 \left(D_x u + D_y v \right) = 0 \tag{1.8}$$

The matrixes **u**, **v** and **p** contain the velocity components and pressure values at the discretization points, which are called collocation points in the spectral collocation method. Matrixes $\mathbf{D}_x$ and $\mathbf{D}_y$ are the derivative matrixes in the two spatial directions (see Canuto, Hussaini, Quarteroni and Zang 1988 for more details about the derivative matrixes). A second order explicit Runge-Kutta method was used in the time integration of the ODEs.

DOMAIN DECOMPOSITION
Domain decomposition was introduced to be able to calculate sound propagation for large computational domains. The computational domains were divided into a set of smaller non-overlapping subdomains. Computational domains that contained both air and ground were divided into subdomains containing only air or ground, so in a sense the subdomains were homogenous. Satisfaction of the differential equations had to be ensured on the boundaries between subdomains too. Therefore a correctional method, where the boundary values were corrected between each timestep in the Runge-Kutta time integration, was introduced. The corrected values were calculated on the basis of the physical boundary conditions, continuous normal particle velocity and air pressure , and implemented via characteristic boundary conditions (Bjørhus 1995 and 2000).

OPEN BOUNDARIES
Reflections of the propagating signal from the outer boundaries of the computational domain have a tendency to contaminate the solution. Such reflections should therefore be kept as small as possible. An approximation to the exact open boundary conditions was therefore implemented via characteristic boundary conditions at the outer boundaries. The chosen approximation was quite good for normal incidence, but unfortunately it didn't perform nearly as good when the angle of incidence increased.

MAPPING OF DOMAINS
Because spectral collocation requires square domains, some special attention had to be made when domains of more complex shapes were used. This problem was solved by performing a mapping of complexly shaped domains onto a square. The mapping lead to a transform of the spatial variables.

NUMERICAL EXPERIMENTS
Some numerical experiments were calculated to test the proposed model. The calculations were done in two dimensions. A computational domain with 66 subdomains (3x22) and the dimensions 15x110 meters (height x length) was used. There were 51 collocation points in each direction in each subdomain. This gave a resolution of 3.44 points per wavelength for a 1000 Hz signal. A point source was implemented by trigging one collocation point with an air pressure that varied with time. This point source was set to radiate a bandlimited signal between approximately 100 and 900 Hz. The power spectral density of the source signal is shown in Fig. 1.

The sound speed and damping of the signal in free field was calculated from a simulation with only air domains. The sound speed between 5 and 80 meters from the source is shown in Fig. 1. The damping of the signal over the same distance is shown in Fig. 2.
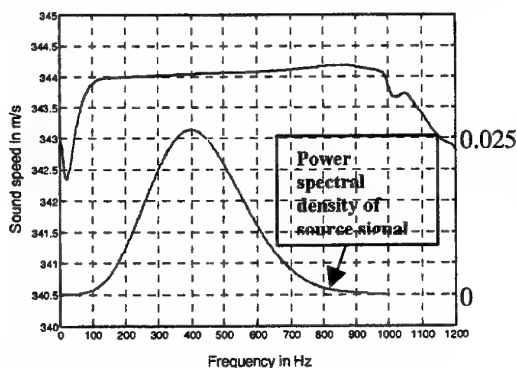
Fig. 1. Sound speed between 5 and 80 meters from the source.   Fig. 2. Damping between 5 and 80 meters from the source.
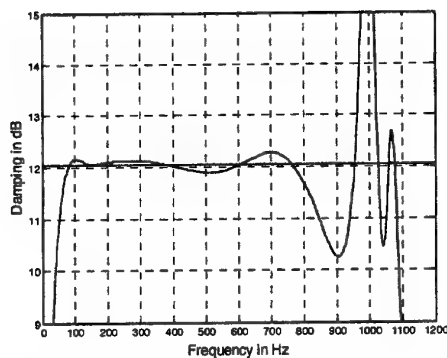
In these experiments a sound speed of 344 m/s was chosen for the air. Fig. 1 shows that the sound speed in the calculations is highly accurate within the frequency band of the source signal. In other words there is hardly any dispersion at distances up to at least 80 meters. For two dimensions a damping of 12 dB is expected between 5 and 80 meters from the source.

29

Fig. 2 shows that the damping in the numerical experiments is in good accordance with the expected damping. There is however a dip centered at 900 Hz. This dip is most likely caused by interference between the direct wave and a reflection from the boundaries of the computational domain. This shows the importance of good open boundary conditions at the outer boundaries of the computational domain.

An approximation to the ground profile shown in Fig. 3 was implemented based on measurements done at Granåsen in Trondheim (Storeheier 1999).
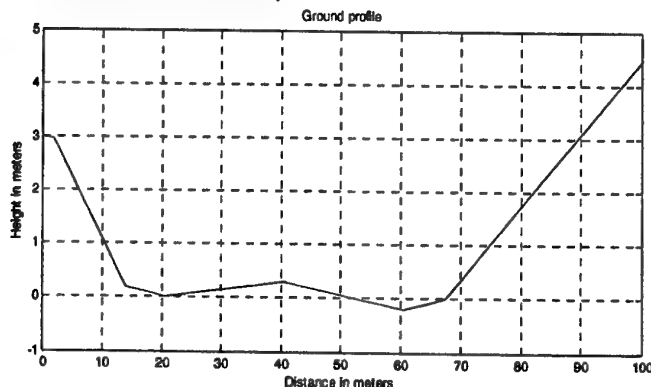
Fig. 3. Measured ground profile.

The parameters in the ground were chosen based on measurements done at this site. At zero meters a point source was placed 1.5 meters above the ground (0,4.5). The source signal was the same as for the experiment described above. The resulting air pressure was registered at a point 2 meters above the ground and 100 meters from the source (100,6.5). The air pressure relative to the expected free field value for two dimensions (insertion loss) was calculated and compared to measurements done at the site.
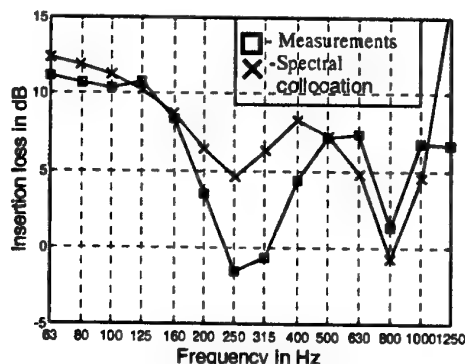
Fig. 4. Air pressure relative to free field at 100 meters from the source.

The results from the calculations with spectral collocation follow the measurements quite nicely except for the fact that the destructive interference at 250 Hz isn't large enough.

CONCLUSION
Spectral collocation is well known for its low dispersion and dissipation. The results above have confirmed this and shown that spectral collocation is a useful method for calculating sound propagation over long distances. The only major advantage is the fact that the calculations are very time consuming. It took 40 hours to calculate the results shown in Fig. 4. The calculations were done on a PC with a 733 MHz Pentium III processor and 512 Mb of internal memory. There are however ways to reduce the computational time and this should be investigated further.

REFERENCES

Bjørhus, M., A computational model for outdoor sound propagation. Part II: A spectral collocation method, SINTEF Report STF42 A00XYZ, SINTEF Applied Mathematics, Norway, 2000.

Bjørhus, M., The ODE formulation of hyperbolic PDEs discretized by the spectral collocation method, SIAM J. Sci. Comput., No. 16, Mai 1995.

Canuto, C., Hussaini, M. Y., Quarteroni, A. and Zang, T. A., *Spectral methods in fluid dynamics*. Springer-Verlag, New York, 1988.

Storeheier, S. Å., Validation of propagation model for non-flat terrain. Results of outdoor measurements. SINTEF Report STF40 A99074, SINTEF Telecom and Informatics, Norway, 1999.

Split-beam transducer with 3 sections

helge.bodholt@simrad.no

Introduction

The traditional split-beam echo sounder measures the phase angle between the signals received on two transducer halves. With four transducer sections, arranged as four quadrants, the direction to the target can be measured both longitudinal and transverse. This has been the principle in all Simrad split-beam transducers for target strength measurements; from the first ES380 in 1983 to the latest 200 kHz composite transducer ES200-7 introduced last year.

However, three sections would be enough to provide the necessary information; and a new split-beam transducer ES30-10 with three sections is now introduced. The frequency is 38 kHz, and the beamwidth is 10 degrees. The three sections are identical, with 120 degrees rotation from one to another.

ES38-10
with three sections

bird's-eye view

split-beam transducer
with four sections
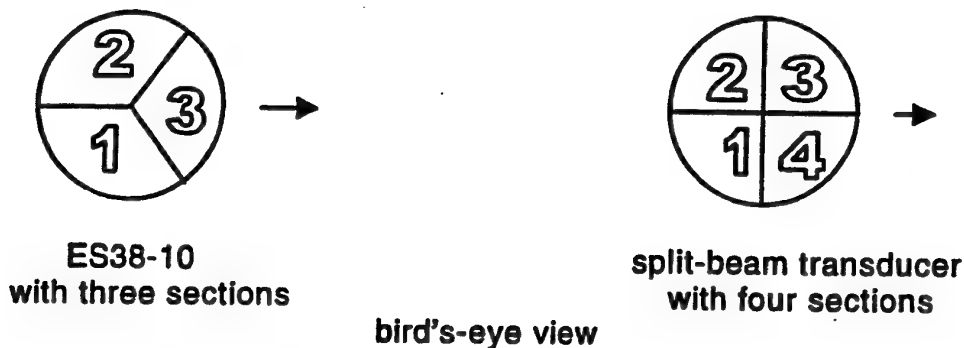
Angle measurement

For a traditional split-beam transducer configured with two halves, the angle u, between the acoustic axis and the direction to the target is derived from

$$\varphi = kd \sin u \qquad (1)$$

where φ=phase angle between the signals received
        on the two transducer halves
k=wave number=$2\pi/\lambda$
λ=wavelength
d=distance between the centres of the two transducer halves

Normally the angle u is small, so that $\sin u$ can be approximated by u, and we have

$$\varphi = k\, d\, u$$

The product $\Lambda = kd$ is called the angle sensitivity, and the relation between the phase angle and the physical angle to the target can be written as

$$\varphi = \Lambda\, u \qquad\qquad (2)$$

In Simrad split-beam echo sounders the phase angle φ is detected in the receiver and transferred to the main processor, where the angle u is calculated as $u = \varphi / \Lambda$
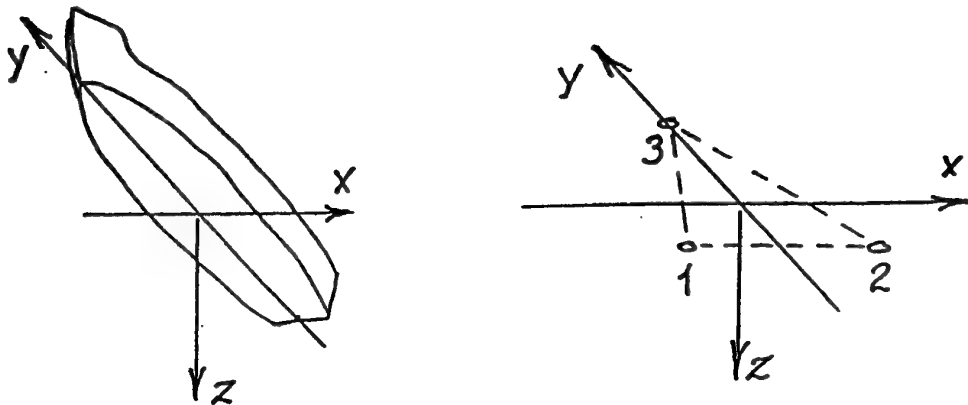
For a transducer with three sections the mathematics is a little more complicated. The acoustic centres of the three sections have the co-ordinates:

$$\mathbf{e}_1 = (-\frac{\sqrt{3}}{2}a \quad -\frac{1}{2}a \quad 0)$$

$$\mathbf{e}_2 = (\frac{\sqrt{3}}{2}a \quad -\frac{1}{2}a \quad 0) \qquad\qquad (3)$$

$$\mathbf{e}_3 = (0 \quad a \quad 0)$$

in a right handed xyz-system with the y-axis pointing ahead on the vessel and the z-axis pointing vertical down. a is the distance from origo to one of the acoustic centres. For the new 38 kHz transducer a is 66 mm.

s is a unit vector in the direction towards the target

$$s = (\cos v_x \quad \cos v_y \quad \cos v_z)$$

where v_x v_y and v_z are the angles from s to the axes of the co-ordinate system.

The echo signals received on the three transducer sections have different phase angles caused by the different travel distances to the three acoustic centres. With origo as the reference point, the extra travel distance to a point e is the inner product $e \cdot s$. The phase angles at the acoustic centres, relative to origo, are
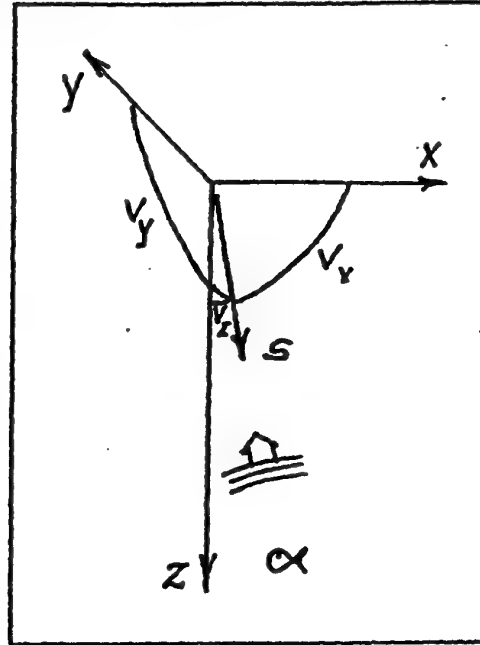
$$\varphi_{10} = k \, e_1 \cdot s$$
$$\varphi_{20} = k \, e_2 \cdot s \qquad \qquad (4)$$
$$\varphi_{30} = k \, e_3 \cdot s$$

The three phase angles are not independent. The relation between them is

$$\varphi_{10} + \varphi_{20} + \varphi_{30} = k(e_1 + e_2 + e_3) \cdot s = 0 \qquad (5)$$

The angles v_x and v_y can be derived from the equations (4) and (3)

$$\varphi_{10} = k \, e_1 \cdot s = k\left(-\frac{\sqrt{3}}{2} a \cos v_x - \frac{1}{2} a \cos v_y\right)$$

$$\varphi_{20} = k \, e_2 \cdot s = k\left(\frac{\sqrt{3}}{2} a \cos v_x - \frac{1}{2} a \cos v_y\right) \qquad (6)$$

$$\varphi_{30} = k \, e_3 \cdot s = k a \cos v_y$$

which lead to $\quad \cos v_x = \dfrac{1}{\sqrt{3} ka} (\varphi_{20} - \varphi_{10}) \qquad (7)$

$$\cos v_y = \frac{1}{3ka} (2\varphi_{30} - \varphi_{10} - \varphi_{20})$$

The echo sounder screen presents a horizontal cross-section of the beam, with fish echoes marked as dots at their respective positions in the beam. The unit vector s is pointing in the direction to the target, and the projection of s onto the xy-plane is used for the screen presentation. The projection of s has the co-ordinates $(\cos v_x \quad \cos v_y)$. These cosines have to be calculated for every depth sample.

The signals from the three transducer sections goes to three receiver channels and comes out as three digital complex numbers, G_1, G_2 and G_3. In the equations (7) there are three phase angles. They can be found by an arctan(Im/Re). However, the arctan is a time consuming function, and it may be worthwhile to reduce the number of phase angles from three to two with the following manipulation. We define

$$\varphi_{31} = \varphi_{30} - \varphi_{10}$$
$$\varphi_{32} = \varphi_{30} - \varphi_{20}$$
(8)

and the equations (7) can be written as

$$\cos v_x = \frac{1}{\sqrt{3}ka}(\varphi_{31} - \varphi_{32})$$
(9)

$$\cos v_y = \frac{1}{3ka}(\varphi_{31} + \varphi_{32})$$

A phase angle difference, as in equation (8) can be deduced from the phase angle in the product of the first complex number and the other conjugated:

$$\varphi_{31} = \text{Arg}(G_3 \cdot G_1{}^*) + n \cdot 2\pi$$
(10)
$$\varphi_{32} = \text{Arg}(G_3 \cdot G_2{}^*) + n \cdot 2\pi$$

where * means complex conjugate, and Arg (the argument) is a phase angle between $-\pi$ and π.

For fish in the main lobe of this transducer and between the -10 dB points, the phase angle difference in equation (8) is less than 160 degrees, which means that there is no 2π ambiguity; n=0.

In existing Simrad split-beam echo sounders, the complementary angle to v is often used

$$u_x = \pi/2 - v_x \qquad \sin u_x = \cos v_x$$
$$u_y = \pi/2 - v_y \qquad \sin u_y = \cos v_y$$

u_x and u_y are the angles from s to respectively the yz-plane and the xz-plane. Most split-beam transducers are narrow beam transducers, so that the approximation sinu=u is allowable in the main beam; and we have

$$u_x = \frac{1}{\sqrt{3}ka}(\varphi_{31} - \varphi_{32})$$
(11)

$$u_y = \frac{1}{3ka}(\varphi_{31} + \varphi_{32})$$

35

The angle sensitivity Λ is much used in existing split-beam echo sounders related to transducers with four sections. For a transducer with three sections the use of angle sensitivity is more dubious. However, in order to make use of existing programs in the echo sounder processor, we state a similar definition of the angle sensitivity

$$\Lambda = kd$$

where d is the distance between the centres of two of the sections

$$d = \sqrt{3} \cdot a$$

The signal processor in the receiver calculates two 'phase angles', φ_x and φ_y, although at least one of them, φ_y is fictive regarded as a phase angle. With the aid of equation (11) we have

$$\varphi_x = \Lambda u_x = kdu_x = \varphi_{31} - \varphi_{32} \tag{12}$$
$$\varphi_y = \Lambda u_y = kdu_y = (\varphi_{31} + \varphi_{32})/\sqrt{3}$$

φ_x and φ_y are transferred to the main processor, where the angle to the target is calculated as

$$u_x = \varphi_x / \Lambda \tag{13}$$
$$u_y = \varphi_y / \Lambda$$

For this transducer $\Lambda = \sqrt{3}ka = 18.3$

The coordinate system used here has the x-axis pointing port and the y-axis pointing ahead. The presentation on the echo sounder screen is a bird's eye view with the x-axis pointing starboard, so that a minus sign must be applied to u_x in formula (13)

It should be noted, that the amplitudes of the three signals are not equal. The three transducer sections are identical in geometrical form and tapering, but they are rotated 120 degrees relative to each other. The geometrical form of one section is a rhomb, and the beam pattern is not circular. Therefore, the amplitude of the three signals G1, G2 and G3 should not be used individually.

The sum of the three echo signals, G1+G2+G3 represents the echo received by the complete transducer area and is used for the presentation of the echo amplitude in the echogram, and in the target strength calculation.

Beam pattern compensation

The main lobe of the transducer ES 38-10 is circular. Thus it can be expressed as a function of v_z . The central part of the main lobe, between the -6 dB points, can as a good approximation be expressed by a second order function

$$B = -0.126\ v_z^2 \qquad\qquad (14)$$

where v_z is the angle from the z-axis in degrees
B is one-way beam pattern in dB

ES38-10 Beam pattern, transverse
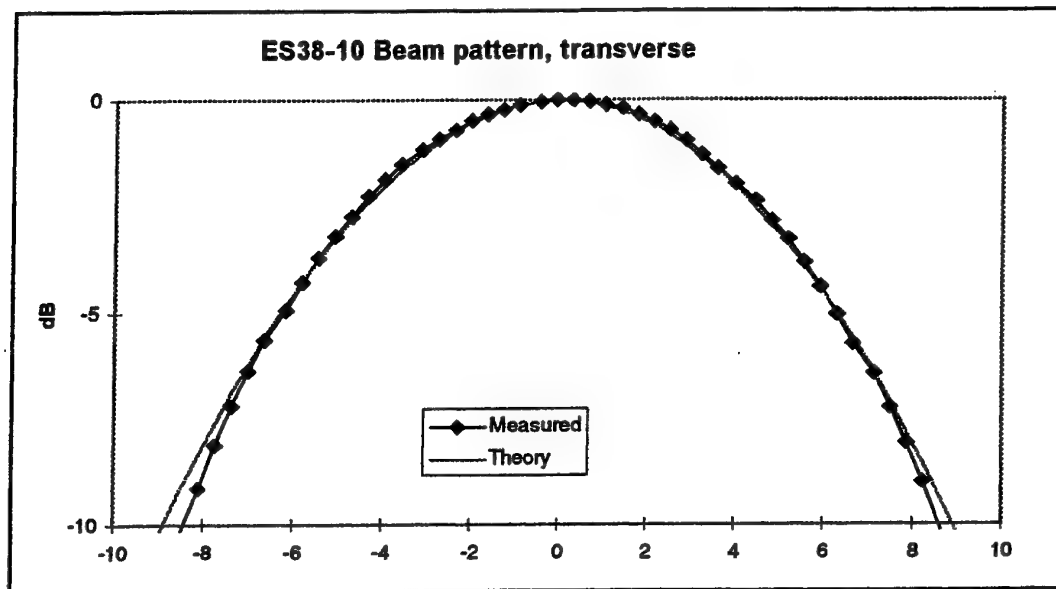
The three angles from **s** to the co-ordinate axes must obey

$$\cos^2 v_x + \cos^2 v_y + \cos^2 v_z = 1$$

and from this

$$\sin^2 v_z = 1 - \cos^2 v_z = \cos^2 v_x + \cos^2 v_y = \sin^2 u_x + \sin^2 u_y$$

For small angles with $\sin u = u$

$$v_z^2 = u_x^2 + u_y^2$$

$$B = -0.126 \cdot (u_x^2 + u_y^2)$$

Transducer design

The transducer has 48 tonpilz elements, positioned in a hexagonal pattern. Each tonpilz element is circular with a diameter of 35 mm, and the centre to centre distance is 36.5 mm. The 48 elements are electrically connected as three sections with 16 elements in each section. The transducer centre, origo, is a point between the three inner elements. The circumference of the 48 elements is six-sided, but it is not regular. The sides have 4 or 5 elements. The three sections are numbered from 1 to 3:

section 1,   starboard aft
section 2,   port aft
section 3,   forward

The transducer elements are fixed by polyurethane foam. This is a well-established and low cost technology.

FORWARD

birds-eye view
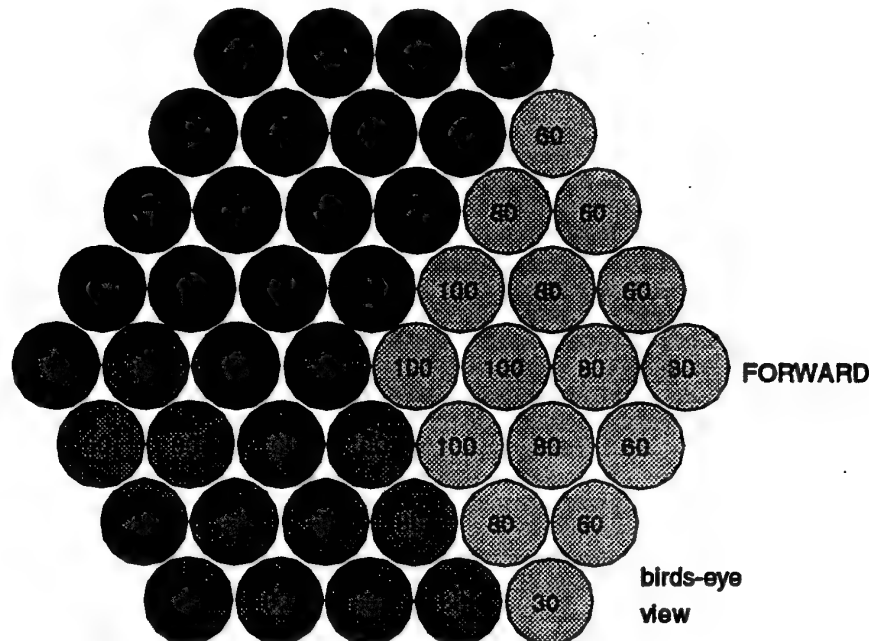
Transformers

Three transformers, one for each section, are placed in the transducer, behind the tonpilz elements. The transformers tune the capacitive component in the transducer impedance, and transform the impedance to 75 ohms, which matches the impedance of the transducer cable. In addition the transformer is used for amplitude tapering of the transducer elements in order to lower the side lobes. The secondary side of the transformer, towards the elements, has four taps for tapering of the elements. The voltage levels are shown on the drawing. For a split-beam transducer it is essential to avoid that a large fish in a side lobe is taken for a small fish in the main lobe. The penalty for a strong tapering is a

wider beam and limited input power due to cavitation at the transducer centre. With the chosen tapering 1500 W may be applied without cavitation at 3 m depth.

Transducer housing
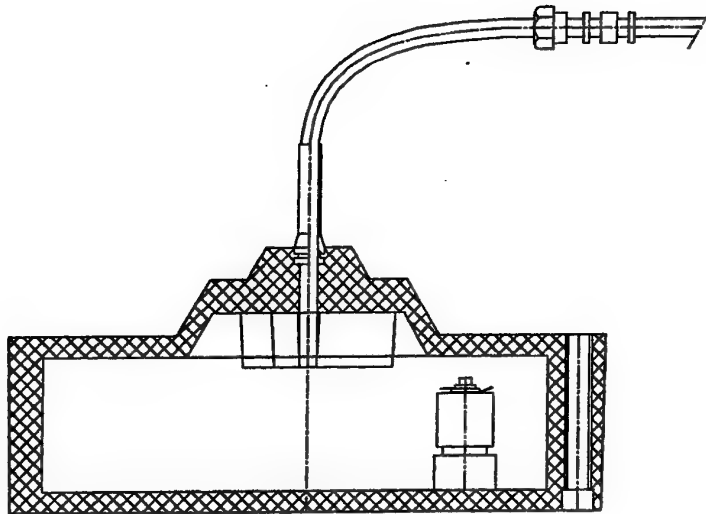
The unit with the tonpilz elements in foam is completely encapsulated in a polyurethane mould, which makes a robust and watertight housing. The transducer housing is circular for easy installation into a blister on the vessel hull. The transducer is mounted with 6 bolts through holes in the transducer periphery. The holes are lined with sleeves of stainless steel, so that the bolts can be tighten securely, metal against metal. A steel mounting ring has to be welded into the blister, before the transducer is installed.

Analyses of electric measurements on piezoelectric disks using FE-modeling

Rune Fardal and Magne Vestrheim

Department of Physics, University of Bergen, Allégaten 55, N-5007 Bergen

Abstract

Finite element (FE) simulations have been compared with classical "Mason" type of models and measurements for electrical response functions of piezoelectric disks. It is shown how a relative converged accuracy of the FE simulations better than the relative resolution of the measurements for both frequencies and response values for the first radial modes of the disk can be obtained. The results of some analyses using the FE model with adjusted constants are given, particularly for the lower radial modes frequency range. Some observations on the effects of frequency dependent dielectric constants are also given.

1. Introduction

For more than 100 years a lot of work has been done on trying to understand and simulate the behaviour of piezoelectric elements. For some specific resonance modes simplified and one-dimensional analytical models may be available, such as the much used "Mason" type of models for thickness extensional (TE) [1,2] and radial (R) [2,3] modes. One way to describe the various material loss effects is through the use of complex elastic, dielectric and piezoelectric material constants, where the imaginary parts are associated with the losses [4]. As these solutions are valid only under idealizing assumptions, the models can not describe the whole mode spectrum including the coupling of the modes for practical finite dimensions of the elements. More recently, numerical finite element models have become available also for piezoelectric structures [5,6,7]. Such models have been shown to provide a far more complete and accurate description of piezoelectric elements and piezoelectric transducer constructions. However, the use of such models for accurate simulations is still limited due to limited information being available for the material constants involved, and also due to limitations in the present understanding and applications of how the different constants affects the element vibrations.

In the present work a finite element (FE) model [7] will be used for giving some examples on analyses of electric measurement data for a single piezoelectric disk made of Morgan Matroc PZT-5A material [8]. The disk is denoted "disk 21", and the diameter, D, is 40.10 mm and the thickness, T, with electrodes is 1.989 mm, see Fig. 1. The diameter over thickness (D/T) ratio is thus 20.1601. Such high D/T ratios are required for using TE and R modes in methods for determining material constants according to recommendations given in e.g. the IEEE Std. 176 [2]. It is important that the numerical uncertainty of the FE model calculations will be well below the measurement resolution in order that numerical artifacts are not introduced in the comparisons with experimental data. This aspect is given particular attention here, and some results are discussed in Secs. 3 and 4. Further, the use of the FE model for a more detailed analysis of the electrical measurements of disk properties is discussed in Sec. 5.
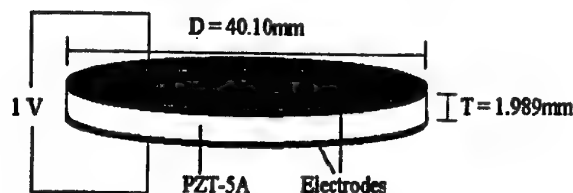
Fig. 1. *The disk 21 on which the electrical measurements and simulations have been performed.*

An example of typical electrical measurements of the conductance of the disk 21 is shown in Fig. 2 together with simulation results using the "Mason" type of model for radial modes. Fig. 3 shows the same measurements together with results using the "Mason" type of model for TE modes. In Fig. 4 the measurement

data are compared with results using FE simulations. Note that logarithmic scales are used along the two axes in order to represent the large span in frequency and conductance values involved. For the first radial modes a reasonable agreement with the radial modes theory is illustrated. Also a reasonable agreement is shown with Mason TE model at the first TE mode in Fig. 3. The limitations of the two models used in Figs. 2 and 3 are clearly seen even for a disk with such a high D/T ratio. The FE model is shown to provide at least a more complete qualitative description of the vibrations of the disk. The quantitative accuracy in the simulations may be limited through the limited knowledge available concerning the material constants, and the limited amount of adjustments being done here for the results shown. This is one of the main motivations for this type of adjustments; if the constants are not given with the desired accuracy, simulations on piezoelectric elements and transducer constructions will be inaccurate and often useless for practical purposes [9]. Further details on the models and the data used will be found in Secs. 2 and 5.
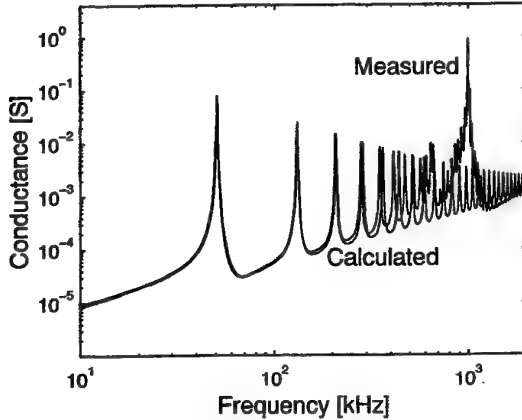
Fig. 2. *Comparison between measured conductance and calculations using Eq. (1).*
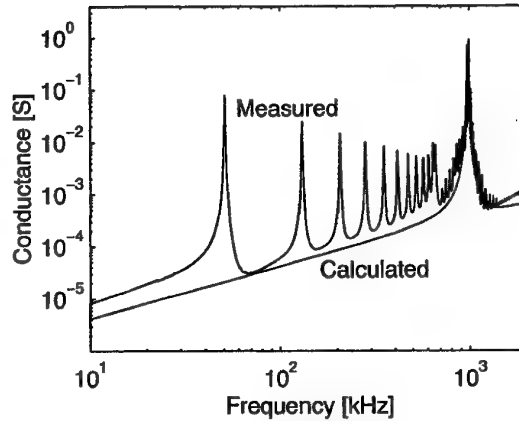
Fig. 3. *Comparison between measured conductance and calculations using Eq. (7).*
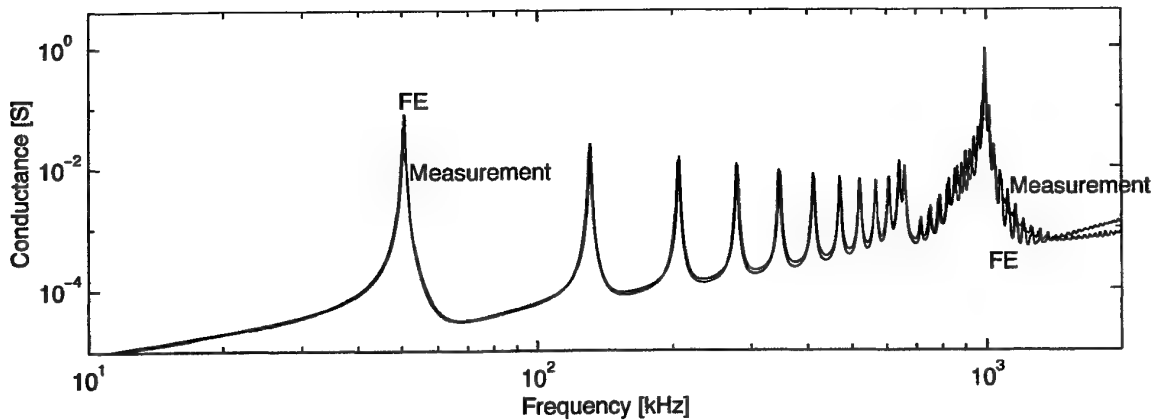
Fig. 4. *Comparison between measured conductance and calculations using FE simulations.*

2. Theory and measurements

The "Mason" type of model used to describe the R modes in Fig. 2 in the introduction is given by the following expression for the electrical admittance, Y [10],

$$Y(\omega) = G + iB = i\omega \left\{ 1 - \frac{2\left(\hat{k}^p\right)^2}{1 - \hat{\sigma}^p - \Im\left(\omega a / \sqrt{\hat{c}_{11}^p / \rho}\right)} \right\} \frac{\pi a^2 \hat{\varepsilon}_{33}^p}{T}. \tag{1}$$

In Eq. (1) G is the conductance and B is the susceptance of the element. $\Im(x) = x J_0(x)/J_1(x)$ is called the "Ono's" function, a = D/2 is the radius of the disk, ρ is the density of the piezoelectric material, and " ^ " is used for

denoting complex constants. The constants used in this model are derived from the set of constants used in the FE simulations, see Table 1, by [2],

$$\hat{c}_{11}^{P} = \hat{c}_{11}^{E} \frac{\left(\hat{c}_{13}^{E}\right)^{2}}{\hat{c}_{33}^{E}}, \qquad \qquad \hat{\sigma}^{P} = \frac{-\hat{s}_{12}^{E}}{\hat{s}_{11}^{E}}, \qquad (2),(3)$$

$$\hat{\varepsilon}_{33}^{P} = \hat{\varepsilon}_{33}^{S} + \frac{\left(\hat{e}_{33}\right)^{2}}{\hat{c}_{33}^{E}}, \qquad \hat{k}^{P} = \frac{\hat{e}_{31}^{p}}{\sqrt{\hat{c}_{11}^{P}\hat{\varepsilon}_{33}^{P}}}, \qquad \hat{e}_{31}^{p} = \hat{e}_{31} - \frac{\hat{e}_{33}\hat{c}_{13}^{E}}{\hat{c}_{33}^{E}}. \qquad (4),(5),(6)$$

Here the compliance constant matrix, [s], is derived from the stiffness constant matrix, [c], [s] = [c]$^{-1}$ [2].

The "Mason" model used to describe the TE modes in Fig. 3, is given by the following expression for the electrical impedance, Z [11],

$$Z(\omega) = R + iX = \left\{1 - \hat{k}_{t}^{2} \frac{\tan\left(\omega T \sqrt{\rho / \hat{c}_{33}^{D}}/2\right)}{\omega T \sqrt{\rho / \hat{c}_{33}^{D}}/2}\right\} \frac{T}{i\omega \pi a^{2} \hat{\varepsilon}_{33}^{s}}. \qquad (7)$$

In Eq. (7) R is the resistance and X is the reactance of the element. The constants used in Eq. (7) are derived from the set of constants used in the FE simulations as given in Table 1, by [2],

$$\hat{k}_{t}^{2} = 1 - \frac{\hat{c}_{33}^{E}}{\hat{c}_{33}^{D}}, \qquad \qquad \hat{c}_{33}^{D} = \hat{c}_{33}^{E} + \frac{\hat{e}_{33}^{2}}{\hat{\varepsilon}_{33}^{S}}. \qquad (8),(9)$$

All the constants used and given in Table 1 have the same definitions as in [2], except that complex constants are being used here to include losses.

The program FEMP version 3.0 [7] has been used for the FE simulations in the present work. The program can calculate eigenmodes, eigenmode resonance spectra [12], element displacements, electrical response functions, and also sound field radiation into different media and sensitivity response functions. Front- and backing layers in more complicated transducer structures, can be included [7]. Two different methods, the direct time harmonic method and the mode superposition method, for calculating the response functions are implemented in the FE model used [7]. When using the direct method, the response functions are calculated directly from the FE equations using matrix manipulation. For the mode superposition method the response functions are calculated by summing the contributions to the response for all eigenmodes up to a maximum frequency, f_{max} [7]. The number of elements per shear wavelength, N_s, of sound waves in the radial and thickness directions of the disk at given frequencies will influence on the accuracy obtained in the simulations. For the mode superposition method f_{max} also affects the accuracy. Various number of elements and maximum frequency has been chosen in the different examples in the present work. Convergence tests of the convergence accuracy using the FEMP 3.0 program are shown in Sec. 4.

The electric measurements on the disk have been performed using a Hewlet Packard 4192A impedance analyzer. The impedance analyzer has been controlled from, and the measurements have been logged on a PC via a standard IEEE488-bus and a Matlab program. A vertical holder with little mechanical loading but good electric contact has been used to hold the disk. Different frequency resolutions have been chosen in the different examples presented here (see Sec. 5)

3. Accuracy needed for the FE simulations

In Fig. 5 a typical measurement series close to the first radial mode is shown to give an example on practical measurement resolution both in frequency and conductance value (similar results for the susceptance has not been shown here for simplification). A measurement resolution of 1 Hz has been used for the frequency. The series resonance frequency for maximum G [2] is found at 50.531 kHz with a relative resolution in the determined resonance frequency of the order of 10 ppm. The resolution of the measurements of the conductance value is 0.01 mS for the measurements shown, which represents a relative resolution of the order of 20 ppm. (Note that in the present work the absolute uncertainty of the measurements will not be considered or used).

42

When comparing with measurements it is important that the FE calculations can be done at a higher accuracy then the measurement resolution, in order to ensure that significant variations in the responses are not due to calculation errors. Thus the considerations of the measurement data show that an accuracy of the order of 1 ppm is of interest both with respect to resonance frequencies and the response function values. How such numerical accuracies can be achieved in the FE simulations will be discussed in the following section.

4. Convergence

Convergence tests for the FE simulations are used to show that a converged accuracy of 1ppm can be obtained for the first radial resonance frequencies in both frequency and value. Such convergence tests have been performed on the three first radial resonance frequencies for both frequencies and conductance values and also for the region below the first radial serial resonance. The converged accuracy is found for both the direct and the mode superposition method. Convergence tests are performed by specifying and varying N_s for both methods. In [7] it has been found to be reasonable to choose the same number, N_s, in both radial and thickness directions. For the mode superposition method convergence tests by variations of f_{max} has been performed as well.

In Fig. 6 f_{max} for the mode superposition method at the radial modes R1, R2 and R3 has been chosen to be approximately twice the respective resonance frequencies $f_{SR1} \approx 50$ kHz, $f_{SR2} \approx 128$ kHz and $f_{SR3} \approx 201$ kHz. For the direct method only the converged accuracy at f_{SR1} has been shown. N_s at f_{SR1}, f_{SR2}, or f_{SR3} are varied from $N_S = 2$ to $N_S = 50$ in both the radial and the thickness directions and the deviation in frequency relative to the frequency found using 50 elements per shear wavelength, $(f_{SR1,NS} - f_{SR1,N50})/ f_{SR1,N50}$, is calculated. 1 ppm converged accuracy is reached at N_S approximately 12, 18 and 20 elements pr shear wavelength, respectively, at the three resonances for the mode superposition method. For the direct method, 1 ppm converged accuracy is reached at $N_S = 9$. In these examples a frequency resolution of 0.01 Hz has been used at R1 and R2, and 0.1 Hz at R3. This resolution makes it possible to detect relative differences in frequency of approximately 0.1 ppm.

In Fig. 7 the deviation in conductance values at the resonance frequencies relative to the conductance found using 50 elements per shear wavelength at the resonance frequencies is calculated as a function of N_S. Convergence tests when varying f_{max} for the mode superposition method has shown that the conductance value shows no sign of converging even for $f_{max} = 1.5$ MHz. This means that for the example in Fig. 7 the conductance value is converging for the mode superposition method, but towards the wrong value. When using $N_S = 50$ at R1, the conductance value for the two methods deviate with 152 ppm when $f_{max} = 100$ kHz. For the direct method f_{max} is of no influence, and the conductance is converging towards the correct theoretical conductance value.

Fig. 6. *Deviation in frequency for the three first radial resonances relative to the frequency found using 50 elements per shear wavelength.*

Fig. 7. *Deviation in conductance values for the three first radial resonances relative to the values found using 50 elements per shear wavelength.*
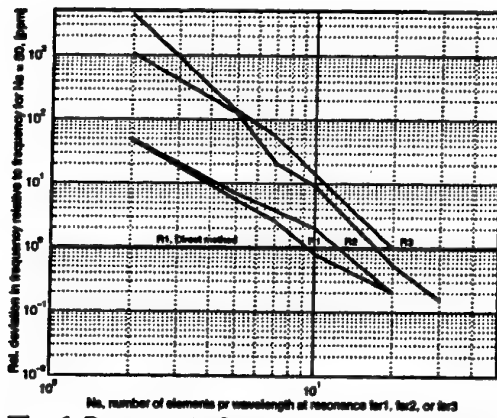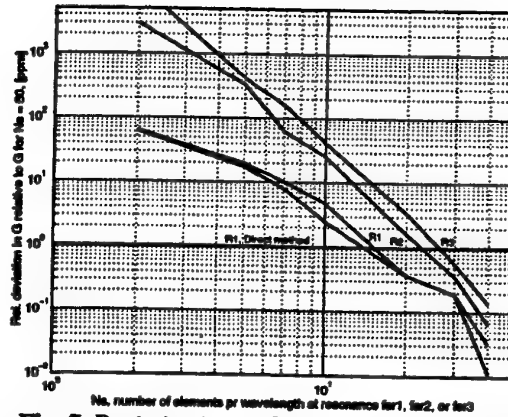
When using the mode superposition method this is only a problem for the conductance values and not for the frequencies. The convergence is seen to be a little slower for the conductance in Fig. 7 than for the resonance frequencies in Fig. 6, and a 1 ppm converged accuracy is reached at N_S of approximately 16, 22 and 28 elements per shear wavelength, respectively, at the three resonances for the mode superposition method. For the direct method, 1 ppm converged accuracy is reached at $N_S \approx 13$.

With the exception of the convergence for the conductance as a function of f_{max} for the mode superposition method all tests show 1 ppm converged accuracy with less than 28 elements per wavelength at the frequencies tested. It is of no problem to calculate with this number of elements at these frequencies using a PC with a 550 MHz processor and 256 MB of internal memory. 1 ppm converged accuracy is therefore fully achievable both for frequency and conductance values at the first radial modes and for the conductance values at the lower frequencies. Another question is of course whether the FE model simulates the response functions physically correctly to such an accuracy. The FE model used in this work has been compared with other commercial FE models with a good agreement [13]. But only detailed comparisons with measurements at a sufficiently high accuracy can tell how accurate the FE model really is. Such an endeavor has not been attempted here.

5. Analyses

In the FE simulations shown in Fig. 4 the direct method with $N_S = 4$ at 2 MHz was used to obtain the conductance response. To get the agreement shown it was necessary to adjust the constants used in the FE simulations. It should be noted that all the adjustments done in this section are partly of a "serendipity type", as a full understanding of how the different constants affect the response functions at a high accuracy is lacking. Thus the values of the constants arrived at through the adjustments are not necessarily the physically correct values. Variations were done using as a starting point a FE set of real constants found in Chapter 5 in [14] to approach a radial mode set of complex constants derived by Eqs. (2)-(6), as also found in [14], Table 6.5. Thus the approach is to first obtain an adjustment in the low frequency radial modes range based on adjusting the four planar constants $\hat{\varepsilon}_{33}^P$, $\hat{c}_{11}^P$, $\hat{\sigma}^P$ and $\hat{k}^P$ in the radial modes model in Eq. (1). In this process $\hat{c}_{11}^E$ was adjusted to get matching of $\hat{c}_{11}^P$, $\hat{\varepsilon}_{33}^S$ was adjusted to get matching of $\hat{\varepsilon}_{33}^P$, $\hat{e}_{31}$ was adjusted to get matching of $\hat{k}^P$, and $\hat{c}_{12}^E$ was adjusted to get matching of $\hat{\sigma}^P$. The piezoelectric constants, e, were all assumed to be real before any adjustments were performed, but a complex $\hat{e}_{31}$ has been chosen here to adjust $\hat{k}^P$, while e_{33} and e_{15} were kept real. To get an even better agreement with the measurements for the first R-modes as seen in Figs. 8 and 9, more accurate adjustments of the real part of $\hat{c}_{11}^E$ and the imaginary part of $\hat{c}_{12}^E$ were performed. It is these adjusted constants and the constants derived from these which are given in Table 1 and which have been used in the simulations for all of the Figs. 2, 3, 4, 8 and 9. It must be stressed that these adjustments only show one possible way to get better agreement between the simulations and the measurements, and is not necessarily the physically correct choice, as noted above.

Table 1. *The material constants needed in the FE-simulation, R-mode simulations and TE-mode simulations. The 'PZT-5A' column is constant values given by Morgan Matroc [8]. The last column shows the adjusted constant*

44

values that are used in the simulations. The R and TE -mode constants are derived from the FE-set of constants by Eqs. (2)-(6) and Eqs. (8) and (9).

Symbol FE-const.	Unit	PZT-5A	Adjusted constants	Symbol R-modes	Unit	PZT-5A	Adj. constants Derived values
ρ	kg/m³	7750	7740	$\hat{\varepsilon}^p_{33}/\varepsilon_0$	-	-	$1040\times(1-i/93)$
$\hat{\varepsilon}^S_{11}/\varepsilon_0$	-	916	$916\times(1-i/50)$	$\hat{k}^p$	-	-0.60	$-0.5834\times(1-i/122)$
$\hat{\varepsilon}^S_{33}/\varepsilon_0$	-	830	$825\times(1-i/92)$	$\hat{c}^p_{11}$	10^{10} N/m²	-	$7.25308\times(1+i/98)$
$\hat{e}_{31}$	C/m²	-5.4	$-5.59\times(1-i/44)$	$\hat{\sigma}^p$		-	$0.3541\times(1-i/485)$
e_{33}	"	15.8	14.79	**TE-modes**			**Derived values**
e_{15}	"	12.3	12.3	$\hat{\varepsilon}^S_{33}/\varepsilon_0$	-	830	$825\times(1-i/92)$
$\hat{c}^E_{11}$	10^{10} N/m²	12.1	$10.9835\times(1+i/98)$	$\hat{k}_t$	-	0.48	$0.454\times(1+i/3788)$
$\hat{c}^E_{12}$	"	7.54	$7.30\times(1+i/106.732)$	$\hat{c}^D_{33}$	10^{10} N/m²	14.7	$14.506\times(1+i/97)$
$\hat{c}^E_{13}$	"	7.52	$7.38\times(1+i/98)$				
$\hat{c}^E_{33}$	"	11.1	$11.51\times(1+i/98)$				
$\hat{c}^E_{44}$	"	2.11	$2.11\times(1+i/98)$				
$\tan\delta$	-	0.02	-				
Q_M	-	75	-				

More detailed comparisons around R1 in Figs. 8 and 9 show that using the derived sets of constants, the radial model results are shifted a little above the FE simulations in frequency as is also to be expected. In the Mason model an infinitely large and thin plate is assumed, and deviations between the FE simulations and the results from the radial modes model can be seen even for D/T = 20. This deviation will be larger for the higher R-modes as seen in Fig. 3. A Rayleigh type of correction [15] could be used to reduce this problem, but the IEEE 176-1987 standard [2] does not recommend the use of such a Rayleigh correction when the main intention of the measurements is the determination of material constants. For the FE simulations in Figs. 8 and 9 the direct method for calculating the conductance with N_S = 20 at 50 kHz has been used. For the measured data in Figs. 8 and 9 a limited frequency resolution of 20 Hz has been used. A much better frequency resolution, such as the 1 Hz resolution used for Fig. 5 could have been used to obtain a smoother and more accurate conductance curve. (Less accurate results using a resolution of 100 Hz are given in Figs. 2, 3, and 4). It should be mentioned that if these comparisons had been done using the constant values provided by Morgan Matroc [8], much larger deviations from the measurements would have been observed. It should also be noted that no possible effects from finite electrode thickness have been included in the present analyses.
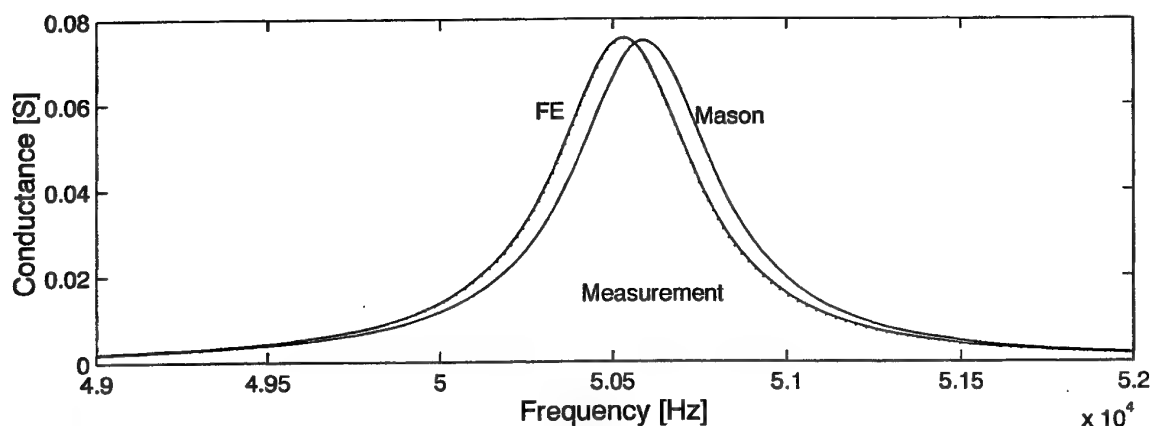

Fig. 8. *Comparisons between measured conductance (dotted line), simulations using the Mason radial mode model, and simulations using FE.*
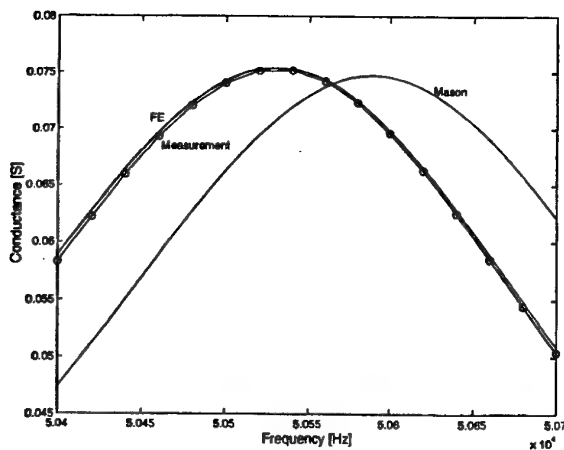
Fig. 9. *Comparisons between measured conductance (dotted line), simulations using the Mason radial mode model, and simulations using FE.*
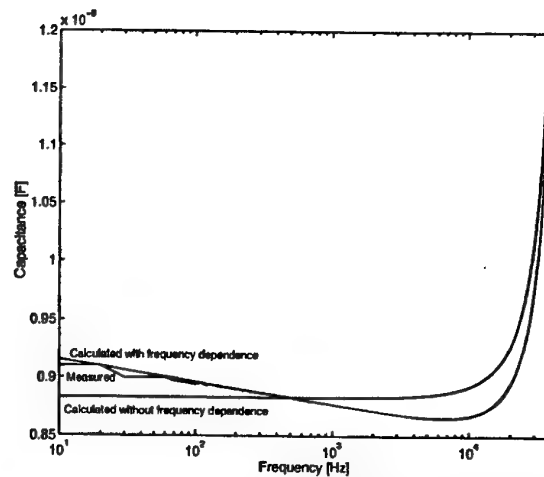
Fig. 10. *Measured capacitance and simulations with and without frequency dependence using the Mason radial mode model.*

If the response is plotted on the form of capacitance (B/ω), the effects of a frequency dependent dielectric material constant can be seen. For the Mason model it is easy to implement such a frequency dependence. In Fig. 10 the measured and calculated capacitance is plotted without and with a frequency dependent ε^T_{33}. ε^T_{33} has been fitted at 500 Hz and reduced by 2.05% per frequency decade to fit the trend in the experimental data. Morgan Matroc [8] gives a frequency dependence of ε^T_{33} to be -2,4% per frequency decade. This effect of frequency dependence is shown for the low frequency range in Fig. 10, but is also expected to give further deviations between measurements and simulations for higher frequencies as well. Until now, no FE simulations including such frequency dependent constants has been performed.

6. Conclusions

The FE simulations of the electrical response functions for piezoelectric disks are seen to give a much better overall agreement with the measurements compared to the classical "Mason" type of models. The FE model has been shown to be capable of calculations at a higher converged accuracy than the resolution of the measurements for the frequency range of the first radial modes and below. This enables very accurate adjustments of the material constants that describes the piezoelectric disk by comparison between measurements and simulations of the electrical response functions. More extensive FE analyses of the behaviour of piezoelectric elements, will benefit from further detailed work on studying the effects of the different specific material constants on the element vibrations.

Acknowledgements

References

1. W. P. Mason, *Electromechanical Transducers and wave filters* (Van Nostrand, New York, 1948), 2nd ed.
2. ANSII/IEEE std 176-1987, "IEEE standard on piezoelectricity". The Institute of Electrical and Electronics Engineers, Inc., New York (1988).
3. W. P Mason, "Electrostrictive effect in barium titanate ceramics", Phys Rev. 74(9), 1134-1147 (1948).
4. R. Holland, "Representation of dielectric, elastic, and piezoelectric losses by complex coefficients", IEEE Trans. Sonics and Ultrasonics, SU-14(1), 18-20 (1967).
5. H. Allik and T. J. R. Huges, "Finite element method for piezoelectric vibration", Int. J. Num. Meth. Eng. 2, 151-157 (1970).
6. H. Allik, K. M. Webman, and J. T. Hunt, "Vibrational response of sonar transducers using piezoelectric finite elements", J. Acoust. Soc. Am. 56, 1782-1791

7. J. Kocbach, "Finite Element Modeling of Ultrasonic Piezoelectric Transducers". Thesis for the dr. scient. degree. Dept. of Physics, University of Bergen (2000).

8. "Five modern Piezoelectric Ceramics", Bulletin 660011/F, (Vernitron Piezoelectric Division, 232 Forbes Road, Bedford, England.).

9. M. Vestrheim, F. Atterås and R. Fardal, "Material constants of piezoceramic materials", in *Proc. of the 23rd Scandinavian Symposium in Physichal Acoustics*, Ustaoset, Norway, edited by U. R. Kristiansen Scientific/Technical Report, No. 420003, Dept. of Telecommunications, Norwegian University of Science and Technology, 37-38 (2000).

10. Sherrit S., Gauthier N., Wiederick H.D and Mukherje B.K. "Accurate evaluation of the real and imaginary material constants for a piezoelectric resonator in the radial mode", Ferroelectrics, **119**, 17-32 (1991).

11. Sherrit S., Wiederick H.D and Mukherje B.K., "Non-iterative evaluation of the real and imaginary material constants of piezoelectric resonators". Ferroelectrics, **134**, 111-119 (1992).

12. J. Kocbach, P. Lunde, M. Vestrheim, "Tables of resonance frequencies for disks of PZT-5A, PZT-5H, $Pb(ZrTi)O_3$, $BaTiO_3$ and $PbTiO_3$", Scientific/Technical Report, No. 2000-07, Department of Physics, University of Bergen.

13. J. Kocbach, P. Lunde, M. Vestrheim, " FEMP – Finite Element Modeling of Piezoelectric Structures Theory and Verification for Piezoceramic Disks", Scientific/Technical Report, No. 1999-07, Department of Physics, University of Bergen.

14. F. Atterås, "Materialkonstantar for Piezokeramiske Elementer". Thesis for the cand. scient. degree (in Norwegian). Dept. of Physics, University of Bergen (1998).

15. IRE *Standards on Piezoelectric Crystals: Measurements of Piezoelectric Ceramics*, 1961, (proceedings of the IRE, Vol. **49**, 1161-1169, (1961).

Ultrasonic scattering from liquid droplets in a wet gas

Andrew C Baker, Kjell-Eivind Frøysa, Hilde Furset and Per Lunde

Christian Michelsen Research AS
Fantoftvegen 38, Postboks 6031
N-5892 Bergen, Norway
E-mail: andrew.baker@cmr.no

Ultrasonic flowmeters are increasingly being used in the fiscal metering of dry natural gas. Typically such meters are in the size range of 6 to 40" diameter and can offer accuracy of 0.5 % or better. Currently there is much interest in the development of this technology for use in the metering of wet natural gas. This presents several challenges if good accuracy is to be maintained. This abstract describes one aspect of the development of ultrasonic wet gas metering, that is the measurement of ultrasonic scattering from liquid droplets and mist carried in the gas. This work is part of a 3-year project jointly funded by Kongsberg Offshore, Statoil, Norsk Hydro, Phillips Norge and the Norwegian Research Council (NFR).

A considerable amount of literature exists on the many theoretical models for ultrasonic scattering from single scatterers and clouds of scatterers. These models have been tested widely against experimental measurements in the fields of underwater acoustics and medical ultrasound where the continuous medium is liquid and the dispersed medium is a gas or a solid. There have also been comparisons of such theoretical models in emulsions. Although there is no reason to suspect that the theoretical models are inapplicable to the gas-continuous case, there is a dearth of publications in the open literature on measurements of ultrasonic scattering from liquid droplets or mist in suspension in a gas.

In this study we have attempted measurements of ultrasonic scattering (side scatter and backscatter) on a wide range of droplet sizes (1 micron to 8 mm diameter) and liquid volume fractions (10 – 1155 parts per million) for ultrasonic frequencies in the range 50 to 300 kHz.

Measurements of side scatter and back scatter made on single plastic spherical beads (diameters in the range 3 to 8 mm) showed good agreement with theoretical predictions (within the measurement uncertainty of about 2 dB). Measurements of back scatter from a liquid mist (droplet diameters 33 – 52 micron) gave scattering levels some 15 to 20 higher than predicted. It is speculated that the discrepancy could be due to interface effects at the boundaries of the mist filled region and/or scattering from turbulence caused by the spray nozzles used to generate the liquid mist. One of the main difficulties of such measurements is generation of a well characterised mist, the two main parameters of interest being the droplet diameters and the volume fraction occupied. In an effort to create a well defined scattering medium an array of spherical plastic beads (4 mm diam) suspended on fine wires was built. The beads were placed in a random pattern and the suspension wires were small enough that they didn't make a significant contribution to the scattered field. Back scattering measurements made on this random array showed better agreement with theory

(within about 5 dB) but the difference was still outside of the calculated range of the expanded total uncertainty.

It is important to obtain good experimental measurements in order to verify the candidate theoretical models. Such theoretical models will then have the advantage that they offer greater flexibility and are easy to apply under conditions where good experimental measurements would be difficult to obtain, e.g. at high pressures and temperatures.

A. C. Baker, 15 March 2001.

Ultrasonic Reciprocal Transducer Systems and Flow Measurement

M. Willatzen
Mads Clausen Institute for Product Innovation
University of Southern Denmark
Grundtvigs Alle 150
DK-6400 Sønderborg, Denmark
Tel: +45 65 50 16 82
email: willatzen@mci.sdu.dk

Abstract

A one-dimensional description of reciprocal ultrasound systems is described. The model allows near- and far-field characteristics to be evaluated under various excitation and electrical loading conditions. Numerical results are obtained for reciprocal transducer systems of interest for flow meter district-heating applications using transducers with half-wavelength thick stainless steel matching layers. Good agreement with measurements is found.

1 The piezoelectric plate transducer operated in thickness mode

The following discussion is restricted to piezoelectric transducers in the form of a thin cylinder. We shall assume that the piezoelectric transducer is operated in thickness mode. Under these simplifying circumstances, the general 3D piezoelectric equations degenerate into:

$$D = dT + \epsilon^T E \tag{1}$$

$$E = \beta^T D - gT \tag{2}$$

$$D = \epsilon^S E + eS \tag{3}$$

$$E = \beta^S D - hS \tag{4}$$

$$S = dE + s^E T \tag{5}$$

$$T = -eE + c^E S \tag{6}$$

$$S = gD + s^D T \tag{7}$$

$$T = -hD + c^D S. \tag{8}$$

It should be mentioned that two *independent* relations, e.g., Eqs. (3) and (8), suffice to describe the one-dimensional problem. The rest, Eqs. (1)-(2) and (4)-(7), are just alternative representations of Eqs. (3) and (8) in different variables.

2 Dynamic operation

Newton's Second Law, Poisson's Law, and the definition of strain completely determine the temporal and spatial behavior of the resulting strains, stresses, velocities, currents, and voltages in the transmitter and receiver transducers when invoking the appropriate mechanical boundary conditions and subsidiary electromechanical conditions (e.g., the coupling between applied voltage and electric displacement, transducer electrode velocities). In this section, the one-dimensional modeling equations accounting for the dynamic response of a multilayer transmitter-receiver piezoelectric transducer setup will be derived.

Newton's Second Law applied to an infinitesimal slab of width dz can be stated as [4]:

$$\rho A dz \frac{\partial u}{\partial t} = (F_z - F_{z+dz}) = -AT_z + AT_{z+dz} = A\frac{\partial T}{\partial z}dz, \tag{9}$$

where u is the particle velocity, ρ is the mass density, A is the cross-sectional area, and F_z is the force on the slab at position z. Eq. (9) is equivalent to:

$$\rho\frac{\partial u}{\partial t} = \frac{\partial T}{\partial z}, \tag{10}$$

and from the definition of strain in the one-dimensional case: $S = \frac{\partial \zeta}{\partial z}$ it is found that

$$\frac{\partial u}{\partial z} = \frac{\partial\left(\frac{\partial \zeta}{\partial t}\right)}{\partial z} = \frac{\partial}{\partial t}\frac{\partial \zeta}{\partial z} = \frac{\partial S}{\partial t}, \tag{11}$$

where ζ is the z-coordinate displacement. Equations (10-11) are the basic (one-dimensional) equations describing the dynamics of a piezoelectric material and, of course, an ordinary (non-piezoelectric) material. Accordingly, these equations apply to a multilayer transducer consisting of a piezoceramic material as well as ordinary materials. It is convenient to cast Eqs.(10-11) in a different form by use of the Poisson Equation:

$$\frac{\partial D}{\partial z} = \rho_{free} = 0, \tag{12}$$

and Eq.(8) implying:

$$\rho\frac{\partial u}{\partial t} = c^D \frac{\partial S}{\partial z} \tag{13}$$

$$\frac{\partial u}{\partial z} = \frac{\partial S}{\partial t}. \tag{14}$$

In Eq.(12), ρ_{free} denotes the external (or free) charge density, which is zero everywhere within the multilayer transducer except on the electrodes. Eqs. (13) and (14) therefore apply to the piezoceramic layer as well acoustic coupling layers and matching layers.

The voltage of the transmitting voltage source is related to the electric field between the electrode plates as follows:

$$V(t) = Z_{e1}I + \int_{z_L}^{z_1} E(z,t)dz, \tag{15}$$

where z_L and z_1 are the left and right ceramic plate positions of the transmitter multilayer structure, respectively (see Fig.1), Z_{e1} represents any complex electrical impedance in series with the pulse generator and the transmitting transducer, and I is the current. The impedance Z_{e1} may account for internal electrical impedances in the pulse generator as well as external ohmic resistors and/or inductive or capacitive impedances. The loads on the left and right boundaries of the transmitter are considered to be air and water, respectively.

Differentiating Eq.(15) with respect to time and making use of Eqs. (4), (12), and (14) leads to (keeping in mind the relation between current and electric displacement: $I = A\frac{\partial D}{\partial t}$):

$$\frac{\partial V}{\partial t} = AZ_{e1}\frac{\partial^2 D}{\partial t^2} + \frac{l_1}{\epsilon_1^S}\frac{\partial D}{\partial t} - h\left[u(z_1) - u(z_L)\right], \tag{16}$$

where A denotes the cross-sectional area of the piezoceramic material. Eq. (16) is the electromechanical subsidiary condition needed for the transmitter. An equation similar to Eq. (16) can be written down for the receiver; refer to Eq. (34) and Fig.2.

The set of equations: (13), (14), (16) and continuity of the (normal) velocity and pressure between layers and surrounding media completely specify the problem to be solved. However, before stating these conditions explicitly, some further discussions will be carried out. Firstly, notice that Eqs.(13) and (14) can be augmented in S and u, respectively, to yield:

$$\frac{\partial^2 u}{\partial t^2} - v_a^2\frac{\partial^2 u}{\partial z^2} = 0 \tag{17}$$

$$\frac{\partial^2 S}{\partial t^2} - v_a^2\frac{\partial^2 S}{\partial z^2} = 0, \tag{18}$$

where $v_a = \sqrt{\frac{c^D}{\rho}}$ is the layer-dependent sound velocity, i.e., it depends on the position coordinate z for a multilayer structure.
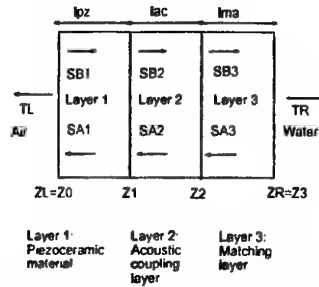
Figure 1: Schematic transducer geometry, transmitter.

In the present work, the multilayer structure is assumed to consist of a piezoceramic material (thickness l_{pz}), an acoustic coupling layer (e.g., grease, thickness l_{ac}), and a matching layer (thickness l_{ma}). To simplify matters, we have disregarded the thicknesses of the plate electrode layers in this example but the arguments involved can easily be extended to any multilayer transducer consisting of an arbitrary number of layers and thicknesses. In fact, it has been verified numerically [5] that a few microns thick electrode layer has very little or no effect on results.

2.1 Solving transducer dynamic equations by use of Fourier analysis

The formulation of boundary conditions are conveniently done for each frequency component at a time. Applying Fourier analysis to the generator input voltage is the standard method which will be

used here. A general excitation voltage $V(t)$, provided by the pulse generator, can be decomposed into its Fourier components $V(\omega)$ according to:

$$V(t) = \frac{1}{\sqrt{2\pi}} \int_{-\infty}^{\infty} V(\omega) \exp(-i\omega t) d\omega \tag{19}$$

$$V(\omega) = \frac{1}{\sqrt{2\pi}} \int_{-\infty}^{\infty} V(t) \exp(i\omega t) dt. \tag{20}$$

Solving for each frequency component $(\frac{1}{\sqrt{2\pi}} V(\omega) \exp(-i\omega t) d\omega)$ of $V(t)$ at a time, the partial differential equations (17)-(18) reduce to ordinary differential equations:

$$u + \frac{v_a^2}{\omega^2} \frac{\partial^2 u}{\partial z^2} = 0 \tag{21}$$

$$S + \frac{v_a^2}{\omega^2} \frac{\partial^2 S}{\partial z^2} = 0, \tag{22}$$

with the simple solutions:

$$u = u_A \exp(-ikz - i\omega t) + u_B \exp(ikz - i\omega t) \tag{23}$$
$$S = S_A \exp(-ikz - i\omega t) + S_B \exp(ikz - i\omega t). \tag{24}$$

Here, the wave number $k = \frac{\omega}{v_a}$ has been introduced, and u_A, u_B (S_A, S_B) are specified by the boundary conditions. It follows from Eqs.(23)-(24) that the plane waves associated with u_A, S_A propagate backwards (in the $-z$ direction) whereas u_B, S_B propagate forwards (in the $+z$ direction). It is convenient to write down similar expressions for the stress and velocity functions in terms of one set of coefficients only, say S_A, S_B. According to Eqs. (8), (13), and (23)-(24), the sought expressions become

$$T = c^D \left[S_A \exp(-ikz - i\omega t) + S_B \exp(ikz - i\omega t) \right] - hD \tag{25}$$

$$u = \frac{c^D S_A}{Z_a} \exp(-ikz - i\omega t) - \frac{c^D S_B}{Z_a} \exp(ikz - i\omega t), \tag{26}$$

where $Z_a = \rho v_a$ (note that for plane waves: $Z_a = \rho v_a = |\frac{T}{u}|$). Furthermore, under monofrequency conditions, Eq.(16) simplifies to:

$$-i\omega V = -AZ_{e1}\omega^2 D - i\omega \frac{l_1}{\epsilon^S} D - h\left[u(z_1) - u(z_L)\right]. \tag{27}$$

Parameter	Value	Unit
$\omega_0/(2\pi)$ (driving frequency)	$1 \cdot 10^6$	Hz
N (number of periods)	8	
V_0 (applied voltage amplitude)	10.0	V
Thickness (piezoceramic material)	1.96	mm
Transducer area	380	mm^2
Thickness (stainless steel)	2.81	mm
h (piezoceramic material)	$1.42 \cdot 10^9$	F^{2}V/m^3
ϵ^S (piezoceramic material)	$1440\epsilon_0$	F/m
c^D (piezoceramic material)	$1.19 \cdot 10^{11}$	Pa
c^D (stainless steel)	$2.53 \cdot 10^{11}$	Pa
c^D (water)	$2.25 \cdot 10^9$	Pa
c^D (air)	$1.24 \cdot 10^5$	Pa
ρ (piezoceramic material)	7750	kg/m^3
ρ (stainless steel)	8000	kg/m^3
ρ (water)	1000	kg/m^3
ρ (air)	1.29	kg/m^3

Table 1: Table 1: Material parameters and characteristic dimensions.

Employing the two equations (25)-(26) and imposing continuity of the (normal) velocity and pressure between layers/surrounding media supplemented by the condition given in Eq.(27) yield nine equations in nine unknowns for the multilayer transmitter structure depicted in Fig.1. The unknowns are: $D, T_L, T_R, S_{A_i}, S_{B_i}, i = 1, 2, 3$ where T_L and T_R refer to the stress amplitude associated with the backward-propagating wave L (in air) and the forward-propagating stress wave R (in water), respectively. The explicit form of the nine equations read:

$$T_L = c_1^D (S_{A_1} + S_{B_1}) - h_1 D$$

$$\frac{T_L}{Z_{aL}} = c_1^D \left(\frac{S_{A_1}}{Z_{a1}} - \frac{S_{B_1}}{Z_{a1}} \right)$$

$$c_2^D (S_{A_2} + S_{B_2}) = c_1^D \left(S_{A_1} \exp(-ik_1 l_1) + S_{B_1} \exp(ik_1 l_1) \right)$$
$$- h_1 D$$

$$c_2^D \left(\frac{S_{A_2}}{Z_{a2}} - \frac{S_{B_2}}{Z_{a2}} \right) = c_1^D \left(\frac{S_{A_1} \exp(-ik_1 l_1)}{Z_{a1}} - \frac{S_{B_1} \exp(ik_1 l_1)}{Z_{a1}} \right)$$

$$c_3^D (S_{A_3} + S_{B_3}) = c_2^D \left(S_{A_2} \exp(-ik_2 l_2) + S_{B_2} \exp(ik_2 l_2) \right)$$

$$c_3^D \left(\frac{S_{A_3}}{Z_{a3}} - \frac{S_{B_3}}{Z_{a3}} \right) = c_2^D \left(\frac{S_{A_2} \exp(-ik_2 l_2)}{Z_{a2}} - \frac{S_{B_2} \exp(ik_2 l_2)}{Z_{a2}} \right)$$

$$T_R = c_3^D \left(S_{A_3} \exp(-ik_3 l_3) + S_{B_3} \exp(ik_3 l_3) \right)$$

$$-\frac{T_R}{Z_{aR}} = c_3^D \left(\frac{S_{A_3} \exp(-ik_3 l_3)}{Z_{a3}} - \frac{S_{B_3} \exp(ik_3 l_3)}{Z_{a3}} \right)$$

$$-i\omega V = -A Z_{e1} \omega^2 D - i\omega \frac{l_1}{\epsilon_1^S} D - h_1 \left[c_2^D \left(\frac{S_{A_2}}{Z_{a2}} - \frac{S_{B_2}}{Z_{a2}} \right) - c_1^D \left(\frac{S_{A_1}}{Z_{a1}} - \frac{S_{B_1}}{Z_{a1}} \right) \right], \quad (28)$$

where c_m^D, Z_{am}, k_m, h_m, ϵ_m^S are the bulk modulus under constant electric displacement, acoustic impedance, wave vector, piezoelectric h constant, permittivity under constant strain of layer m, respectively, and Z_{aR} (Z_{aL}) is the acoustic impedance of the medium located right (left) to the transducer. Keep in mind that layer 1, layer 2, and layer 3 in the case of the transmitter are the piezoceramic layer, the acoustic coupling layer, and the matching layer, respectively, so that, e.g., l_1, l_2, and l_3 are equal to l_{pz}, l_{ac}, and l_{ma}, respectively.

Solving Eqs.(28) for T_R, the right aperture velocity amplitude u_R can be expressed as:

$$u_R = -\frac{T_R}{Z_{aR}}, \quad (29)$$

and insertion into the Rayleigh equation gives the incoming pressure wave at the receiving transducer [6],[7]:

$$P_{rec}(\vec{x'}, \omega, t) = -\frac{i\omega\rho}{2\pi} \int_{A_{tra}} dA_{tra} \frac{u_R(t - |\vec{x'} - \vec{x}|/v_{aR})}{|\vec{x'} - \vec{x}|}, \quad (30)$$

assuming ultrasound transmission between the two transducers occurs in a water bath and under zero-flow conditions. In Eq.(30), A_{tra}, v_{aR}, $\vec{x}$, and $\vec{x'}$ are the transmitter aperture area, sound speed in the medium to the right (water), the position coordinate on the transmitter aperture (variable during integration), and the position coordinate on the receiver aperture. Notice, that the *axial* distance between the two transducers, i.e., the z-coordinate of $\vec{x'} - \vec{x}$, is a constant during integration due to the assumption that the two transducers point face-to-face. Since this is a one-dimensional model, the incoming pressure on the receiver aperture (being an input parameter to the receiver) is calculated as an average pressure over the receiver aperture:

$$P_{rec}(\omega, t) = \frac{1}{A_{rec}} \int_{A_{rec}} P_{rec}(\vec{x'}, \omega, t) dA_{rec}, \quad (31)$$

where A_{rec} denotes the receiver aperture area. Following this procedure for determining incoming receiver pressures allows receiver voltage signals to be calculated whether the receiver is located in the near-field or in the far-field zones of the transmitter. In a previous paper, however, the receiver was assumed to be located in the far-field zone of the transmitter [5].

In the case where transmission takes place in, e.g., a flow meter in a moving medium, the analysis leading to the received pressure wave becomes much more involved. When comparing stresses instead of pressures, the input signal to the receiver is:

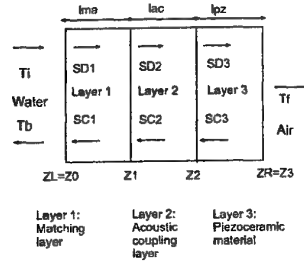$$T_i = T_{rec}(\omega, t) = -P_{rec}(\omega, t). \tag{32}$$

Figure 2: Schematic transducer geometry, receiver.

The analogue set of boundary expressions for the receiver, with Fig.2 as a reference, can now be formulated as:

$$T_i + T_b = c_1^D(S_{C_1} + S_{D_1})$$

$$-\frac{T_i}{Z_{aL}} + \frac{T_b}{Z_{aL}} = c_1^D\left(\frac{S_{C_1}}{Z_{a1}} - \frac{S_{D_1}}{Z_{a1}}\right)$$

$$c_2^D(S_{C_2} + S_{D_2}) = c_1^D\left(S_{C_1}\exp(-ik_1l_1) + S_{D_1}\exp(ik_1l_1)\right)$$

$$c_2^D\left(\frac{S_{C_2}}{Z_{a2}} - \frac{S_{D_2}}{Z_{a2}}\right) = c_1^D\left(\frac{S_{C_1}\exp(-ik_1l_1)}{Z_{a1}} - \frac{S_{D_1}\exp(ik_1l_1)}{Z_{a1}}\right)$$

$$c_3^D(S_{C_3} + S_{D_3}) - h_3D = c_2^D\left(S_{C_2}\exp(-ik_2l_2) + S_{D_2}\exp(ik_2l_2)\right)$$

$$c_3^D\left(\frac{S_{C_3}}{Z_{a3}} - \frac{S_{D_3}}{Z_{a3}}\right) = c_2^D\left(\frac{S_{C_2}\exp(-ik_2l_2)}{Z_{a2}} - \frac{S_{D_2}\exp(ik_2l_2)}{Z_{a2}}\right)$$

$$T_f = c_3^D\left(S_{C_3}\exp(-ik_3l_3) + S_{D_3}\exp(ik_3l_3)\right) - h_3D$$

$$-\frac{T_f}{Z_{aR}} = c_3^D\left(\frac{S_{C_3}\exp(-ik_3l_3)}{Z_{a3}} - \frac{S_{D_3}\exp(ik_3l_3)}{Z_{a3}}\right)$$

$$0 = -AZ_{e2}\omega^2 D - i\omega\frac{l_3}{\epsilon_3^S}D - h_3\left[-\frac{T_f}{Z_{aR}} - c_1^D\left(\frac{S_{C_3}}{Z_{a3}} - \frac{S_{D_3}}{Z_{a3}}\right)\right], \tag{33}$$

where T_b and T_f are the reflected stress amplitude at the left aperture and the forward propagating stress amplitude at the right aperture, respectively, and Z_{e2} represents the series electrical impedance in the receiver circuit. Note that in the case of the receiver, layer 1, layer 2, and layer 3 are the matching layer, the acoustic coupling layer, and the piezoceramic layer, respectively so that l_1, l_2, and l_3 are equal to l_{ma}, l_{ac}, and l_{pz}, respectively, etc. The time-dependent analogue to the last of Eqs.(33) is:

$$0 = AZ_{e2}\frac{\partial^2 D}{\partial t^2} + \frac{l_3}{\epsilon_3^S}\frac{\partial D}{\partial t} - h\left[u(z_R) - u(z_2)\right]. \tag{34}$$

Solving Eqs.(33) for the electric displacement D, the induced voltage $V'_{rec}(\omega, t)d\omega$ may be found:

$$V'_{rec}(\omega, t)d\omega = Z_2I = -iZ_2A\omega D, \tag{35}$$

and summing up contributions from all frequency components associated with the applied voltage pulse gives the real-time induced voltage $V_{rec}(t)$:

$$V_{rec}(t) = \int_{-\infty}^{\infty} V'_{rec}(\omega, t)d\omega = \frac{1}{\sqrt{2\pi}}\int_{-\infty}^{\infty} V_{rec}(\omega, t)\exp(-i\omega t)d\omega, \tag{36}$$

where $V_{rec}(\omega, t)$ in the latter equality is the Fourier transform analogue to $V_{rec}(t)$ (compare $V(\omega)$ with $V(t)$ in Eqs. (19)-(20)). This concludes the derivation of the received voltage response from a known applied voltage signal.
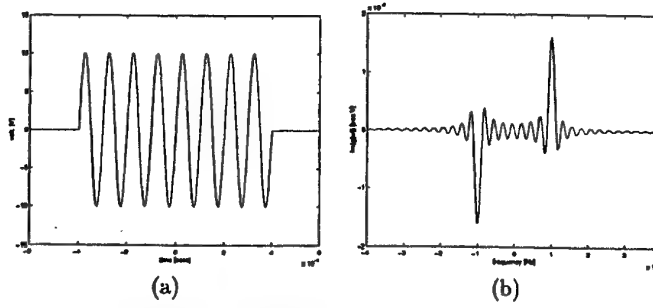
(a)   (b)

Figure 3: Pulse generator voltage (transmitter circuit); b) Fourier transform of pulse generator voltage, ($N = 8$, $V_0 = 10$ V, $\omega_0/(2\pi) = 1$ MHz).

3 Transmitter excitation

Consider the case where a sinusoidal 8-period voltage pulse $V(t)$ with amplitude $V_0 = 10$ V and frequency $\omega_0/(2\pi) = 1$ MHz is applied to the piezoceramic electrodes equivalent to:

$$V(t) = V_0 \sin \omega_0 t, \quad \text{if} \quad |t| \leq \frac{8\pi}{\omega_0}$$

$$V(t) = 0, \quad \text{if} \quad |t| > \frac{8\pi}{\omega_0}. \tag{37}$$

Deconvoluting $V(t)$ into its Fourier components $V(\omega)$ according to Eq. (20) yields:

$$V(\omega) = i\sqrt{\frac{2}{\pi}}V_0 \left[\frac{\sin[(\omega_0 - \omega)(8\pi/\omega_0)]}{2(\omega_0 - \omega)} - \right.$$
$$\left. \frac{\sin[(\omega_0 + \omega)(8\pi/\omega_0)]}{2(\omega_0 + \omega)} \right]. \tag{38}$$

The applied real-time voltage is shown in Fig. 3a and the corresponding Fourier transform is depicted in Fig. 3b. The resonance is, of course, located at the driving frequency: 1 MHz (or −1 MHz) and falls off in an oscillating manner away from the resonance.

The design of the reciprocal transducer is schematically illustrated in Figs. 1-2, and the various material parameters and layer thicknesses are given in Table 1. Note that the thicknesses of the piezoceramic material and stainless steel are chosen to be exactly a half wavelength at 1 MHz in the present work, i.e., $l_i = \frac{1}{2}\sqrt{c_i^D/\rho_i}/(\omega_0/2\pi); i = 1, 3$. These values are slightly different from those used in [8].

(a)   (b)
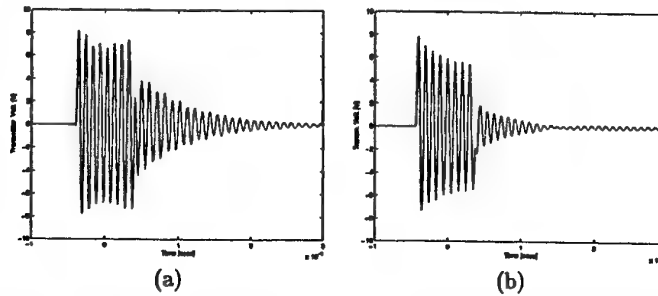
Figure 4: Voltage across the transmitter electrodes for the multilayer structure shown in Fig. (1) where the acoustic coupling layer thickness is zero. a) Calculated voltage response b) Measured voltage response under similar conditions. $Z_1 = 75$ Ohm, $Z_2 = 75$ Ohm.

Measurements were carried out using a LeCroy 9400 DUAL digital oscilloscope to aquire voltage signals across the receiver electrodes. The transmitter was electrically excited using a Philips PM

56

138 function generator adjusted to deliver a sinusoidal 8-period voltage pulse with amplitude 10 V. Since the function generator is represented by a 50 Ω intrinsic impedance, a 25 Ω resistor was connected in series with it to obtain a total source impedance of 75 Ω. In the same manner, by connecting a 25 Ω resistor in series with the oscilloscope's 50 Ω input, a receiver load resistance of 75 Ω was obtained. The two transducers were mounted in a water bath of dimensions: 1 m × 0.5 m × 0.5 m so as to ensure that unintended reflections did not disturb the measurements. Measurements as well as numerical results were obtained corresponding to an axial transducer distance of 19 cm which is a typical transducer distance for flow meter applications in the flow range: 6 - 40 m^3/hour.

The dynamic voltage response across the transmitter electrodes due to the applied generator voltage in Fig. 3a is given in Fig. 4a (computed) and Fig. 4b (measured). Most of the features seen in the measured response are also found in the computed transmitter voltage. In particular: a) the absolute voltage values are similar; b) the first period in the response is characterized by a higher amplitude as compared to the subsequent 7 (i.e., $N-1$) periods; and c) as soon as the generator is off, the transducer continues to perform damped oscillations. The amplitude of the damped oscillations is, however, somewhat higher in the calculated response. This is due to mainly the absence of mechanical and dielectric losses. Another reason is that the transducer is a three-dimensional body where several modes are excited (even though the thickness mode is by far the most important mode!) and stress and strain cannot exactly be represented by one coordinate only (z) corresponding to the quasi-plane wave assumption.

(a)   (b)

(c)
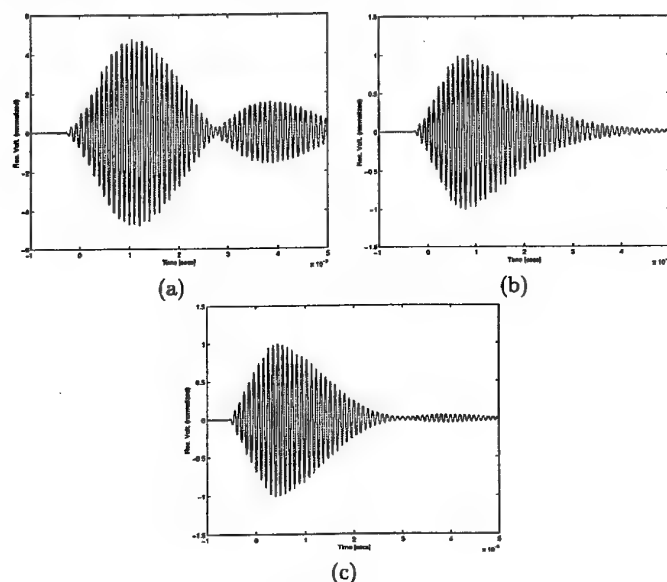
Figure 5: Received voltage for the multilayer structure shown in Fig. (2) where the acoustic coupling layer thickness is chosen to be zero. a) In the case where the transmitter is 'short-circuited' and the receiver is open-circuited ($Z_1 = 0, Z_2 = \infty$); b) Loaded by 75 Ohm resistances in the transmitter and receiver circuits ($Z_1 = 75$ Ohm, $Z_2 = 75$ Ohm); c) Measured received voltage corresponding to conditions under b).

Computing the received voltage for the multilayer transducer structure shown in Fig. 2 in the case where no series resistance appears in the transmitter circuit ($Z_1 = 0$) and at the same time open-circuiting the receiver transducer ($Z_2 = \infty$), i.e., in the limit of vanishing electric displacement between the receiver electrodes, results in the received voltage pulse depicted in Fig. 5a. Since no experimental conditions resemble this ideal situation, it is more appropriate to include a series resistance (which is chosen to be a 75 Ohm resistance in both circuits; a typical value for the electronics in flow meter applications) when comparing theory and measurements. In doing this, the pulse shown in Fig. 5b is computed. It is evident that instead of two consecutive peaks (Fig. 5a), one peak in the pulse is now observed (Fig. 5b), and this latter result agrees much better with

experimental results (Fig. 5c). It should also be mentioned that the computed pulse amplitude is considerably less when including the 75 Ohm resistances (a factor of 4.77 is found between the two amplitudes). In order to have a common standard of reference, all subsequent results are normalized with respect to the peak value of Fig. 5b. In Fig. 5c, measured results for the received voltage response is given corresponding to the same conditions as those in Fig. 5b. The general characteristics are the same: a) the peak value is obtained after approximately 10 periods, i.e., shortly after the generator is in off-mode; and b) following the main peak of the pulse, the signal dies away characterized by a time constant of about 15 microsecs (although the pulse shows somewhat stronger damping in the measured case). This reflects the tendency observed for the voltage across the transmitter electrodes (Figs. 4a and 4b).

4 Conclusions

A complete set of modeling equations for one-dimensional multilayer ultrasound transducers is presented. The combination of Newton's Second Law, Poisson's equation, and the definition of strain, allows dynamic equations for a multilayer transducer to be determined. Transducer dynamics become completely specified by imposing continuity of normal velocities and stress across material interfaces as well as the electrical condition across the piezoceramic electrodes. Numerical test cases are discussed for a transducer consisting of a piezoceramic layer and a half-wavelength matching layer of stainless steel. Variations in transducer reciprocal signals, accomodated by different electrical impedances connected to the transmitter and receiver, are finally addressed, and good agreement between numerical results and measurements is found.

References

[1] J.Tichy and G. Gautschi, 'Piezo-elektrische Messtechnik,' Springer-Verlag, Berlin, Heidelberg, New York, 1980.

[2] L.D. Landau and E.M. Lifshitz, 'Fluid Mechanics,' Course of Theoretical Physics, Volume 6, 2nd Edition, Pergamon Press, 1987.

[3] J. van Randeraat and R.E. Setterington, 'Piezoelectric Ceramics,'Philips Application Book, Mullard Limited, London, 1974.

[4] G.S. Kino, 'Acoustic Waves, Devices, Imaging & Analog Signal Processing', Prentice-Hall, Englewood Cliffs, N.J., 1987.

[5] M. Willatzen, 'Ultrasound transducer modeling - received voltage signals and the use of half-wavelength window layers with acoustic coupling layers,' IEEE Trans. Ferroelectricity and Frequency Control, Vol. 46, pp. 1164–1174, September 1999.

[6] V.A. Shutilov, 'Fundamental Physics of Ultrasound,' Gordon and Breach Science Publishers, 1988.

[7] A.D. Pierce, 'Acoustics, An Introduction to Physical Principles and Applications,' Acoustical Society of America, New York, 1989.

[8] M. Willatzen and E. Brun, 'Modeling of multilayer ultrasound transducers', Proceedings of FLOMEKO 98, Lund, Sweden, June 1998.

Acoustic transmission and reflection properties
of Alberich anechoic coatings

Alex Cederholm

The Marcus Wallenberg Laboratory, KTH

Stockholm, Sweden

1   Introduction

Knowledge of acoustic transmission and reflection properties of construction materials has a great importance for the silent motion of vehicles. The purpose of this study was to experimentally and numerically investigate an Alberich anechoic rubber coating included in submarine hulls. Taking favorable acoustic properties into account the coating can be manufactured thinner than ordinary coatings. A crucial parameter in any vehicle application is weight, thus by using the thinner anechoic coating the weight can be reduced.

The measurements were conducted in water with narrow band spherical insonification of a steel plate, coated with the anechoic rubber. Using the registered data, reflection and transmission coefficients were calculated based on integrated direct, reflected and transmitted wave packages. The considered center frequencies were contained in the kHz region and the used experimental setup enabled to vary the angle of incidence. Thus the obtained reflection and transmission coefficients could be expressed as function of center frequency and angle of incidence.

A computational model based on a finite element approach was adopted to find equivalent elastic parameters of the inhomogeneous rubber coating in terms of homogeneous layers by matching to the measured data, [1]. In the model the plate consists of multiple homogeneous layers surrounded by water halfspaces. For the matching a genetic algorithm was employed to find a suitable layer-parameter combination, [2].

2   Measurements

For the measurements the steel plate was vertically lowered into water. The plate has the dimensions 2 by 2 m and a thickness of 5 mm. In addition the plate is coated with a 5 mm thick Alberich anechoic rubber. The rubber contains periodically placed cylindrical air inclusions with a diameter of approximately 10 mm, resulting in the anechoic characterization. For reference purposes a uncoated steel plate was used for verification of the method and the equipment. As transmitters and receivers, hydrophones of spherical type was employed resulting in a spherically insonification of the plate. The wave package/source signal was chosen to consist of six periods of a cosine function with Blackman window for a specified center frequency. The center frequency ranged from 10 kHz to 30 kHz with a step of 5 kHz. An example of the signal is displayed in Figure 1.
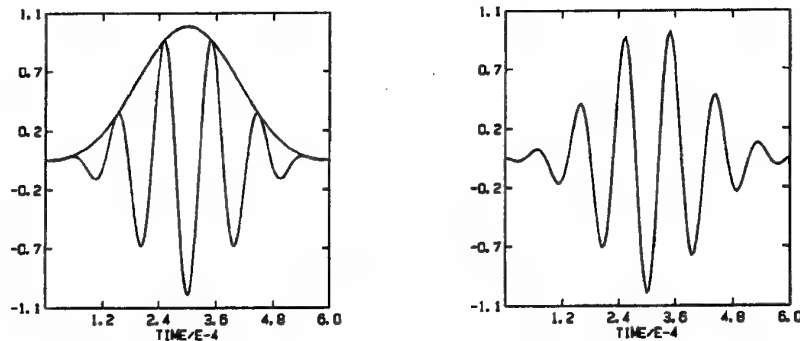
Figure 1. Left: Transmitted signal with the Blackman window.
Right: Measured transmitted signal with filtering. Center frequency 10 kHz.

Furthermore in Figure 1 the corresponding measured signal is displayed, which exhibits a slight difference in comparison to the signal specified in the signal generator. This small perturbation occurs in the signal transition between hydrophone and water, which should be expected. The measured signal has been filtered and then used as input for the numerical computation.

Referring to Figure 2 the experimental setup is shown with scaled distances. The hydrophone where the wave package is transmitted is denoted as A. With hyrophones placed at reflection position, B, and at transmission position, C, resulting in a angle of incidence α, time signals have been registered. Using the direct wave, the transmitted wave and the reflected wave the corresponding reflection and transmission curves as function of center frequency and angle of incidence are calculated. The angle of incidence, α, ranged between 8.13° to 40.99° degrees and was varied by increasing/decreasing the depth of hydrophone A and respectively decreasing/increasing the depth of hydrophones B and C.

Figure 2. Experimental setup showing orientations of the hydrophones (A,B,C) in respect to the investigated plate.

The configuration of the plate and the hydrophones has been chosen with care, to avoid unwanted interference from later arriving field components in the registered time signals. Such components are for instance reflections from the water surface and the plate edges.

3   Computational model

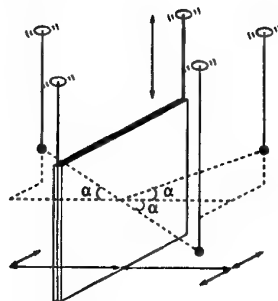In the computational model the plate is composed of two coupled homogeneous elastic layers surrounded on both sides by water halfspaces. A cartesian coordinate system (r,z) is introduced with the z-axis orthogonal to the plate. The transmitter is represented by a symmetric point source on the z-axis, exciting a cylindrically symmetric wavefield composed of compressional waves (P) and waves with polarization parallel to the z-axis (SV). The equations of motion are transformed to the lateral wavenumber domain (k) by a Hankel-Bessel transform.

$$H_m(h(k)) = \int_0^\infty h(r) J_m(kr) r \, dr \quad m = 0, 1, \dots$$

Here $J_m(kr)$ are Bessel functions of the first kind and k is the wave number in the r direction. In the k domain the displacements and pressures are solutions of a two point ordinary differential equation boundary-value problem. This boundary-value problem is solved by a finite element approach using basis functions composed of exact local solutions in the layers. The finite element analysis results in a system of linear equations.

$$\mathbf{A}(k)\mathbf{x} = \mathbf{b}(k)$$

The equation system is symmetric and block-tridiagonal with blocks of order 1 x 1 in fluid layers and 2 x 2 in solid layers. The corresponding wavefield components in the (r,z) domain are then obtained by inverse Hankel-Bessel transformation.

$$\frac{1}{2} \int_\Gamma \mathbf{H}(kr)\mathbf{x}(k) k \, dk$$

The contour Γ is deviated from the real axis to an equivalent path and the integral is evaluated by adaptive numerical quadrature. Transient fields are obtained by Fourier synthesis of their mono-frequency components.

A comparison in the time domain between the predicted and the experimentally observed pulse shape in reflection and transmission position is shown in Figure 3 for the uncoated steel plate. The parameters of steel and the water halfspaces are assumed to be known, and are shown in Table 1. In Figure 3 data is normalized by the direct pulse arrival at the reflection position. The angle of incidence is 24.3° and the center frequency is 20 kHz.
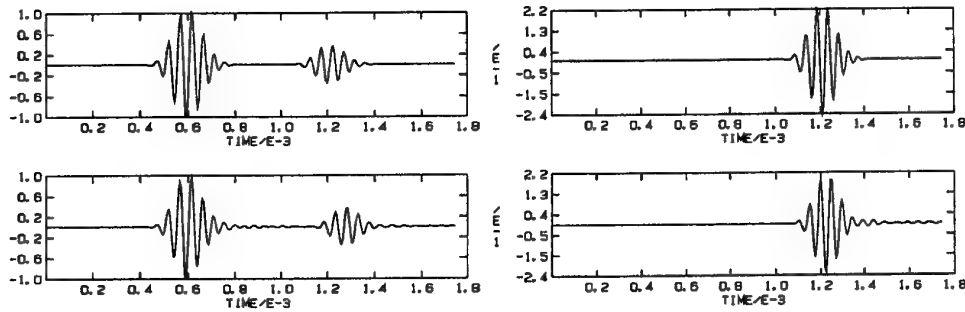

Figure 3. Upper-Left: Reflection position, simulation. Upper-Right: Transmission position, simulation. Lower-Left: Reflection position, measurement. Lower-Right: Transmission position, measurement.

Note that both curve shapes and amplitudes agree for the uncoated steel plate and there is no harmful interference from unwanted field components.

4 Transmission and reflection coefficients

In Figure 4 the reflection and transmission coefficients for the uncoated steel plate, with parameters in Table 1, are shown as function of incidence angle at a center frequency of 20 kHz.

Figure 4. Left: Reflection coefficient. Right: Transmission coefficient.

The average deviations for the reflection and transmission coefficients are ±0.21 dB respectively ±0.42 dB, which is satisfactory.

Turning to the coated steel plate the elastic parameters of the homogeneous rubber layer should be matched to the measured data. For the matching a genetic algorithm is employed. The algorithm finds a suitable parameter combination for the rubber layer in the parameter space within specified boundaries. In this case the parameter space consists of the density, the P wave velocity, the S wave velocity and the thickness for the layer. The parameter sets, individuals, are represented by bit-strings, 'chromosomes', unique for each individual. Initially a finite number of individuals are chosen at random, constituting the first generation. Then, a simulated evolution proceeds by applying mating, reproduction and mutation operators iteratively. Eventually a best fitted individual is produced for a specific number of iteration steps.

For the matching the fitness function has been chosen to be the the sum of the average difference between the measured and the predicted reflection and transmission coefficients, in dB scale. The measured coefficients are based on maximum amplitudes of the the observed wave packages. For the predicted coefficients a simplification has been introduced by using computed mono-frequency fields, thus making the computations less time consuming.

The resulting material parameters are shown in Table 1. Describing the inhomogeneous coating by one homogeneous layer resulted in a thickness of 50.2 mm, consequently an approximately 10 times greater thickness.

Material	Density kg/m^3	P-vel m/s	P-atten db/λ	S-vel m/s	S-atten db/λ
Water	1000.0	1480.0	-	-	-
Steel	7700.0	5850.0	-	3230.0	-
Rubber	544.6	330.2	1.0	84.9	50.0

Table 1. Material parameters of the surrounding medium and the plate.

In figure 5 the corresponding reflection and transmission coefficients for the coated steel plate is displayed at a center frequency of 20 kHz.
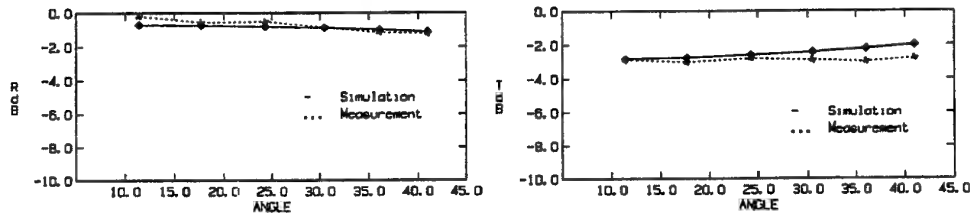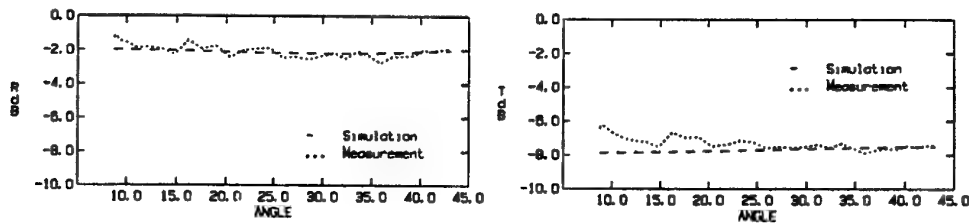

Figure 5. Left: Reflection coefficient. Right: Transmission coefficient.

The average deviations for the reflection and transmission coefficients are ±0.27 dB respectively ±0.48 dB, which at this stage is satisfactory.

5   Conclusions and future work

For the uncoated steel plate good agreement between the observed and the theoretically predicted pulse shapes has been achieved, see Figure 4. For the coated steel plate the agreement is satisfactory, see Figure 5, but the thickness of the homogeneous rubber layer is approximately 10 times greater than the real thickness of the coating. The future objective is to obtain the simplest equivalent material for the coating with the prerequisite to reduce the overall thickness of the composite layer. For this purpose several layers describing the inhomogeneous rubber could be introduced. Matching all frequencies simultaneously will be of particular interest, since the resulting parameter combination could be used as a model of the rubber layer in a broad frequency range.

Acknowledgment

References

[1] I.Karasalo "Exact finite elements for wave propagation in range-independent fluid-solid media",
    Journal of Sound and Vibration, **172**(5), 1994, pp. 671-688.

[2] D.Whitley, T.Starkweather "Genitor II: a distributed genetic algorithm",
    J. Expt. Theor. Artif. Intell. **2**, 1990, pp. 189-214.

4

Mine Classification by Synthetic Aperture Sonar

Geoffrey Shippey, CTH*
Jörgen Pihl, FOI**
Mattias Jönsson, FOI**

*CTH, Chalmers University of Technology, SE-412 96 GOTHENBURG, Sweden
**FOI, Swedish Defence Research Agency, SE-172 90 STOCKHOLM, Sweden

Abstract

High-resolution sonar at long range is desirable for future mine hunting and classification. Synthetic Aperture Radar (SAR) is now used routinely to achieve high resolution at long distances, so it is natural to look to Synthetic Aperture Sonar (SAS) for a solution to the problem. Unfortunately the operational application of SAS has been very limited. The low velocity of sound compared with radar signals creates a practical problem. Variability of the propagating medium and uncertainty in position of the sonar platform create problems in achieving the necessary phase coherence for aperture synthesis. SAS image resolution depends on how well these effects can be compensated. In SAR, correction of platform position from the radar data itself is termed "autofocus". The term "autopositioning" is preferred for SAS, since image focus is seldom used directly. The paper describes an experiment using the Remotely Operated Vehicle (ROV), PLUMS, and a wideband sonar with a multiaperture receiver array. Artificial targets were placed on the seabed about 100 m from the ROV track. A beacon positioning system with two transmitters on the seabed was used for initial positioning. The availability of a physical aperture image from each transmitted pulse greatly simplified the autopositioning problem. DPC (Displaced Phase Centre) methods were investigated, based on both seabed and target image correlation. The simplest method investigated was a variant of Prominent Point Processing as used in SAR. The paper provides some theoretical background to these different methods, together with corrected images of the experimental targets.

1 Introduction

The development of new mines, which can move and hit ships at some distances, has made mine hunting more risky for the Mine Counter Measure (MCM) ships. The capability to detect and classify mines at a distance is therefore highly desirable, especially in non-war situations where personnel losses cannot be tolerated. There are at least two ways to achieve this capability. One is to mount the sonar on a Remotely Operated Vehicle (ROV), which can then be moved close to the mine without endangering the MCM ship. Another way is to improve the spatial resolution of the sonar, so that classification can be done at a safe distance. Higher resolution requires a bigger sonar aperture, but there are practical and economical limits for the physical size of an MCM sonar, and current designs are coming close to this. There is therefore considerable interest in the use of Synthetic Aperture Sonar (SAS) to increase the effective aperture size for classification purposes. Range resolution is also important for SAS imaging, partly for the final image quality, and partly for autopositioning along the way. We have therefore investigated the use of SAS for classification of MLOs (mine-like objects) at 100m range, in an experiment using an ROV-mounted wideband so-

nar. The wideband SAS processing method consists of combining successive physical aperture images as described in [1]. This is a conceptually simple time-domain method for wideband signals, avoiding the bandwidth and other limitations of many FFT-based processing techniques. The problem of slow processing in the time domain will be discussed later in the paper.

2 The Field Experiment

The experiment was performed at the FOI test site Djupviken in October 1999. Djupviken is a semi-enclosed bay in the southern Stockholm Archipelago, where the seabed consists of soft postglacial clay and mud. At this site, there is a pontoon laboratory, which is completely floating in 10 m of water. The seafloor slopes downwards, from a depth of 10m where the ROV was operated, to 20m depth at 200m range out in the bay. The seabed is fairly smooth and free from vegetation. Two transmitters, "beacons", were placed on the seabed and used to determine the position of the platform by triangulation. The beacons were placed 80m from the ROV track, about 40m apart (Figure 1).
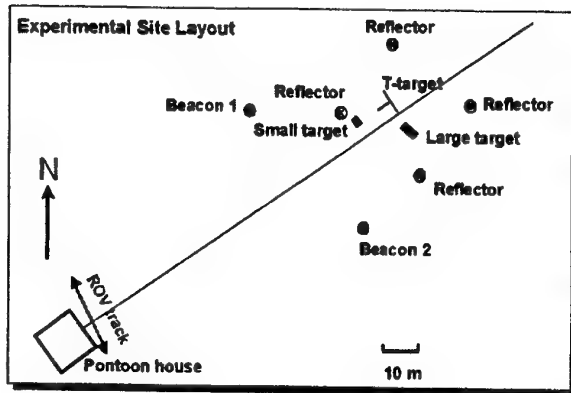
Figure 1. The objects at the experimental site.

Three targets were positioned about 100m from the ROV track, and the target area was delimited by four corner reflectors. The targets were two MLOs, the "Small Target" with dimensions 0.4x0.4x1.6m and the "Large Target" (0.7x0.7x1.8m), together with the "T-Target", designed to assess spatial resolution in the SAS image. This consisted of a T-formed metal frame with plastic foam balls attached on short rods above it (Figure 2). During processing another target was discovered at closer range, which turned out to be a concrete slab sunk in the seabed.

The sonar was mounted on the PLUMS (Platform for Underwater Measurement Systems) ROV, (Figure 3), designed by the Swedish Defence Research Agency. PLUMS is an open stainless steel pipe frame within which different types of equipment can be mounted. Heading and attitude are measured using a three-axis rate gyro aided by a magnetic compass and two pendulums. Roll, pitch and yaw angles can be controlled to errors of less than one degree. Depth can be kept constant to within 0.1 m down to the maximum depth of 70 m.
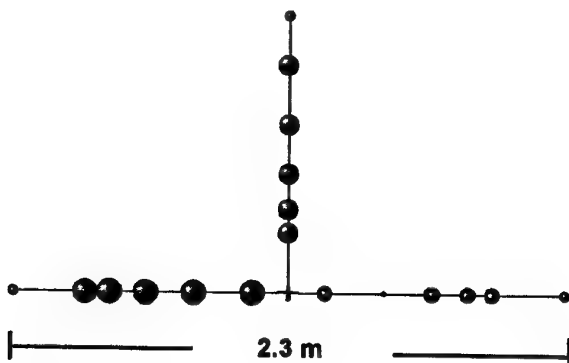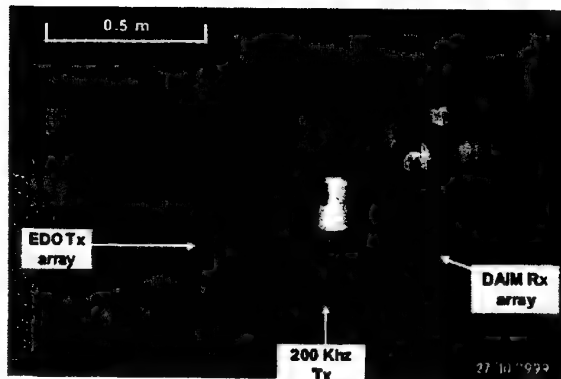

Figure 2. T-target.

Figure 3. The ROV PLUMS.

Two different transmitters were used for imaging, an EDO side-scan array and a 200 kHz single transducer transmitter, here termed Tx200. The receiver array consisted of two identical 16-element sub-arrays with a spacing of 15mm. For the Djupviken experiments, they were mounted side by side to form a 32-element Uniform Linear Array (ULA). The DAIM Receiver has an operational bandwidth from 50 kHz to 100 kHz, which is extremely high. It is difficult and costly to achieve uniform receiver response over a large sector in azimuth and a wide bandwidth. However in the analysis, the received signals are always first matched filtered with a computed kernel. The kernel is based on a recorded replica of the source signature and its Hilbert transform and can be adjusted to give equal response for all receiver channels [2]. Software calibration reduces the need for uniform response from the receiver hardware.

In our experiments, the beacons and the EDO array used a linear chirp from 60kHz to 120kHz, while the Tx200 chirped from 120kHz to 240kHz. Unfortunately the receiver response was not constant within this frequency span, resulting in a usable bandwidth of only about twenty percent of the nominal bandwidth. Match filtering also decreases the effective bandwidth, since the spectrum is in some sense squared.

3 Beacon Positioning
3.1 Introduction

In SAS, image resolution depends on positioning accuracy. Along-track errors of the order of the acoustic wavelength and even smaller across-track errors lead to evident phase incoherence, giving blurred focus and high

64

sidelobe levels. Initial positioning estimates can be obtained by dead reckoning with a high-quality platform. However the PLUMS vehicle was not equipped for precision inertial navigation, so beacon positioning was used instead. Two wideband transmitters mounted on the seabed were used as baseline. In previous rail-based experiments using the DAIM receiver array, very accurate range estimates were made using a shore-mounted wideband transmitter, and it was hoped to repeat this experience. Look-angles up to 1 radian are possible with the DAIM receiver, allowing positioning along an extended track. However beacon positioning is an operational inconvenience, and inertial platforms are expensive, so a main objective of the experiment was to investigate autopositioning methods, where the platform position is corrected from the acoustic data itself.

3.2 Position Estimation

The precise separation between the beacons was not known. Hence the positioning computation was performed in three stages. First range and look-angle was estimated for all pings to one beacon. Range and look-angle was then estimated for all pings to the second beacon. The look-angles as seen from the receiver array were estimated using wideband MUSIC [3,4], and enabled beacon separation to be estimated by the cosine law. Vehicle position could then be determined by triangulation using the two ranges and beacon separation. The angular information also allowed vehicle heading to be determined with more precision than was given by the on-board instrumentation.

The matched filtered signal was first windowed to remove any surface or bottom reflections, which also eliminated signals from the second beacon and other sources. The platform moved at a slow steady speed so the window was chosen around the range determined from the previous ping. The MUSIC look-angle allowed beamforming in the beacon direction followed by range estimation. Signal travel times were determined either from the peak amplitude of the compressed signal, or by correlation with a matched filtered replica of the transmitted pulse.

3.2 Navigation

Range and angle estimates are made in the plane containing the receiver and beacon. Triangulation is required in a horizontal plane, so these ranges and angles are first resolved into the horizontal plane. The baseline between the two beacons can then be computed from the cosine law,

$$D^2 = r_1^2 + r_2^2 - 2r_1 r_2 \cos\left(\Theta_1 + \Theta_2\right) \tag{3.1}$$

where r and theta are the horizontal range and look-angles to each beacon (Figure 4). Separation between the beacons is estimated as the mean separation over all pings. Platform position is determined in the beacon coordinate system, with origin midway between the beacons. The x-axis points along the baseline while the y-axis is orthogonal to the baseline pointing towards the vehicle (Figure 5). The platform position is given as

$$x = \frac{r_2^2 - r_1^2}{2D} \tag{3.2}$$

and

$$y = \sqrt{\frac{r_1^2 + r_2^2 - D^2}{2} - x^2} \tag{3.3}$$

Vehicle heading is determined from the bearing and look-angle to both beacons, and then averaged.

In the Djupviken experiment, the beacon baseline was quite short compared with the range to the vehicle, while the vehicle path was almost parallel to the baseline. The ensuing along-track navigation errors were greater than the cross-track errors. Estimates made from the imagery suggest an along-track random position error of 74 mm, and an across-track random error of 18mm. These are not absolute errors but the errors relevant to phase coherence along the aperture.
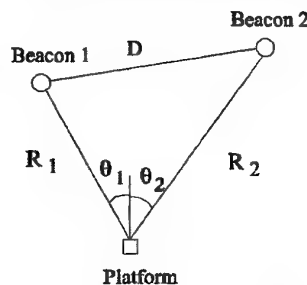

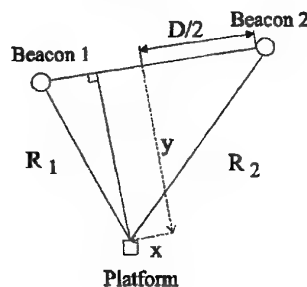Figure 4.The platform and the two beacons projected on a horizontal plane.

Figure 5.The platform, the beacons and the beacon coordinate system.

4 Autopositioning

4.1 Introduction

In the SAR community, and in much of the SAS literature, autopositioning/autofocus is entirely concerned with cross-track navigation error. This is because phase coherence is so much more sensitive to cross-track error. Here the along-track errors were too large to ignore, so methods which could correct for both components of error were investigated. A review of SAR autofocus methods is contained in [5]. Phase gradient methods can detect track curvature, but are less helpful for the random ping-to-ping platform errors which are a feature of SAS. However one method, Prominent Point Processsing can be implemented in a particularly simple way using a multi-channel receiver array. This will be described in Section 4.2. Displaced Phase Centre (DPC) methods appear to have been developed specifically for sonar [6]. Leading and trailing subarrays are selected from the full receiver array in such a way that the phase-centre, defined as the midpoint between transmitter and receiver, remains stationary between consecutive pings. In Sherriff's implementation, seabed echoes from consecutive pings are correlated, and the phase displacement gives cross-track (strictly cross-heading) error. In our method, DPC images of the seabed are correlated instead of DPC echoes. Section 4.3 shows that this method is capable of giving both along- and cross-heading error. A similar method can be used with target images.

SAS processing is usually carried out in the FFT Domain. However when a long, wideband, receiver array is used, and random autopositioning corrections are required, it is more convenient to generate the SAS image by summing physical aperture images derived from successive pings, leading to a time domain back–projection approach. Autopositioning is then also based on physical aperture images generated at each platform position. The disadvantage with this method is slow processing, but faster time-domain algorithms are now becoming available [7].

4.2 Prominent Point Processing

This is conceptually the simplest method. As noted earlier, SAS imaging is carried out by adding physical aperture images, generated at each point along the aperture. If a strong isolated reflector is present in the target, this gives rise to a point-spread function in each image with peak brightness at the pixel corresponding to the reflector location. Phase coherence for this reflector is then forced by phase-shifting each physical aperture image so that the phase at the selected pixel location is zero. This phase shift corrects for both along and across-heading errors resolved along the line of sight to the selected pixel in the target area, and thus for the whole image if the area is sufficiently small. The same pixel location must be used throughout, since the brightest pixel may move from one ping to the next. The strategy used with recorded data was to select the location of the brightest pixel in an image generated from the middle of the synthetic aperture.

Only one isolated strong reflector should be present at the selected location. Otherwise phase interference between neighbouring reflectors causes errors. Also the uncorrected navigation must be sufficiently good to select the same point in the image each time. However the image-based method requires no interaction, and a single phase-shift at mid-frequency could be used to handle the wideband echoes [8].

4.3 Seabed Image Correlation

The idea is to correlate images of the same area of seabed from consecutive pings, generated using DPC subarrays chosen from the full receiver array. If there is no displacement, then the consecutive images will correlate perfectly. However if the phase-centre is displaced by a small amount on the seabed, then complex images of seabed or target are phase-shifted by an angle proportional to platform displacement [9].

For seabed autopositioning, the coordinates of the image frame move with the phase-centres of the subarrays, as given by the navigation data. The image area should lie directly abeam of the displaced phase centres for consecutive pings, designed to be almost coincident in the along-track direction. Consider the following simplified model. The sonar platform travels with constant heading along the x-axis, with the receiver axis pointing in the y-direction. The seabed is defined by a random distribution of reflectors on a plane, horizontal, surface. For simplicity, this is assumed to be coplanar with the vehicle, an assumption not made in actual processing. Define an H x K rectangular image frame on this surface centred at [X,Y]. Suppose that a ping occurs when the phase centre of the array lies at [0,0]. A physical aperture complex image is made of the reflectors visible within the frame, with coordinates [x', y'] centred on the middle of the frame. Suppose Y is sufficiently large for all points in the image to lie in the far field of the array, and that $Y \gg X$, $Y \gg H$, $Y \gg K$. Then all angles α are small enough for $\sin \alpha \approx \alpha$. Consider a

reflector located at x'= a, y'=b within the frame. Then the psf is a circular arc through [a,b], approximating a straight line, making angle α = -atan((X+a)/(Y+b)) with the X-axis, ie

$$\alpha \approx -\frac{X+a}{Y} \qquad (4.1)$$

A second ping is transmitted when the phase-centre has moved to [u,v]. There is no navigation error, so the image frame also moves by [u,v]. The reflector moves to [a-u, b-v] within the frame. The change in α is negligible. The two images are now correlated in the column, or Y, direction. Suppose that one of the columns coincides precisely with x' = a. The psf in the second image, centred on [a-u, b-v] intercepts this column at

$$y'= b - v - u \tan\alpha \approx b - v - \frac{u(X+a)}{Y} \qquad (4.2)$$

Then image correlation for this column will show a displacement given by

$$\Delta y'(a) = -v - \frac{u(X+a)}{Y} \qquad (4.3)$$

If there are many reflectors in the scene, then the displacements for all the columns across the image lie on a straight line given by

$$\Delta y'(x') = -v - \frac{X+x'}{Y}u = -v - \frac{u}{Y}X - \frac{u}{Y}x' \qquad (4.4)$$

The slope of this correlation line

$$\varphi = \frac{u}{Y} \qquad (4.5a)$$

depends on the along-heading displacement, u. Write Q=X/Y≈ (minus look-angle) for X<<Y. The intercept at x'=0 is given by

$$\Delta y'(0) = -v - \Theta u \qquad (4.5b)$$

Equations (4.5) can be inverted to obtain [u,v] , the true movement of the phase-centre from the slope and intercept of the image correlogram. The navigation error [g,h] is the difference between the [u,v] and the displacement given by the navigation file. To obtain the integrated track error, these ping-to-ping errors [g,h] must be summed over the pings along the synthetic aperture. The above analysis was confirmed by simulation studies using random distributions of point reflectors to represent the seabed.

The above arithmetic does not rely on stabilizing the phase centre against platform movement, but DPC is needed to retain cross-correlation between images when the platform moves a substantial distance between pings. In our experiments, the correlation levels between seabed images was poor, so a lot of work went into extracting the line fit required for Equation 4.4. Images are already broken into columns by the frame definition. They were further divided into overlapping sections in the row direction. Each section of each column was then correlated separately with the matching section in the partner image. Correlation of each pair of sections yields four quantities - peak absolute ccf, ratio of peak ccf to next highest peak, estimated Y displacement, cross-power. The correlation is rejected if peak ccf or peak ratio are too low or Y displacement is too high. The result of image correlation is a pair of matrices of Y-displacements and cross-powers, with rejected sections indicated by NaN entries. A Hough Transform, weighted by cross-power, was then be used to find the best line fit.

4.4 Target Image Correlation

A prominent landmark such as a rock outcrop can be used in a similar manner to the seabed, but leaving the image frame fixed as the platform moves. The arithmetic is slightly different but the principle is the same. The prominent object can be the target itself. However the target is too small to be resolved in the physical aperture image (otherwise SAS would not be necessary), so will not appear as a random reflector distribution. Using a point-target model, the psf is a sector of a circular arc centred on the phase-centre at each platform position. A little arithmetic leads to the expected result that the y-intercept in (4.5b) gives a combined correction for navigation error resolved in the direction of the target. This correction was used for the results shown in the paper. Subject to certain conditions, it is also possible to separate out along and across heading error components, but this was not done. The theory was confirmed by simulation studies, including the simulated T-Target showing that the point target model was appropriate in this case.

5 SAS Processing
Prominent Point Processing

In spite of its theoretical limitations, this method worked consistently well with all targets imaged. Examples of PPP compensation are shown in Figure 6 (T-target) and Figure 12 (Large target). Of course any detected target is likely to be a prominent object in the scene, but it is less obvious that the target will contain prominent points, which are satisfactory for the algorithm at the resolution required for classification.

Seabed Autopositioning

Conditions for seabed autopositioning were difficult at Djupviken. Due to the sloping seabed no seabed echoes were received from target range using the 200 kHz transmitter, and no seabed echoes at all using the EDO array, which was unfortunate since the T-Target was only visible with that transmitter. At 200 kHz useful seabed echoes were received out to a range of 35 m from the PLUMS track, but there were severe problems with surface multiples, since the DAIM receiver has a wide elevation beam pattern. There were also problems with periodically corrupted echoes, which made it difficult to find a long enough sequence of pings for SAS imaging.

In the absence of true position, one test of seabed autopositioning is to compare position estimates using images at different ranges. Comparative results at 200 kHz for mid-ranges 21m and 25m are shown in Figure 7. The results for mid-ranges 21m and 28m are shown in Figure 8. The comparison looks quite encouraging apart
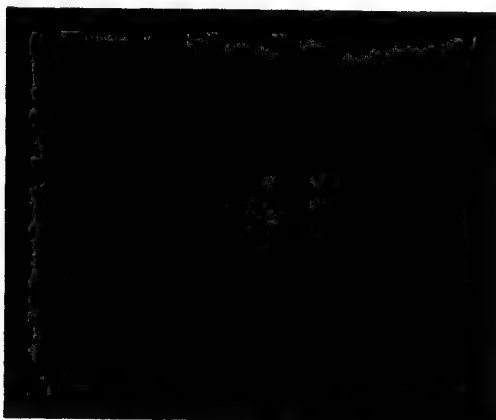
from a few spikes. However when the summed ping-to-ping errors are compared in Figure 9, it can be seen that the corrected tracks jump apart, although they remain parallel for short sequences at a time. This shows the susceptibility of incremental methods to occasional large errors. The result of Seabed Autopositioning is illustrated by Figures 10-11 where the "Large target" is imaged with and without Seabed Autopositioning.

Figure 7. Seabed Autopositioning at 200 kHz. Ping-to-ping cross-track error comparison for mid-ranges 21 m (solid line) and 25 m (dashed line).
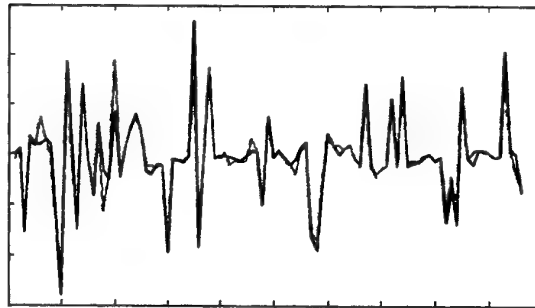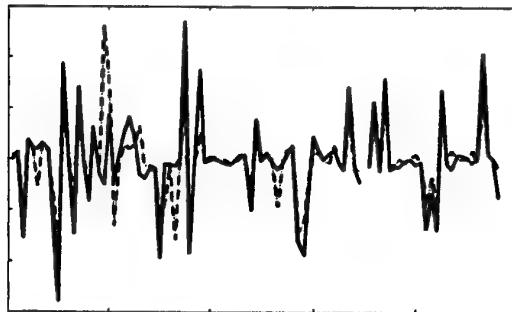

Figure 8. Seabed Autopositioning at 200 kHz. Ping-to-ping cross-track error comparison for mid-ranges 21 m (solid line) and 28 m (dashed line).
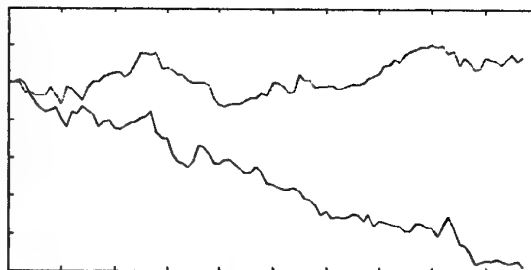

Figure 9. Seabed Autopositioning at 200 kHz. Summed ping-to-ping cross-track error comparison for mid-ranges 21 m (lower line) and 25 m (upper line).

Figure 6. SAS image of T-target with EDO array and PPP compensation.

Figure 10. SAS image of "Large target" with Tx200, Seabed Autopositioning and PPP compensation.
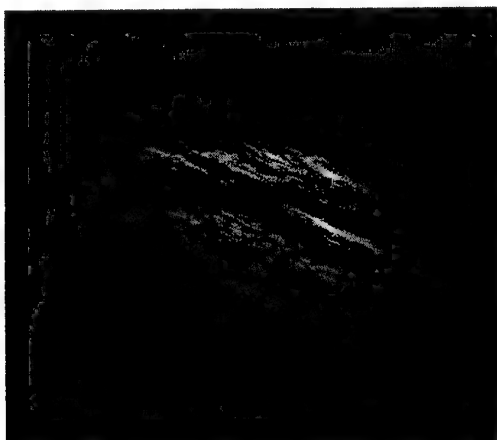

Figure 11. SAS dB image of "Large target" with Tx200 and PPP compensation.

Target Autopositioning

Good image correlations were obtained at both frequencies, using the method outlined in Section 4.3. The result for the T-Target was quite similar to that of the PPP method.

Comparison

Figures 11 and 12 show images of the Large Target using each transmitter. Theoretically the Tx200 should produce better resolution but to achieve the higher resolution positioning must be good enough. Since the positioning accuracy is equivalent in both cases the best image is actually produced with the EDO array.
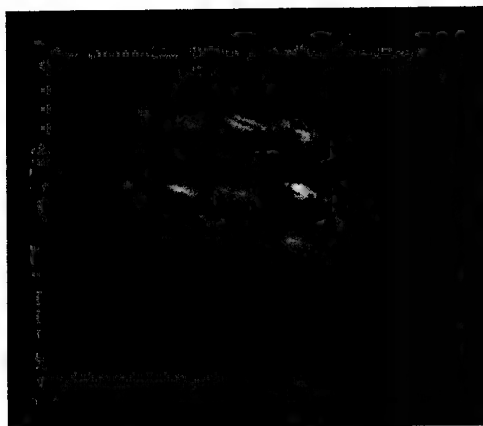
Figure 12. SAS dB image of "Large target" with EDO and PPP compensation.

6 Conclusions

The beacon positioning system using the wideband receiver array worked well, but accuracy was inadequate for synthetic aperture imaging. However after autoposition correction, sufficiently good SAS images for target classification were obtained.

In spite of theoretical limitations, Prominent Point Positioning worked consistently well. This algorithm proved particularly simple to implement using the multi-channel receiver array. An alternative method based on correlating DPC physical aperture images of the target also worked well. This is important, because the DPC method is more general. Autoposition by correlation of DPC seabed images has been shown theoretically and by simulation to yield both along and across-heading errors, but experimental results were disappointing. Further work is needed to decide whether these reflect a fundamental sensitivity of the method to the seabed environment.

For future research, there are a number of practical steps which can be taken to improve the experimental equipment. One goal for this research is to develop robust autopositioning methods, which are adequate for SAS imaging in combination with simple dead-reckoning navigation on the platform.

69

7 Acknowledgements

8 References

[1] G.Shippey (1997): "Simple algorithms for sonar imaging and swath bathymetry with a linear swept frequency (chirp) source", Int. J. of Imaging and Imaging Technology (8, pp.359-376)

[2] Q.Liu, O.Kröling, and G.Shippey (1999): "Software calibration for a wideband linear receiver array using mat5ch-filtering processing", Proc. Inst. Acoustics (UK), **21 Pt1,** (pp103-110)

[3] H.Krim and M.Viberg (1996):"Two decades of signal processing research: the parametric approach"" IEEE Signal Processing Magazine **13(4),** (pp.67-94)

[4] Q.Liu, G.Shippey, and M.Viberg (1999): "Resolution-enhanced active wideband sonar imaging employing beamspace focussing and subspace methods", Proc ISAS 1999 **VI,** Orlando Fl, July 1999, (pp.115-121)

[5] W.Carrera, R.S.Goodman and R.M.Majewski: "Spotlight Synthetic Aperture Radar", Artech House, 1995

[6] R.W.Sheriff: "Synthetic aperture beamforming with automatic phase compensation for high frequency sonars" *Proc. IEEE Symp. On AUV Technology,* Washington DC, June 1992, pp 236-245

[7] L.M.H. Ulander, H. Hellsten, and G Stenström, "Synthetic-aperture radar processing using fast factorised backprojection", Proc. EUSAR 2000, 3rd European Conference on Synthetic Aperture Radar, Munich, Germany, 23-25 May 2000, pp. 753-756.

[8] G.Shippey, P.Ulriksen, and Q.Liu: "Quasi-narrowband processing of wideband sonar echoes", (Proc.4'th European Conf. on Underwater Acoustics) Ed. A.Alippi and G.B.Canelli, Rome, 1998, (pp.63-68)

[9] G.Shippey, P.Ulriksen, and Q.Liu (1998):"Wideband swath bathymetry, SAS autofocus, and underwater navigation fixes: three related problem in echo/image correlation", Proc Inst Acoustics **20 Pt 7 ,** (pp.1-10)

Simulation of nonlinear fields from 2D ultrasound transducers and a new secondary grating lobe phenomenon

Helge Fjellestad and Sverre Holm

Abstract—In this study we have used Burgers' equation to study the field from sparse ultrasound arrays where the full array had 50 by 50 elements. The two-way sidelobe level was reduced by 20-25 dB compard to the fundamental mode. We have also found that a new grating lobe appears at the second harmonics at half the sine of the angle of the fundamental grating lobe.

I. INTRODUCTION

In this study we wanted to simulate the two-way response from sparse arrays when imaging in a nonliner medium. The purpose was to compare the performance under nonlinarity with that in a linear medium as found in [1].

II. THEORY

We have used Burgers' equation [2] to describe the acoustic field:

$$\frac{\partial u}{\partial z} = \frac{\beta \omega_o}{c_o^2} u \frac{\partial u}{\partial \tau} + \Gamma \frac{\partial^2 u}{\partial \tau^2}. \tag{1}$$

In this expression, c_o is the nominal speed of sound in the medium (speed of infinitesimal bulk waves), $\beta = 1 + \frac{B}{2A}$ where $\frac{B}{A}$ is the ratio of the first two terms in the nonlinear pressure - density relation for the medium, and, finally, Γ is a constant related to the thermo-viscous dissipation of the medium. Also, $\tau = \omega t - kz$.

The expression can be modified for numerical implementation [3]:

$$\frac{\partial u_n}{\partial z} = i \frac{\beta \omega_o}{4 c_o^2} \left(\sum_{m=1}^{n-1} m U_m U_{n-m} + \sum_{m=n}^{\infty} n U_m U_{n-m}^* \right). \tag{2}$$

The infinite series has to be truncated to a finite number of harmonics, N. The simulator is based on the principles of [4] and with modifications from [3] in order to generalize it from a circular source geometry to a rectangular geometry. In the simulator, nonlinear propagation is taken care of through the truncated eq. 2 and diffraction is handled from one depth to another through the angular spectrum method [5]. Attenuation can also be introduced in the diffraction step, although not used in our study.

Helge Fjellestad was at the University of Oslo and is currently at PGS Seres, Strandveien 4, P.O.Box 354, N-1326 Lysaker, Norway. Sverre Holm is with the Department of Informatics, University of Oslo, P.O.Box 1080 Blindern, N-0316 Oslo, Norway.

Transducer:	
Beam type	CW
Radius	7.5 mm
Initial pressure	600 kPa
Frequency	3 MHz
Elevation focus	80 mm
Azimuth focus	80 mm
Wavelength	0.5133 mm
Medium:	
Velocity of sound	1540 m/s
Non-lin. parameter (beta)	3.5
Attenuation	0 dB/cm/MHz
Number of harmonics	4
Number of lateral samples	640
Density	1000 kg/m³
Maximum depth	100 mm
Sampling in z	0.39 mm
Sampling in x and y	0.308 mm

TABLE I

SIMULATION PARAMETERS.

III. RESULTS

The main simulations are done for a set of sparse array layouts that were developed during the project "Real-time 3D Ultrasound Imaging System with Advanced Transducer Arrays (NICE)" where the objective was to lay the foundation of a real-time 3D imaging ultrasound system. Part of this project has been done at this University, specifically the construction of the sparse transducer for fundamental imaging. In the NICE project the geometries were evaluated by simulation and experiment for linear wave propagation [1].

When using harmonic imaging, the transmitted frequency has to be lowered because the double frequency has to be within the transducer bandwidth. This has not been done in these simulations because the grating lobes are moved to other locations and it is not possible to compare with conventional imaging.

The specifications used here are the same as those used in the project. The center frequency is 3 MHz and 308 μm pitch (0.6 times the nominal wavelength) and the 2D array has 50x50 elements. No apodization is used, and the corner elements are removed to approximate a circular array. The parameters used in this simulation are summarized in table I. Only the geometry is changed in the different simulations.
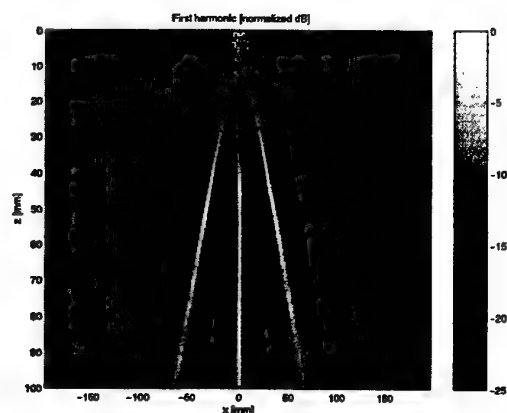
(a) First harmonic.
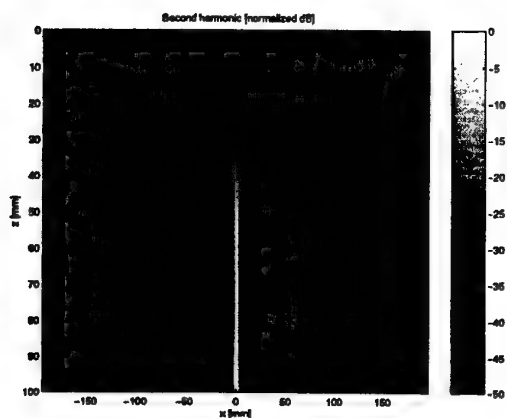
(b) Second harmonic.

Fig. 1. Nonlinear grating lobes

IV. RESPONSE FROM A POINT SCATTERER

A first order approximation to calculate the pulse-echo response is used. It is based on the product of the continuous wave of the transmit and the receive responses, [6].

The two-way response was calculated by assuming nonlinear propagation towards a point scatterer, and linear propagation back to the transducer. The linear propagation of the reflected beam is a valid assumption. The reason for this is that the reflected signal is so weak that it generates almost no distortion of this signal. Simulation of the receiving frequency is set to the double of the transmission frequency because it is the second harmonic that is interesting to study. This way to calculate the pulse-echo is valid in the focus of the beam.

The receive and transmit fields are multiplied and compared to a two-way fundamental image.

V. NONLINEAR GRATING LOBES

When using the nonlinear simulator, a new grating lobe was found at the second harmonic. This new lobe is a kind of grating lobe and appears at half of the sine to the angle of the fundamental.

It is known that fingers are created at the second harmonic. The first report on fingers is from 1973. They were found exper-

imentally by Lockwood et al. [7], and later explained theoretically by Tjøtta et al. [8]. Fingers appear at the second harmonic and they are the lobes that appear approximately between the sidelobe peaks at the fundamental.

The nonlinear grating lobe phenomenon is illustrated in figure 1. The scaling of the images is reduced to -25 dB in the first harmonic figure and -50 dB in the second harmonic. This has been done to make the grating lobes appear clearer since noise is removed. The lobes in the middle of the second harmonic are the nonlinear grating lobes. The phenomenon resembles fingers. The ratio between sine to the grating lobe and this nonlinear grating lobe is found to be approximately .49 in this example.

VI. CONCLUSION

In our study we have found that a grating lobe at $\sin \phi_g$ at the fundamental fundamental frequency results in a new secondary grating lobe at $0.5 \cdot \sin \phi_g$ at the second harmonic. An explanation for this phenomenon can probably be found from the theory of two intersecting beams in a nonlinear medium.

Although details have not been given here, we have found that sidelobes have been reduced by a significant amount for the sparse arrays we have considered. These arrays have between 208 and 880 connected elements on the receiver and transmitter out of the total 2500 elements. In general the two-way sidelobe level at the second harmonic has been reduced by 20-25 dB compared to the fundamental.

VII. ACKNOWLEDGEMENT

REFERENCES

[1] A. Austeng and S. Holm, "Sparse arrays for real-time 3D imaging, simulated and experimental results," *IEEE Ultrasonics Symposium 2000*, October 2000.

[2] D. T. Blackstock, "Thermoviscous attenuation of plane, periodic, finite-amplitude sound waves," *J. Acoust. Soc. Amer*, vol. 36, pp. 534–542, 1964.

[3] K. E. Thomenius, "Impact of nonlinear propagation on temperature distributions caused by diagnostic ultrasound," *IEEE Ultrasonics symposium*, pp. 1409–1413, October 1998.

[4] P. T. Christopher and K. J. Parker, "New approaches to the nonlinear propagation of acoustic fields," *J. Acoust. Soc. Amer*, vol. 90, no. 1, pp. 488–499, 1991.

[5] P. T. Christopher and K. J. Parker, "New approaches to the linear propagation of acoustic fields," *J. Acoust. Soc. Amer*, vol. 90, no. 1, pp. 507–521, 1991.

[6] S. W. Smith, H. G. Pavy, and O. von Ramm, "High-speed ultrasound volumetric imaging system. part I: Transducer design and beam steering," *IEEE Trans. Ultrason., Ferroelect., Freq. Contr.*, vol. 38, no. 2, pp. 100–108, 1991.

[7] J. C. Lockwood, T. G. Muir, and D. T. Blackstock, "Directive harmonic generation in the radiation field of a circular piston," *J. Acoust. Soc. Amer*, vol. 53, no. 4, pp. 1148–1153, 1973.

[8] J. Berntsen, J. N. Tjøtta, and S. Tjøtta, "Nearfield of a large acoustic transducer. part IV: Second harmonic and sum frequency radiation," *J. Acoust. Soc. Amer*, vol. 75, no. 5, pp. 1383–1391, 1984.

Acoustic streaming generated using low burst repetition frequencies and single bursts

G. Pedersen and H. Hobæk

Department of Physics, University of Bergen, Allégt. 55, N-5007 Bergen, Norway

Abstract

At a previous symposium [1] we reported observations of streaming around a needle hydrophone. The hydrophone was positioned near the focus of a focusing ultrasound transducer, and streaming was observed even when using single bursts. No streaming was found without the probe. It was proposed that the origin of this streaming could be excitation of evanescent waves on the probe surface. Presently we report results from a new experiment on this subject. Streaming was observed and measured using tiny tracer particles which were recorded with a CCD-video camera and a computer frame-grabber. The frames were analysed with a Matlab-program for obtaining two-dimensional velocity measurements. The results show that we also observe streaming in free field, and even when using single bursts.

Experimental setup

There are several possible ways to measure acoustic streaming [2-4], or more generally motion in fluids. In our experiments we chose Particle Image Velocimetry (PIV) for several reasons. PIV experimental setups can be made simple and inexpensive.
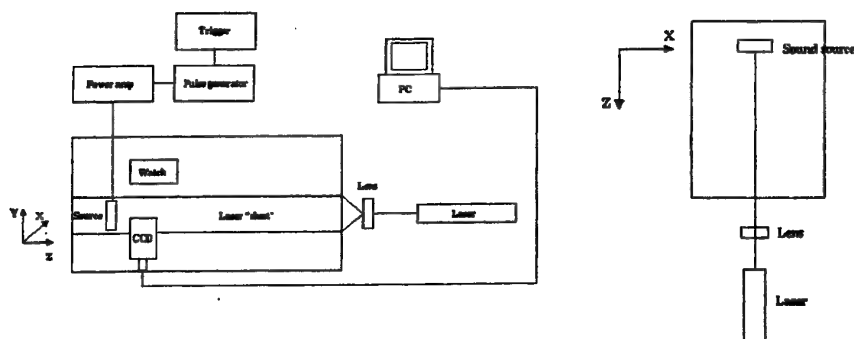

Figure 1: Experimental setup.

The experimental setup is shown in Figure 1. The tank has dimensions $0.3 \times 0.3 \times 0.5\ m$, and is filled with tap water which holds a temperature of $20°C$. The focusing transducer is a

single element of PZT-4D, which has a nominal resonance frequency of 1MHz, a diameter of 36 mm and a nominal focal range of 100 mm. The transducer is mounted air backed in a brass housing, and it is powered by a HP8116A burst/function generator amplified with a ENI240 power amplifier. In addition a HP3312A function generator was used to get a lower burst repetition frequency than 1 Hz (which is the maximum burst repetition frequency possible from the HP8116A). A Saven CI-220 laser together with an external lens was used to produce a laser "sheet" to illuminate a thin slice of the water. The tracer particles used are "polyamid seeding particles", PSP-50, provided by Dantec Measurement Technology. The density of the particles is 1.09 g/cm^3, and the mean diameter is 50 μm. Unfortunately no data on sound velocity in these particles, or the material, are available from the producers. If the sound velocity differs a great deal from that of water, it is possible that we are studying the direct effect of the radiation pressure, and not the acoustic streaming. However, by using colour dye in the water one can make rough estimates of the acoustic streaming, and compare this with the quantitative measurements when using the tracer particles. Approximately the same velocities are obtained, indicating that we are indeed studying acoustic streaming. To capture the streaming a miniature black and white CCD-camera was used, model MTV-261CM, produced by Elfa. The camera sends signals to a frame-grabber (ATI All-In-Wonder 128) mounted in a Compaq Deskpro 2000 PC, where the pictures are stored for later processing. A clock was used to synchronize the pulse/function generator and the frame-grabber. As a basis for calculating streaming velocities MatPIV version 1.4 was used [5]. MatPIV contains a series of Matlab files written by Johan Kristian Sveen to analyse PIV data. Cross-correlation is used to determine the displacement in two captured pictures, two-dimensional FFT is used to calculate the correlation.

Results

Acoustic streaming was studied under several different conditions. The following results show acoustic streaming along the sound-axis of the transducer. The primary parameters that were varied in this study are burst repetition frequency, burst length and burst amplitude. In the results shown in this paper burst amplitude provided to the power amplifier was held constant at a maximum of 1V. In Figure 2 burst length was varied from 100 μs to 400 μs in steps of 100 μs, while burst repetition frequency was held constant at 10 Hz.
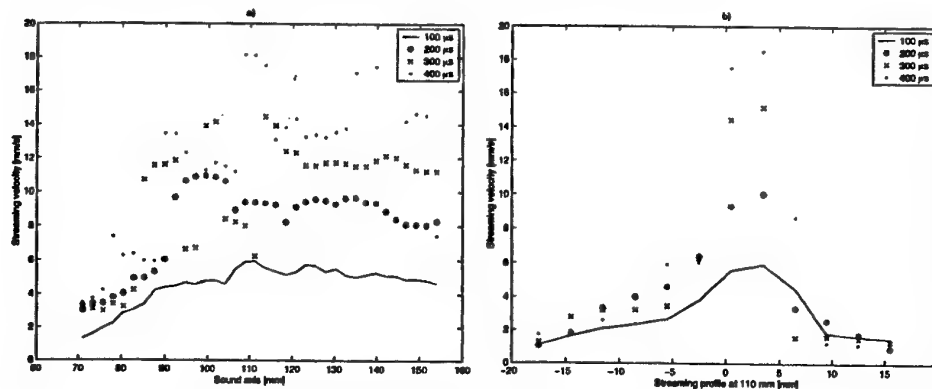

Figure 2: Acoustic streaming, burst repetition frequency 10 Hz.
a) along the sound axis, b) transverse to the sound axis.

Figure 2a shows streaming along the sound axis, while Figure 2b shows the transverse profile of the streaming at 110 mm from the sound source. The streaming was measured after it had reached its maximum value.

Limitations in the experimental setup reduces the maximum streaming velocity which can be measured. The main problem was lack of computer power, which limited the picture quality and the ability to obtain more than 10 frames per second. It is seen in Figure 2 that when the streaming velocity reached 10 mm/s the uncertainty in the measurements increased a great deal. By reducing the burst repetition frequency to 1 Hz, and again varying the burst length one obtained the results shown in Figure 3.
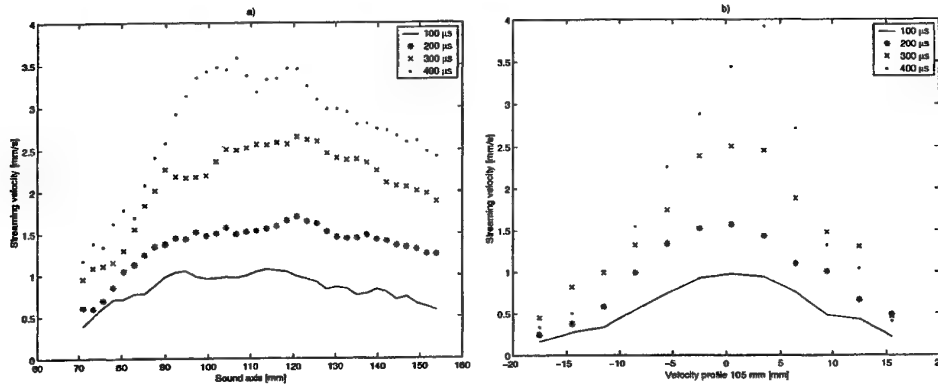
Figure 3: Acoustic streaming, burst repetition frequency 1 Hz.
a) along the sound axis, b) transverse to the sound axis.

The streaming decreased with a factor 5 when the burst repetition frequency was reduced from 10 Hz to 1 Hz. When we used a single acoustic burst, and the length of the burst was varied like in the previous cases, one could still observe acoustic streaming. The velocities are shown in Figure 4. The streaming decreased with a factor 3-4 from the case with burst repetition frequency 1 Hz. But the streaming was still observable. In this velocity range the uncertainty is large, but the results give an indication of the shape and velocity of the single burst streaming.
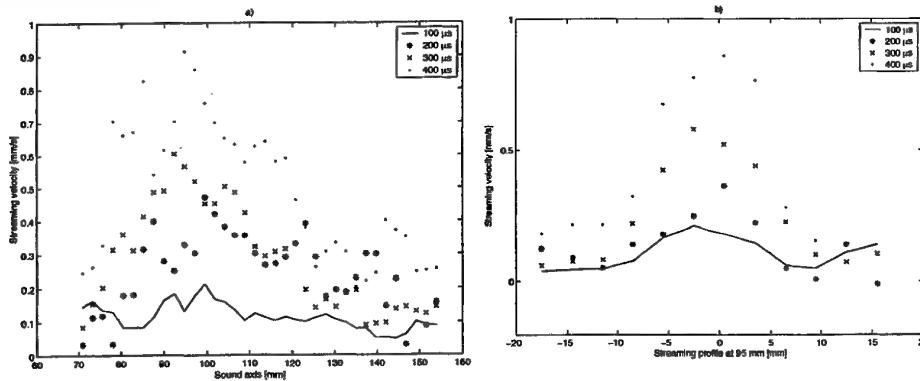

Figure 4: Acoustic streaming, single burst.
a) along the sound axis, b) transverse to the sound axis.

The relation between burst lengths and streaming velocities for the 1Hz and the single burst cases are shown in Figure 5.
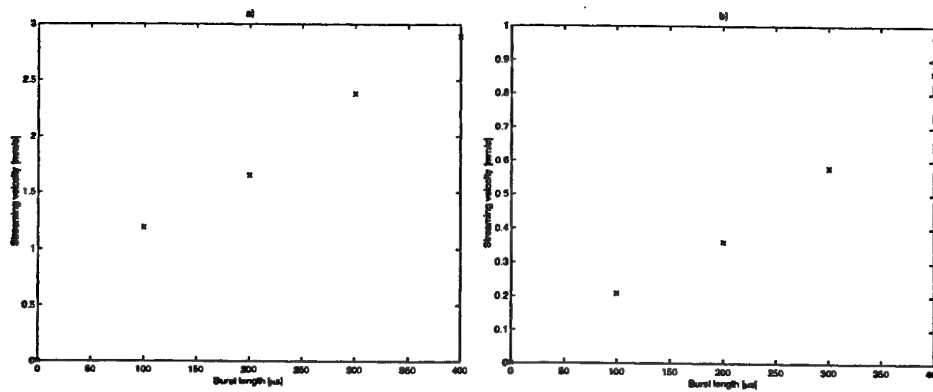
Figure 5: Variation in streaming velocity with burst length. a) 1 Hz, b) single burst.

Decay and rise times of the streaming were also investigated. Figure 6a shows rise time when using a burst repetition frequency of 10Hz and a burst length of 100 μs. The sound was turned on at time 0 s, and turned off after about 6 s. In Figure 6b a single acoustic burst with burst length 400 μs was used. The burst was transmitted to the fluid at time 0 s. As can be seen in Figure 6a, it took longer time for the streaming to reach its maximum than in the single burst case.
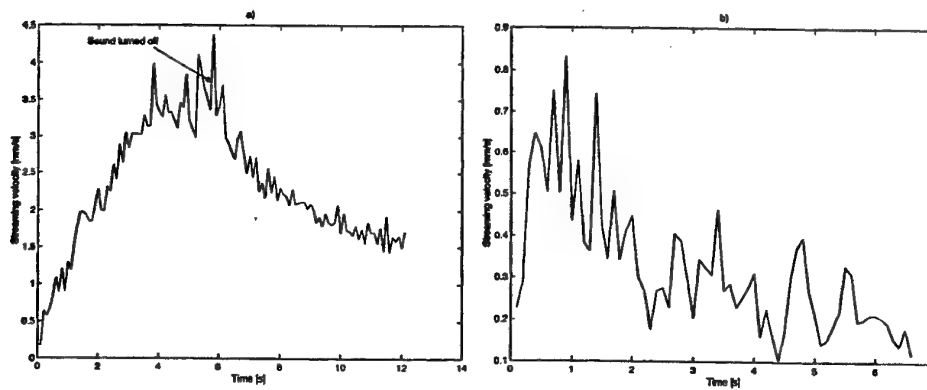
Figure 6: Acoustic streaming, decay and rise time.
a) 10 Hz burst repetition frequency, b) single burst.

When we used a single acoustic burst the maximum velocity was reached right after the burst had passed through the fluid. In the 10 Hz case if the sound is continued after 6 s, the streaming ends up with the velocity shown in Figure 2.

Conclusion

In this study we have investigated acoustic streaming. It has been shown that even a single burst can produce observable acoustic streaming. The streaming reaches its maximum value faster in time with a single burst than when using more than one burst. It is also observed that as the burst repetition frequency is reduced, the streaming along the sound axis falls off faster after it has reached its peak. The maximum also seems to move closer to the sound

source, and the transverse profile broadens. Contrary to our previous findings this streaming is not dependent on evanescent waves, but exist in free field.

References

[1] T. Berge and H. Hobæk: On two peculiar effects observed in high intensity ultrasound beams. Proceedings of the 22nd Scandinavian Symposium on Physical Acoustics. U. R. Kristiansen (ed.) (1999).

[2] H. C. Starritt, F. A. Duck and V. F. Humphrey. An experimental investigation of streaming in pulsed diagnostic ultrasound beams. Ultrasound in Med. & Biol. **15** (1989) 363-373.

[3] H. C. Starritt, C. L. Hoad, F. A. Duck, D. K. Nassiri, I. R. Summers and W. Vennart. Measurement of acoustic streaming using magnetic resonance. Ultrasound in Med. & Biol. **26** (2000) 321-333.

[4] A. Nowicki, T. Kowalewski, W. Secomski and J. Wójcik. Estimation of acoustical streaming: theoretical model, Doppler measurements and optical visualization. European Journal of Ultrasound **7** (1998) 73-81.

[5] J. K. Sveen: An introduction to MatPIV v. 1.4 (www.math.uio.no/~jks/matpiv/). Department of Mathematics, University of Oslo. (2000).

SOME APPLICATIONS OF MULTIPLE FREQUENCY ECHO SOUNDER DATA

Rolf J. Korneliussen and Egil Ona, Institute of Marine Research,
P.B. 1870 Nordnes, N-5817 Bergen, NORWAY, email: rolf@imr.no

ABSTRACT *Multiple-frequency acoustic data collected on routine surveys may improve the quality of scrutinised data as compared to single frequency data. Multiple frequency data is also used to investigate herring avoidance reactions during passage of a research vessel. Utilising the strong difference in directivity of adult herring at 18, 38 and 120 kHz, a comparison of the integrated backscattered echo intensity as a function of depth suggests that most of the reduction in echo energy during passing must be due to density dilution, rather than to diving.*

INTRODUCTION Fish is the second most important Norwegian merchandise, and its importance is increasing. The Institute of Marine Research (IMR) is responsible for assessment of important fish species in Norwegian waters, and so far the use of acoustical methods as the first step in abundance estimation seem to give as least as accurate estimations for most species as any other method [1]. IMR collects large amounts of acoustic data during 1500 ship-days at sea per year, and these data needs to be processed during the 2 – 3 hours available time per day at each cruise. Fig. 1 illustrates the procedure to scrutinise the acoustic data.

Each species is frequently surveyed at the time of year when it is most favourably distributed. On acoustic surveys, only a few species are scrutinised to the highest accuracy due to the limited capacity for biological sampling. The experience of the operator is essential in the scrutinising process. Scattering models applied on the multiple frequency data are used to either retain the acoustic returns from the wanted targets only, or to exclude the returns from the unwanted targets, and thus, improve the quality of the scrutinised acoustic data as compared to data achieved from single frequency techniques. Requirements for collection of optimal multiple frequency data were discussed by Korneliussen [2] as well as some methods for visualisation of such data. Acoustic signatures are used to discriminate between simple classes of acoustic targets [3].
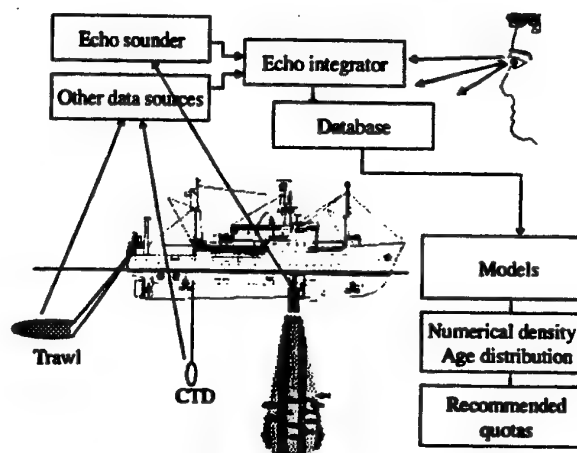

Fig. 1. Interpretation of acoustic data.

Multiple frequency data can also be used to investigate vessel avoidance, which is regarded the most important bias in acoustic abundance estimates of pelagic fish [4]. During wintering, the important pelagic stock of the Norwegian Spring Spawning herring (*Clupea Harengus L.*) is found in horizontally concentrated, distinct layers, and favourably structured for mapping and abundance estimation [5]. However, the measured hourly mean acoustic backscattering coefficient of the over-wintering herring is 3 times larger during the 6 hours of twilight as compared to the 18 hours of night. The reaction by herring to vessel noise [6] is according to modelling theory [7][8] a combination of horizontal avoidance and diving, depending on when the flight reaction occur in relation to the position of herring relative to the vessel. Adult herring, 27 – 37 cm are quite directive targets at the echo sounder frequencies used [9], and a systematic change in tilt angle distribution may dramatically change the backscattered energy, even at constant within-beam fish density. For dense layers of herring, we suggest that the sharp directivity of herring may be used to extract information on the behaviour of the fish within the vertical beams of the passing vessel. All topics with respect to herring vessel avoidance may not be investigated from the measuring platform, but the relation between dilution and diving may be studied. The results may be important for modelling of herring avoidance for correction of measurement bias, but may also be used during selection of optimal echo sounder frequencies for herring research.

DATA COLLECTION IN GENERAL Calibrated multiple frequency acoustic data [10][11] for both applications below were collected in 1999 from R/V "G. O. Sars" cruising at normal vessel speed, 11 knots. The transducers were mounted close together on a protruding keel [12]. The transducers at resonance frequencies 18, 38, 120 and 200 kHz have nearly identical (11^0, 7^0, 7^0 and 7^0) half power beam angles. A special software version of the Simrad EK500 echo sounder [13] was used to achieve an identical burst-length and a high digital sampling rate at all frequencies. The data was corrected for noise [14][15] and scrutinised in the post-processing system [16] after collection.

APPLICATION I: EXTRACTION OF MACKEREL FROM MIXED ACOUSTIC RECORDINGS The data was collected in the North Sea in October 1999, and the biological sampling was optimised for mackerel (*Scomber Scombrus L.*). The acoustic signatures are integrated into the post-processing system [16] to generate a masking matrix for extraction of the acoustic returns from the target species mackerel only, and thus, to exclude echoes from all other targets. The masking matrix contains the number 1 for the elements representing volume-segments classified as mackerel, and zero elsewhere. Fig. 2a-d below shows the original acoustic data corrected for noise. The two curves in the upper part of the figure shows the acoustic signature of mackerel (left) and some other species (right). Since we only had biological trawl-samples for mackerel here, we are not able to tell which species the right signature represents (or even if it is a single or many species). Fig. 2e shows the 200 kHz echogram multiplied by the masking matrix and Fig. 2d shows the colour scale used to visualise the acoustic data.

s_v-frequency-dependency relative to $s_{v,38}$

a) 18 kHz
b) 38 kHz
c) 120 kHz
d) 200 kHz
e) S_v [dB]
e) Mackerel at 200 kHz
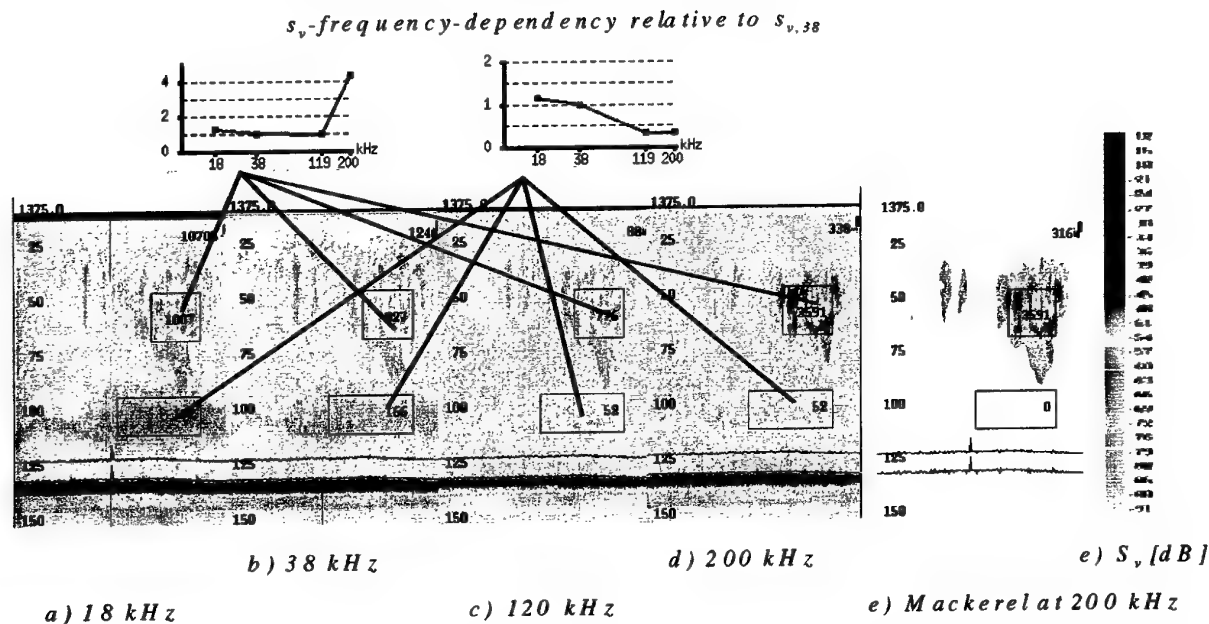
Fig. 2 Original echograms from the North Sea after noise removal (a-d) and a 200 kHz echogram where only the target-category "mackerel" is retained. This is achieved by multiplying the original 200 kHz data with the masking matrix. Fig. e shows the colour scale used.

APPLICATION II: VESSEL AVOIDANCE FROM MULTIPLE FREQUENCY DATA The data was collected in Ofotfjord January 1999 in Northern Norway, in the wintering area of the Norwegian Spring Spawning herring. A typical night time recording of herring at the commonly used echo sounder frequency, 38 kHz, is shown in Fig. 3.

Avoidance is expected to be strong in the upper layers during night. No significant avoidance is expected to occur in the deeper layers at night, below 150 m depth, or in the daytime recordings, where all herring is registered deeper than 150 m. The deeper layers, both day and night will therefore later be used as "reference" layers, with assumed insignificant vessel avoidance. In these layers, the herring is observed dorsally at three simultaneously working echo sounder frequencies. After calibration and noise-correction the observed acoustic quantity between the depths z_1 and z_2 is the mean area acoustic backscattering coefficient with units [m²/n.mi.²]:

$$s_A = 4\pi(1852)^2 \int_{z_1}^{z_2} s_v dz \qquad (1)$$

Fig.3. Two nautical miles of a typical night time recording of herring

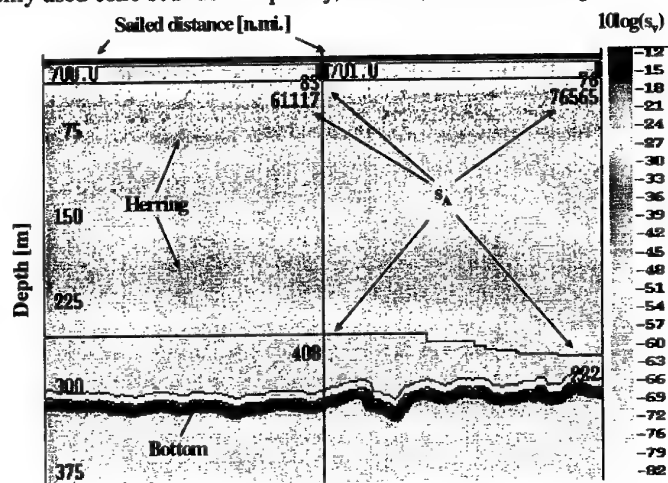The effect of observation volume is accounted for in the equivalent beam angle of the particular transducer used. The mean volume backscattering coefficient, $<s_v>$, is the product between the mean volume density of fish, $<\rho_v>$, and the mean backscattering cross section, $<\sigma>$, of the fish: $<s_v> = <\rho_v><\sigma>$ (2)

Further, the mean backscattering cross section, $<\sigma>$, for a directive scatterer is the convolution of its directivity pattern, $\sigma = \sigma(\theta)$, and its tilt angle distribution $p = p(\theta)$ [15]. It is assumed that both the volume density and the tilt angle distribution is the same in all three beams, at any depth. The expected differences in integrated energy across frequency must therefore be derived from differences in the fish directivity pattern, $\sigma(\theta)$. An example of this for an adult herring is indicated in Fig. 4 for 18 and 38 kHz.

The sharper main lobe of the directivity pattern at 38 kHz compared to 18 kHz, and even sharper at 120 kHz (not shown), makes the 18 kHz fairly stable for moderate changes in tilt angle distribution. At the two higher frequencies, however, moderate changes, in particular in mean tilt may cause a severe reduction in backscattered echo intensity. In result, if the fish is moving from a natural, horizontal swimming mode to a diving mode, it should affect the frequencies differently. Actually, by computing the difference in target strength from the directivity pattern, as a function of diving angle, the relative drop on target strength may be studied as a function of angle, Fig 5.

If the unaffected layers may be used as reference layers, and the ratio between integrated echo intensity between frequencies:

$$\Delta TS = 10\log(\Delta\sigma); \quad \Delta\sigma = s_{A,120}/s_{A,18} \text{ or } \Delta\sigma = s_{A,38}/s_{A,18} \quad (3)$$

is studied as a function of depth, a substantial drop is expected in the layers where the fish is diving, at least for moderate mean diving angles, Fig. 5. During data selection, a detailed scrutinising of one 24-hour cycle of survey data from January 8 to 9 was made at all three frequencies, and stored in 20-m layers, 30-minute sections. Further, to avoid working with low-density regions, a minimum area backscattering coefficient of $s_A = 500$ [m²/n.mi.²] (0.0073 fish/m³) was applied as lower limit.

Fig 3. Target strength of a 30- cm herring as a function of tilt angle θ over $\pm 45°$

Fig. 5. Expected relative drop in target strength or volume backscattering strength between frequencies as a function of mean diving angle(smoothed and normalised data).

RESULTS AND DISCUSSION: APPLICATION I Comparison of the retained 200 kHz data in Fig. 2e with the biological trawl-samples and Fig. 2d shows a discriminating power between mackerel and all other targets. A successful generation of a reasonable masking matrix (which is extracted from a target classification matrix) requires high quality of the collected acoustic data as described by Korneliussen [2]. In reality, it is not a single target, but a volume-segment that is classified. Even though the echo sounder, the transducers and the internal transducer mounting are adapted to meet these requirements, noise removed, the data is not perfect for the generation of the target classification matrix. Thus, both the noise-corrected multiple frequency acoustic data at its original resolution and a smoothed version of the same data are used as input to the classification system. The classification system is further implemented as hierarchical expert system where the first trial uses a set of strict rules for a volume-segment to be classified. In the following trials, the requirements on the acoustic data itself are loosened as compared to the first trial, but also the classification of the neighbouring volume-segments are used.

For mackerel in particular, the classification seems to be successful, and the automatic classification system also reduces the time needed to scrutinise the acoustic data. For other targets than mackerel, the classification seems to be promising, but these can only partly be verified by the biological sampling. This is due to the insufficient depth-resolution and limited capability of the present sampling tools in separating the different types of biological targets.

RESULTS AND DISCUSSION: APPLICATION II The very dense concentrations of herring in the survey area may defend the use of the 120 kHz system well outside the normal use for plankton and single fish, 125 – 150 m, and the signal to noise ratio is still good at 300 m. Fig. 6 shows the depth dependency of the ratio of the mean area backscattering coefficients, $r_1 = c_1(s_{A,38}/s_{A,18})$ and $r_2 = c_2(s_{A,120}/s_{A,18})$ where the constants, c_1 and c_2 are the normalising constants.
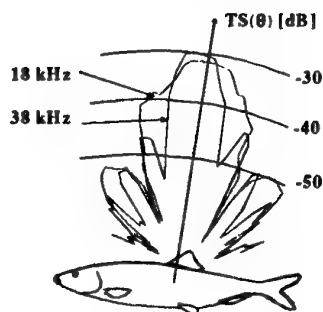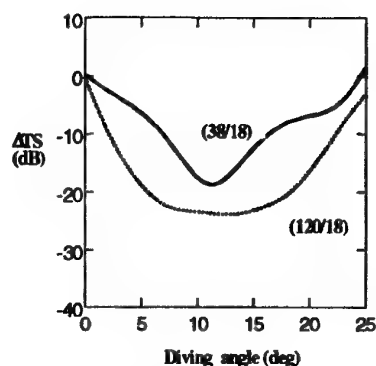
For diving being the only avoidance reaction of herring, r_1 and r_2 should increase rapidly with depth, at least down to 100 m below the surface, and then stabilise at a maximum value at larger depths. Inspection of Fig. 3 shows that even a moderate mean diving angle, e.g. 5 degrees, should give a significantly larger effect than the one observed. For density draining being the major avoidance reaction, there should non, or only a weak depth dependency of r_1 and r_2. The limited response seen here therefore suggests that the avoidance observed in the shallow layers of herring at the wintering area are mainly caused by horizontal dilution. The discontinuity at about 100 m is however interesting, as r_1 here turn back towards 1.0 in the more shallow layers. This may indicate either that the fish is swimming more horizontal again, or that the fish is diving at a very steep angle, as suggested in [8]. As seen from Fig. 5, the ratio also turns against normal values at high diving angles. The clear but weak response seen in both measures may nevertheless indicate some diving, in particular between 100 – 200 m where the deviations are significant at both frequencies. Since the magnitude of the response is low, other effects may also affect the results. These are depth dependent target strength, frequency dependent extinction and others. Before a more firm conclusion can be made, these factors should be investigated, and comparative data from a drifting ship, with stopped main engine should be collected. This would easily isolate acoustic and behavioural effects on the measured ratios.
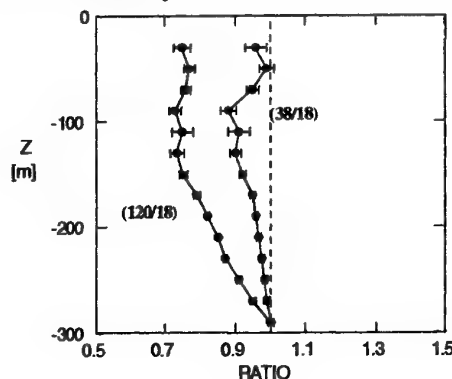

Fig.6. Depth dependency of the normalised ratio of the mean area acoustic backscattering coefficients.

CONCLUSIONS Multiple frequency acoustic data may significantly improve the quality of the scrutinising process in acoustic surveys within the 2 – 3 hours available time available per day. The multiple frequency data may also be used extract sensible classification parameters, as well as investigate the fish vessel avoidance. Thus, some of the uncertainty of the estimated fish stock abundance is reduced.

REFERENCES
1. **Nakken, O. and Ulltang, Ø., 1983.** A comparison of the reliability of acoustic estimates of fish stock abundance and estimates obtained by other assessment methods in Northeast Atlantic. FAO Fish.Rep., (300):249-260.
2. **Korneliussen, R., 1999.** Multifrequency echograms, Proceedings of the 22nd Scandinavian Symposium on Physical Acoustics, 3-4.
3. **Korneliussen, R., 2000.** Application of acoustic signatures of biological scatterers, Proceedings of the 23th Scandinavian Symposium on Physical Acoustics, 15-16.
4. **Olsen, K., Angell, J., Pettersen, F. and Løvik, A., 1983.** Observed fish reactions to a surveying vessel with special reference to herring, cod, capelin and polar cod. FAO Fish. Rep., 300, 131-138.
5. **Røttingen, I., 1992.** Recent migration routes of Norwegian spring spawning herring. ICES CM 1992/H: 18.
6. **Mitson, R.B.** Research vessel noise signatures. ICES Mar. Sci. Symp., Vol.196:147-152, 1993.
7. **Vabø, R., 1999.** Measurement and correction models of behaviourally induced biases in acoustic estimates of wintering herring. Thesis, PhD, University of Bergen.
8. **Olsen, K., Angell, J. And Løvik, A., 1983.** Quantitative estimations of the influence of fish behaviour on acoustic estimates of fish abundance. FAO Fish Rep. 300, 139-149.
9. **Nakken, O., and Olsen, K., 1977.** Target strength measurements of fish. Rapp. P.-v.   Réun. Cons. perm. int. Explor. Mer, 170:52-69.
10. **Foote, K. G., 1982.** Optimizing copper spheres for precision calibration of hydroacoustic equipment, The Journal of the Acoustical Society of America, 71: 742-747.
11. **Foote, K. G., Knudsen, H. P., Vestnes, G., Maclennan, D. N., and Simmonds, E. J., 1987.** Calibration of acoustic instruments for fish density estimation: a practical guide. Int. Coun. Explor. Sea Coop. Res. Rep., 144: 57pp.
12. **Ona, E. and Traynor, J., 1990.** Hull mounted, protruding transducer for improving echo integration in bad weather. C.M. 1990/B:31
13. **Bodholt, H., Nes, H., and Solli, H., 1989.** A new echo-sounder system. Int. Conf. Progress in Fisheries Acoustics, Lowestoft. Proc. I. O. A., St Alban, UK, 11(3): 123-30.
14. **Korneliussen, R., 1998.** Echogram noise quantification. Proceedings of the 21th Scandinavian Symposium on Physical Acoustics, 3-4.
15. **Korneliussen, R., 2000.** Measurement and removal of echo integration noise. ICES Journal of Marine Science, 57, 1204-1217.
16. **Foote, K. G. , Knudsen, H.P., Korneliussen, R.J., Nordbø, P.E. and Røang, K., 1991.** Postprocessing system for echo sounder data. J. Acoust.Soc. Am., 91(4), 1983-1989.

A ray theory approach to investigate the influence of flow velocity profiles on transit times in ultrasonic flow meters for gas and liquid

Kjell-Eivind Frøysa and Per Lunde,
Christian Michelsen Research AS, Bergen, Norway

1. Introduction

Multipath ultrasonic transit-time meters for gas and liquid flow measurement (USM) have already been developed to a stage where they are considered as competitive alternatives to the more conventional orifice plate, turbine and positive displacement meters for fiscal metering of natural gas and oil products, particularly for transmission line applications. USM technology offers significant operational advantages such as no moving parts, non-intrusive measurement (no obstruction of flow), no pressure loss, and bi-directional operation (reducing need for pipework). Compact metering stations can be constructed on basis of the large turn-down ratio of USMs (40:1 or larger for gas meters, 20:1 or larger for liquid meters (tentatively), reducing the need for a multiplicity of meters to cover a wide flow range), and the short upstream/downstream requirements with respect to bends (10D and 5D for gas meters, typically). Measurement possibilities are offered which have not been available earlier, such as fast time response and flow monitoring (e.g. pulsating flow, flow velocity profile; sound velocity profile), and self-checking capabilities (from sound velocity, signal level, etc.). In gas there has been demonstrated potentials of additional information such as gas density and calorific value determination. The potential of remote operation of USMs is an interesting perspective.

For natural gas, the first generation of USMs have been on the market for about 5-10 years [1-3]. USMs have demonstrated their capability to provide metering accuracy within national regulation requirements [4,5]. Better than ±0.7 % uncertainty (of measured value) is being reported, as required for custody transfer in large commercial pipelines. In appropriate applications, multi-path ultrasonic meters can offer significant cost benefits. USM technology is increasingly gaining acceptance throughout the industry, and is today in use in gas metering stations onshore and offshore. ISO standardization work has been started [6].

For metering of oil and petroleum products, USMs for liquids have for many years represented a robust alternative in non-fiscal applications. USMs have recently been introduced also for fiscal metering [7], and 0.15 - 0.25 % uncertainty is claimed, based on *in-situ* flow calibration (using prover). The petroleum industry is at present gaining field experience with this new fiscal liquid metering technology [8].

On the other hand, a relatively small measurement error in the flow rate measured by a USM can easily translate into a large sum of money. For example, an estimate of Norway's export of natural gas in 2000 is about 6000 million USD. Present-day technology for fiscal and sales metering of gas is at a level of 0.5-1 % uncertainty (of measured value). A systematic error in the

flow measurement of, say, 0.5 % (which is still within usual national regulations for gas measurement [5]) would translate into a measurement uncertainty corresponding to an annual value of about 30 million USD for this 2000 gas export estimate. This means that even an uncertainty of about 0.2-0.3 % in some cases is considered as uncomfortable in the industry. Investigations have shown that there are un-exploited potentials in USM technology, such as to reduce systematic errors (cf. [9]).

For example, effects of flow velocity profiles have been widely studied with respect to USM *integration methods* (multipath effects), and is still an area of active research experimentally and theoretically. However, the effects of flow velocity profiles on the acoustic *transit times* have rarely been studied. Such effects will be systematic, and can be of relevance, especially for gas meters operating at high flow velocities. They will influence both on the measured flow velocity and sound velocity.

The measured sound velocity in a USM has traditionally been used for self-check of the meter. Recently, algorithms have been developed for measurement of the gas density based on the measured sound velocity [10]. This means that precise measurement of the sound velocity is now of even higher importance than a few years ago.

Even in relatively "simple" pipework applications, such as straigth pipes (relevant e.g. for metering at gas and liquid transmission networks), the axial flow velocity profiles may take significantly different "shapes", depending on the Reynolds number of the flow, Re. The shape of actual profiles influences on the USM measurement.

In metering stations where compactness is important (e.g. offshore), complex installation conditions (pipe bends, flow conditioners, etc.) cause disturbed flow velocity profiles which influence on the USM measurement. This concerns both axial and transversal flow velocity components.

Transversal flow components will occur especially when the USM is installed downstream bends and other obstructions of the pipe flow. It is expected that downstream a double bend out of plane, the transversal flow regime is typically a swirl, while downstream a single bend, a cross flow is typically established. Such transversal flow components can contribute to the flow measurement performed by each acoustic path. There are examples from installations downstream double bends out of plane where the transversal flow components can be 10 % of the axial flow component, or larger. In practice, the transverse flow components will often neither be a symmetric swirl nor a symmetric cross flow, but instead some kind of an asymmetric variant of either swirl or cross flow, or something inbetween.

In the present work, the accuracy of the traditional expressions used in today's USMs for measurement of flow velocity and sound velocity, with respect to flow profile effects on *transit times*, is investigated by use of ray theory. The influences of axial and transversal flow profiles are both studied. Computational fluid dynamics (CFD) modelling of pipe flow is used to establish representative analytical expressions for acoustic path profiles (axial and transversal). The analytical path profiles are then used as input to a ray theory model for sound propagation in pipe flow, to evaluate effects of more realistic, non-uniform flow profiles (axial and transversal) on the acoustic transit times. The ray theory simulation results are compared with the simpler

and more traditional analytical expressions for the acoustic transit times, derived for the simplified case of uniform axial and transversal flow profiles. The resulting errors in flow velocity and sound velocity for the traditional USM functional relationships are evaluated and discussed.

2. Current theoretical basis for USM flow metering methodology

A USM measures the axial (x) component of the volumetric flow rate at line conditions (with respect to pressure, temperature and fluid quality), q_v, defined as

$$q_v = \iint_A v_x(y,z) dy dz \,, \tag{1}$$

where A is the cross sectional area (in the y, z - plane) of the pipe, cf. Fig. 1, and v_x is the axial (x) component of the flow velocity. For circular cross-section, the double integral in Eq. (1) can be written as a single integral [11, 9],

$$q_v = \int_{-R}^{R} \int_{-\sqrt{R^2-y^2}}^{\sqrt{R^2-y^2}} v_x(y,z) dz dy = 2\int_{-R}^{R}\sqrt{R^2-y^2}\,\bar{v}_x(y) dy \,, \tag{2}$$

where $R = D/2$ is the inner radius of the pipe and

$$\bar{v}_x(y) = \frac{1}{2\sqrt{R^2-y^2}} \int_{-\sqrt{R^2-y^2}}^{\sqrt{R^2-y^2}} v_x(y,z) dz \tag{3}$$

is the average axial flow velocity (the line integral) over the chord with lateral position y.

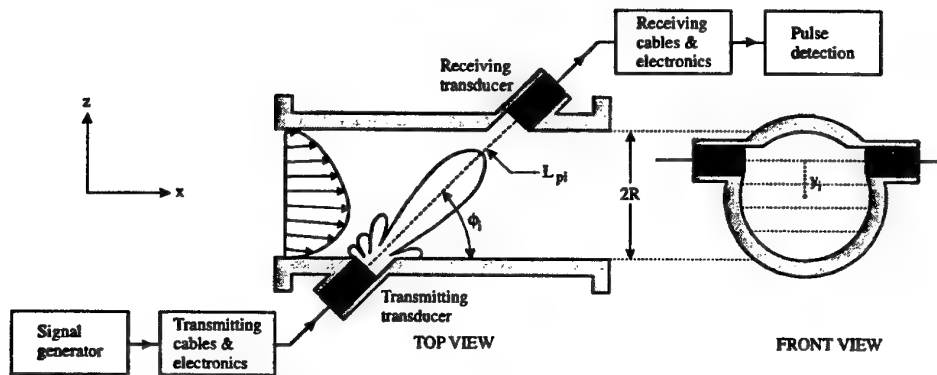Fig. 1. Schematic illustration of a single path (no. i) in a multipath ultrasonic gas flow meter (for downstream sound propagation). (Left: centre path example ($y_i = 0$); Right: path at lateral chord position y_i.)

In USMs used for fiscal metering, the flow velocity is measured using a finite number of acoustic paths, typically 4-6, each path corresponding to a chord over the pipe cross section, cf. Fig. 1 [11,

9]. For each path, transit times are measured electronically for high-frequency ultrasonic pulses propagating across the pipe, at an angle, ϕ_i, with respect to the pipe axis, downstream with the flow, and upstream against the flow. Ultrasonic transducers are used to transmit and receive the signals, and the measured transit times are corrected for time delays due to electronics, cables, transducers, diffraction, transducer cavities, etc. For each acoustic path, the difference between the upstream and the downstream propagating transit times is proportional to the average flow velocity along the acoustic path. Multiple acoustic paths are used to sample the flow velocity profile in the pipe at a set of discrete chords, to improve the metering accuracy.

In this approach, thus, Eq. (2) is solved by numerical integration, giving

$$q_v \approx \pi R^2 \sum_{j=1}^{N_c} w_j^c \bar{v}_{j,x}^c ,$$

(4)

where N_c is the number of chords (typically 4-5), w_j^c are the integration weight factors, $j = 1, ...,$ N_c, $\bar{v}_{j,x}^c = \bar{v}_x(y_j)$ and chord no. j is located at $y = y_j$.

In practice, the flow velocity is measured over N acoustic paths, having inclination angles to the axial flow direction of typically 40° to 50°, and where the projection of one such acoustic path constitutes one of the chords used above. For each such acoustic path, the upstream and downstream transit times are measured.

2.1 Traditional approach; uniform axial flow and no transversal flow

For the simplified case where the flow velocity profile is assumed to be uniform and purely axial (i.e. no transversal flow components), the transit times of path no. i can be found by a simple geometrical approach as (see Fig. 2a)

$$t_{1i} = \frac{L_i}{c - \bar{v}_{i,x} \cos\phi_i}; \qquad t_{2i} = \frac{L_i}{c + \bar{v}_{i,x} \cos\phi_i} ,$$

(5)

where L_i is the interrogation length, ϕ_i the inclination angle of the acoustic path, and t_{1i} and t_{2i} are the upstream and downstream transit times, respectively. $\bar{v}_{i,x}$ is the average axial flow velocity over acoustic path no i, and c is the velocity of sound (VOS). From Eqs. (5) it is easily seen that

$$\bar{v}_{i,x} = \frac{L_i(t_{1i} - t_{2i})}{2t_{1i}t_{2i} \cos\phi_i} .$$

(6)

Alternatively, a more sophisticated and accurate ray tracing approach can be taken, as reported by McCartney *et al* [12], leading to

$$t_{1i} = \frac{L_i}{\sqrt{c^2 - \bar{v}_{i,x}^2 \sin^2 \phi_i} - \bar{v}_{i,x} \cos \phi_i} \; ; \quad t_{2i} = \frac{L_i}{\sqrt{c^2 - \bar{v}_{i,x}^2 \sin^2 \phi_i} + \bar{v}_{i,x} \cos \phi_i} \; . \tag{7}$$

Eq. (7) is claimed by McCartney *et al.* to be valid also for non-uniform flow velocity profiles. However, an underlying assumption in their analysis is that the rays are straight lines. This is possible for uniform flow profiles only, and Eq. (7) is therefore valid only for uniform axial flow profile and no transversal flow components [11, 9].

It is interesting to note that Eq. (7) leads to exactly the same expression, given by Eq. (6), for the average flow velocity over the acoustic path, $\bar{v}_{i,x}$, as the simplified geometrical approach described above and illustrated in Fig. 2a.
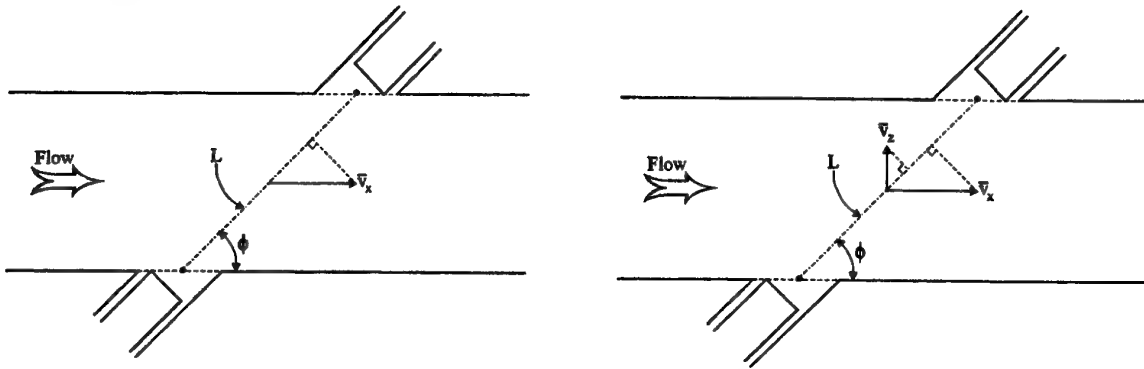

Fig. 2.   Schematic illustration of two simplified "geometrical" approaches which may be used to account for flow velocity components in the USM functional relationships:
(a) Traditional approach; uniform axial flow profile only, and no transversal flow,
(b) Slightly improved approach; uniform axial flow profile and uniform transversal flow profile.

Eqs. (7) also leads to the well-known expression for the sound velocity,

$$c = \frac{L_i \sqrt{(t_{1i} + t_{2i})^2 \cos^2 \phi_i + (t_{1i} - t_{2i})^2 \sin^2 \phi_i}}{2 t_{1i} t_{2i} \cos \phi_i} \; . \tag{8}$$

The velocity of sound has traditionally been used for self-checking in USMs. In addition, recent developments have shown that it can be used as a basis for calculation of density or calorific value of a natural gas [10]. Through the velocity of sound, therefore, a USM can be used as a mass flow meter or an energy flow meter, in addition to its more traditional use as a volumetric flow meter. In such new applications, a sound velocity measurement with a uncertainty of about ±0.25 m/s or better, will be needed for fiscal measurement of density or calorific value [19]. In non-fiscal applications, a less accurate sound velocity measurement may be acceptable.

2.2 Improved approach; uniform axial and transversal flow profiles

In a real flow metering situation, there will be transversal flow velocity components in addition to the axial flow velocity component. Such transversal flow velocity components may influence on

86

the transit times, and thus also on the estimated flow and sound velocities. In the simplest approximation, both the axial and the transversal flow velocity components are considered to be uniform. A simple, geometrical approach can again be taken, giving the following upstream and downstream transit times (see Fig. 2b):

$$t_{1i} = \frac{L_i}{c - \bar{v}_{i,x} \cos\phi_i - \bar{v}_{i,z} \sin\phi_i}; \qquad t_{2i} = \frac{L_i}{c + \bar{v}_{i,x} \cos\phi_i + \bar{v}_{i,z} \sin\phi_i}, \qquad (9)$$

where $\bar{v}_{i,z}$ is the average transversal flow velocity component in the z direction. From Eqs. (9), c can be eliminated, giving

$$\bar{v}_{i,x} + \tan\phi_i \bar{v}_{i,z} = \frac{L_i(t_{1i} - t_{2i})}{2t_{1i}t_{2i}\cos\phi_i}, \qquad (10)$$

as an improvement relative to Eq. (6). In actual fiscal flow meters, Eqs. (6) or (10) (for flow velocity) and Eq. (8) (for sound velocity) are the expressions used to obtain the average flow velocity and sound velocity at acoustic path no. i.

Note that Eq. (8) is "exact" (within the ray approximation) for the uniform axial flow profiles when the transversal flow component, v_z, is zero. Eq. (10) is expected to be a good approximation for uniform axial and transversal flow profiles.

In Eq. (4), the average axial flow velocity over the chord, $\bar{v}_{j,x}^c$, is needed, while in Eqs. (6) and (10) the average axial flow velocity over the inclined acoustic path, $\bar{v}_{i,x}$, is involved. It is usual to assume that these two quantities are approximately equal,

$$\bar{v}_{j,x}^c \approx \bar{v}_{i,x}, \qquad (11)$$

for corresponding chord and acoustic paths. Hence, in this approximation it is assumed that the axial flow velocity profile is constant over the metering volume of the USM. However, in order to obtain $\bar{v}_{i,x}$, a complication is that in the USM, it is found in a linear combination with the transversal flow component, $\bar{v}_{i,z}$, see Eq. (10), and not isolated as needed in Eq. (4). In order to treat this complication, Eq. (4) is written as

$$q_v \approx \pi R^2 \sum_{j=1}^{N_C} w_j^c \bar{v}_{j,x}^c \approx \pi R^2 \sum_{i=1}^{N} w_i \bar{v}_i, \qquad (12)$$

where the inclination angles ϕ_i and the integration weights w_i are chosen to reduce the influence of the transversal flow components. N is here the number of acoustic paths in the flow meter, typically 4-6, and

$$\bar{v}_i = \frac{L_i(t_{1i} - t_{2i})}{2t_{1i}t_{2i}\cos\phi_i},$$

(13)

cf. Eqs. (6) and (10).

In the case where there is one acoustic path per chord, so that $N = N_c$, the weights w_i are equal to the weights w_j^c. In the case where there are 2 acoustic paths per chords (for all or some of the chords), the relation between the weights w_i, $i = 1, ..., N$ and w_j^c, $j = 1, ..., N_c$ will be more complex. It should also be noted that it is only when there are 2 acoustic paths per chord for every chord, i.e. $N = 2N_c$, that the transversal flow velocity component $\bar{v}_{i,z}$ in Eq. (10) will be cancelled for any transversal flow profile. For a smaller number of acoustic paths, only certain transversal flow velocity profiles will in general be cancelled. However, in many cases, it is possible to design the integration weights so that the transversal flow velocity components of main interest in ultrasonic flow metering will be reduced.

The traditional expressions on which today's USMs are based, given by Eqs. (6) or (10) (for flow velocity) and Eq. (8) (for sound velocity), are based on assumptions of uniform axial and transversal flow velocity profiles, as explained above. In a real flow metering situation, the axial and transversal flow velocity components will rarely be uniform, cf. Section 1, and the traditional expressions represent approximations. In the following, the accuracies of the traditional expressions Eq. (8) and (10) are investigated, when more realistic disturbed (non-uniform) axial and transversal flow profiles are taken into account.

3. Flow velocity profiles (axial and transversal)

In Section 5, the traditional USM expressions given by Eqs. (8) and (10) will be investigated using a ray theory accounting for non-uniform axial and transversal flow velocity profiles. As input to the numerical ray-tracing model, 3-dimensional flow profile data are needed. This could in principle be treated using CFD-calculated flow profile data directly into the ray-tracing model. In the present work, a slightly more simplified approach is used, in which the axial and transversal flow profiles are described by analytical formulas. In order to make representative analytical input flow velocity profiles, CFD calculated flow profiles have been studied using CMR's CFD-code *MUSIC* [13, 14], for various pipework / bend configurations. Depending on the installation conditions of the USM, the flow velocity profile will change. The following installation conditions have been used in the present study of CFD-calculated flow profiles:

- USM installed in long straight pipe, for various Reynolds numbers, see Fig. 3,
- USM installed 10D downstream a single 90° bend, see Fig. 4,
- USM installed 10D downstream a double 90° bend out of plane, see Fig. 4.

The calculated axial and transversal flow velocity profiles have been processed further using CMR's uncertainty program for USMs, *GARUSO*, by use of 3-dimensional cubic spline interpolation of the 3-dimensional flow velocity data. In this way, the axial and transversal flow velocity profiles over the acoustic paths are calculated from the profiles over the pipe cross section. As an example, the flow velocity profiles (axial and transversal) have been calculated for

an acoustic path configuration which is relevant for a commercial USM for gas. However, the specific path configuration used is not very important for the results of the study.
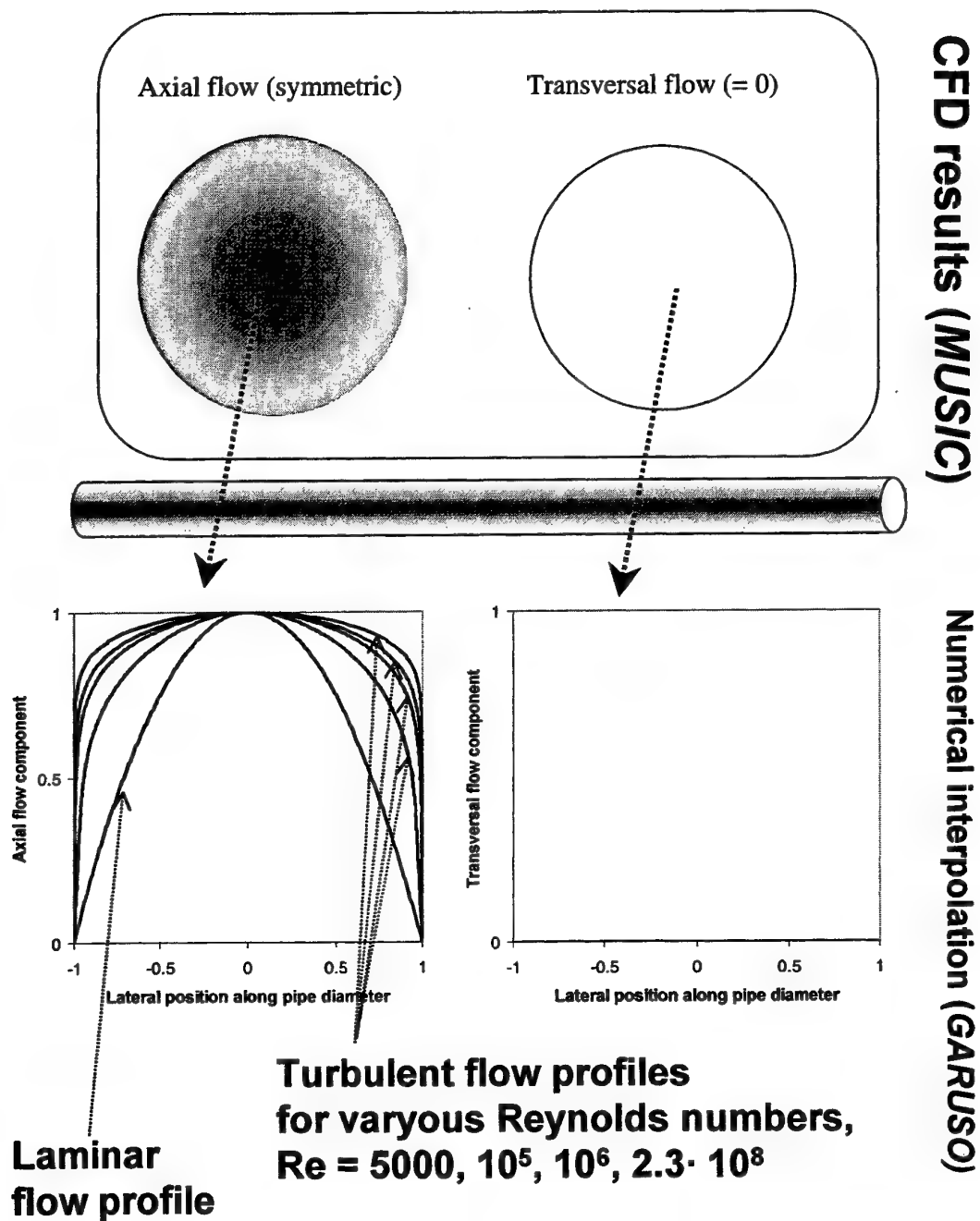

Fig. 3. CFD-calculated flow velocity profiles for flow through a straight pipe at various Reynolds numbers. Based on these CFD data, the flow velocity profile over a centre path in a USM has been calculated by a 3-dimensional cubic spline interpolation, using the *GARUSO* USM uncertainty model and simulator [11, 9, 15].

Fig. 4. CFD-calculated flow velocity profiles downstream a single 90° bend, and a double 90° bend out of plane. Based on these CFD data, the flow velocity profiles over four acoustic paths of relevance in a USM are calculated by a 3-dimensional cubic spline interpolation, using the *GARUSO* USM uncertainty model and si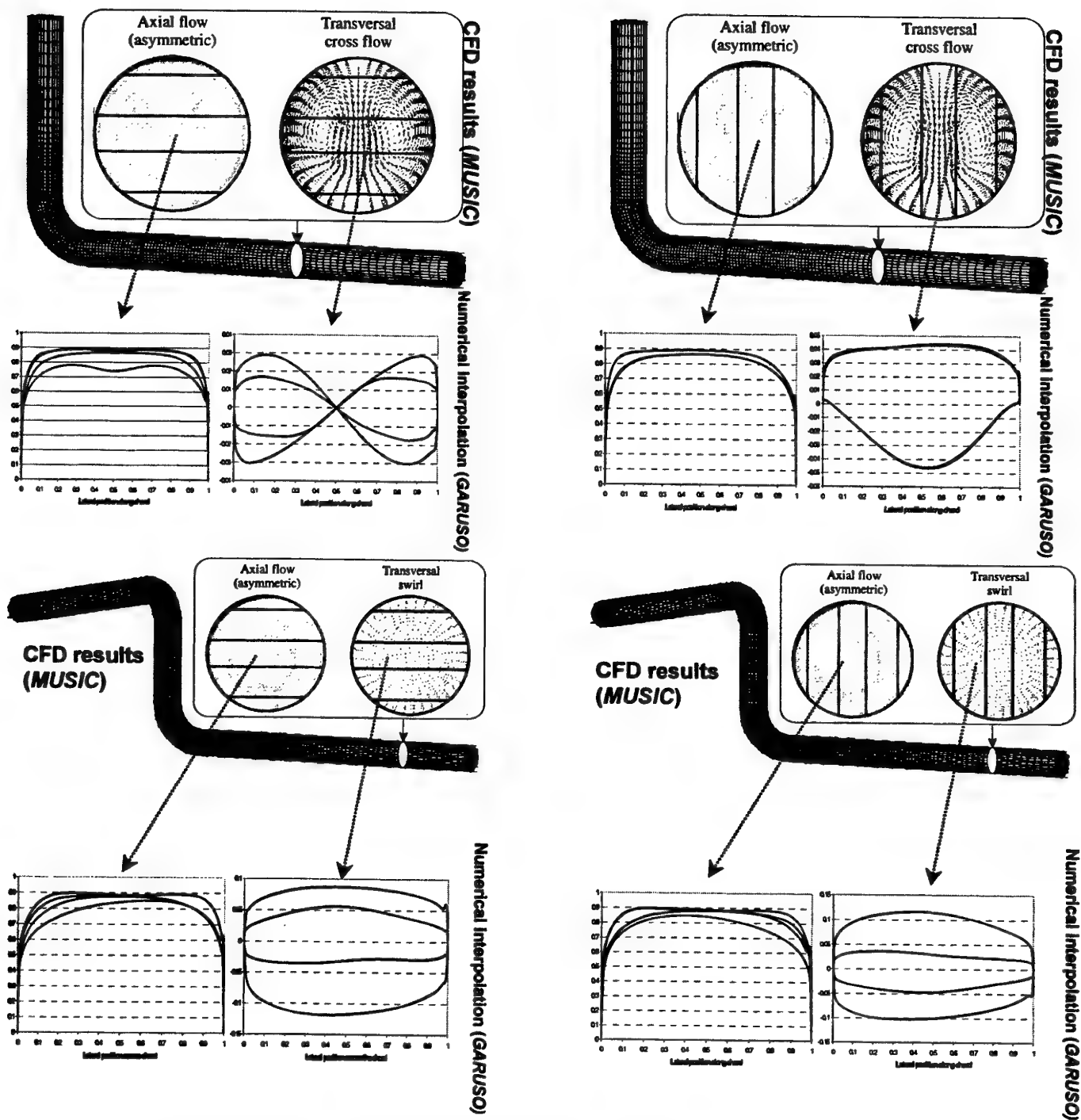mulator [11, 9, 15]. For each bend configuration, two orientations of the USM relative to the pipework are shown ("horizontal" and "vertical" chords). For each orientation and bend type, axial (left) and transversal (right) path profiles are shown.

For flow in a straight pipe, Fig. 3 shows the 3-dimensional CFD calculated profiles, and the flow velocity profile over an acoustic path through the centre of the pipe. In such flow, the transversal flow velocity will vanish, and the axial flow velocity is symmetric. The well-known dependency of the profile flatness on the Reynolds number, which is demonstrated in the figure, means that a variety of different flow profiles have to be taken into account in the discussion of flow profile effects on transit times, flow velocity and sound velocity, even for the "simple" case of a straight pipe.

For USM installation 10D downstream a single 90° bend, and a double 90° bend out of plane, Fig. 4 shows the 3-dimensional CFD calculated profiles, and the flow velocity profile over four acoustic paths of relevance in the USM referred to above. Path profiles for two orientations of the USM relative to the pipework are shown. In this case, both axial (left) and transversal (right) flow profiles over the paths have been calculated. It can be seen that the axial flow velocity profiles over the acoustic paths are asymmetric at some of the paths. The spread of transversal flow velocity component over the various paths is larger than for the axial flow velocity profiles. Here, a sinusoidal profile is seen in some cases, and in other cases, the profile is more similar to the axial flow profiles.

In Section 5, these results are used to derive typical and reasonable representative analytical path profiles (axial and transversal) which are used as input to the numerical ray model discussed in Section 4.

4. Ray theory model for sound propagation in pipe flow

A ray theory model has been derived, enabling calculation of the transit time along acoustic path no. i, $i = 1, ..., N$. In this theory, non-uniform axial and transversal flow velocity components can be accounted for, and thus the effect of non-uniform flow profiles on the transit times can be studied. The model is a further development of earlier work by the authors, cf. [16, 11].

The model is based on the general ray tracing equations as given by Pierce [17]:

$$\frac{d\underline{s}}{dt} = -\underline{s} \cdot \nabla \underline{v} - \underline{s} \times \nabla \times \underline{v} - \frac{1 - \underline{v} \cdot \underline{s}}{c} \nabla c , \qquad (14)$$

$$\frac{d\underline{x}}{dt} = \underline{v} + \frac{c^2 \underline{s}}{1 - \underline{v} \cdot \underline{s}} , \qquad (15)$$

where $\underline{s}$ is the wave slowness vector, t is the time, $\underline{x}(t)$ describes the ray trajectory, and $\underline{v}(\underline{x}) = (v_x(x,y,z), v_y(x,y,z), v_z(x,y,z))$ is the flow velocity vector. In addition to the ray approximation, which is basically a high-frequency approximation where diffraction effects are neglected, the following assumptions are made (cf. Fig. 5):

- Constant velocity of sound, c,
- 2-dimensional flow: $v_y = 0$,
- v_x and v_z are independent of x and y: $v_x = v_x(z)$, $v_z = v_z(z)$.
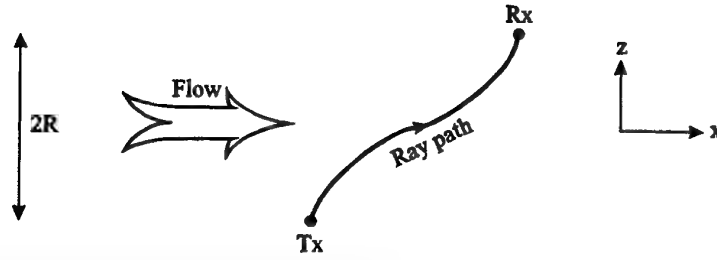
Fig. 5. Principle sketch of the ray path from the transmitting transducer (Tx) to the receiving transducer (Rx), for downstream propagation in acoustic path no. i.

Eqs. (14) and (15) then reduce to the set of equations

$$\frac{ds_x}{dt} = 0$$

$$\frac{ds_z}{dt} = -s_x \frac{\partial v_x}{\partial z} - s_z \frac{\partial v_z}{\partial z}$$

$$\frac{dx}{dt} = v_x(z) + \frac{c^2 s_x}{1 - v_x(z)s_x - v_z(z)s_z}$$

$$\frac{dz}{dt} = v_z(z) + \frac{c^2 s_z}{1 - v_x(z)s_x - v_z(z)s_z}.$$

(16)

In order to solve Eq. (16), initial conditions are specified at $t = 0$. For downstream propagation, these initial conditions are, for $x = 0$ and $z = -R$,

$$s_x = \frac{\cos \varphi}{c + v_x(-R)\cos\varphi + v_z(-R)\sin\varphi},$$

$$s_z = \frac{\sin \varphi}{c + v_x(-R)\cos\varphi + v_z(-R)\sin\varphi}.$$

(17)

Eq. (16), with initial conditions given by Eq. (17), has been solved using a fourth order Runge Kutta method. Analytical expressions for v_x and v_z (axial and transversal flow profiles, respectively) have been derived and used, cf. Section 5. An iteration procedure for φ based on Newton's method has been used to ensure that the ray ends at the specified receiver point.

The simulation of the upstream sound propagation is similar to the downstream propagation, with modified initial conditions (expressions not given here).

It may be noted that Eqs. (16)-(17) could have been obtained also if Lighthill's [18] set of basic ray theory equations were used instead of Eqs.(14)-(15). Note that the present solution gives only ray transit times, not the ray amplitude.

5. Results using the ray theory model

Based on the CFD-calculated axial and transversal flow profiles for straight pipes and pipes with bends, discussed in Section 3, typical but simplified analytical axial and transversal flow profiles have been selected for use in the numerical ray simulations. These flow profiles are analytical simplifications of the CFD calculated flow profiles discussed in Section 3. The following analytical flow profiles have been used:

Axial flow profiles:

- Symmetric parabolic flow profile (Laminar flow, Re < 1000).
- Symmetric turbulent flow profile (Turbulent flow, Re > 3000).
- Asymmetric, turbulent flow profile.
- Uniform flow profile, Re = ∞.

Transversal flow profiles:

- 0 % uniform profile (= 0).
- 10 % uniform profile, selected for comparison between simple and more "real" flow velocity profiles. (The transversal flow velocity is 10 % of the average axial flow velocity).
- 10 % symmetric flow profile (of relevance in cross flow and swirl situations).
- Sinusoidal flow profile (of relevance in cross flow situations).

The selected axial and transversal flow velocity profiles are shown in Fig. 6.
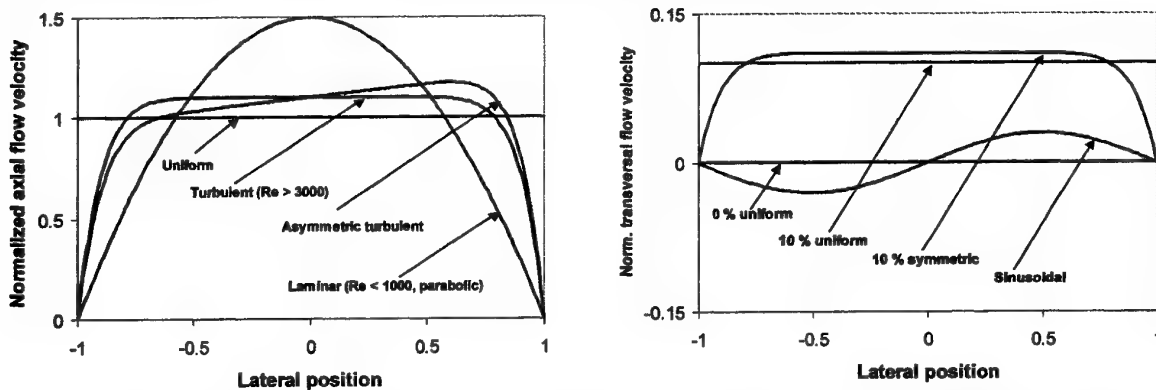
Fig. 6. The selected axial (left) and transversal (right) flow velocity profiles used in the ray theory simulations. The axial flow velocity profiles are scaled to have average flow velocity of 1, and the transversal flow velocity is scaled to the average axial flow velocity.

The following acoustic path parameters have been used in the simulations:

- Pipe diameter: $D = 0.2$ m ($\approx 8"$).
- Velocity of sound: $c = 400$ m/s.
- Inclination angle: $\phi = 45°$.

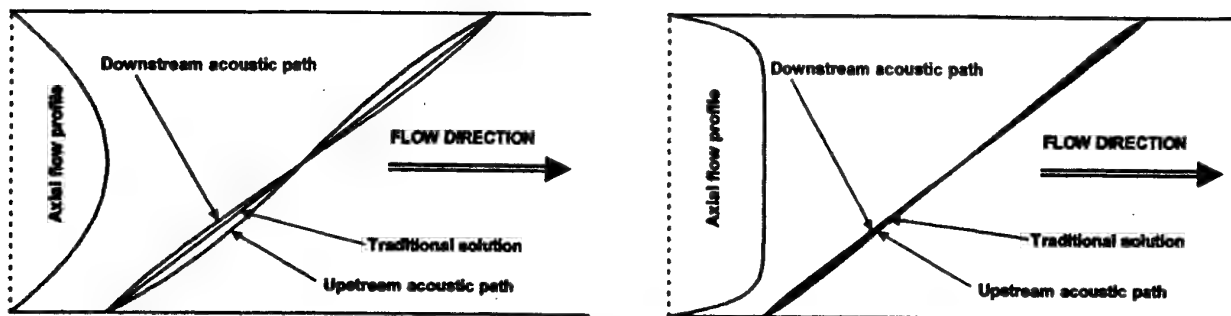Fig. 7   Calculated acoustic ray paths for upstream and downstream propagation, for two types of axial flow velocity profiles. Here, $\phi = 45°$, $c = 400$ m/s, $D = 20$ cm, and $v_x = 50$ m/s. The deviation of the ray paths from a straight line is caused by the non-uniformity of the axial flow velocity profile. Left: Laminar (parabolic) axial flow profile (Re < 1000). Right: Turbulent axial flow profile (Re > 3000, typically).
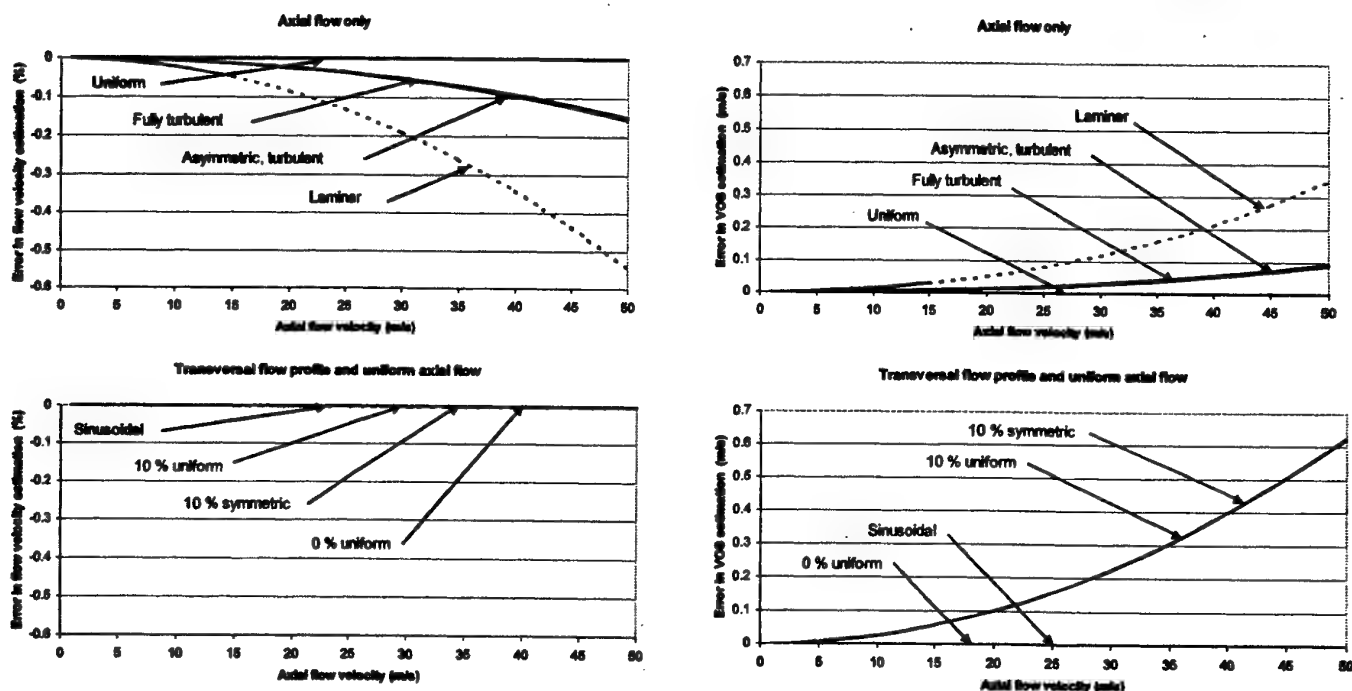

Fig. 8   The effect of non-uniform flow velocity profiles on the estimate of the average flow velocity over the acoustic path (left) and the velocity of sound (right). In the two upper figures, the transversal flow velocity component is zero and the effect of various axial flow velocity profiles is studied. In the two bottom figures, the axial flow velocity profile is uniform and the effects of various transversal flow velocity profiles are studied.

If the axial flow velocity profile is uniform, the ray path between the transmitter and the receiver will be the straight line. Non-uniformity in the axial flow velocity profile will cause the ray path to deviate from this straight line. In Fig. 7, the ray paths are shown for a flow velocity of 50 m/s, for a laminar (parabolic) axial flow profile (left) and a turbulent flow profile (right). Transversal flow velocities are not taken into account in Fig. 7. In the case of the laminar flow velocity profile, the deviation of the ray path from the straight line is larger than for the turbulent flow

94

velocity profile. This is because the turbulent flow velocity profile is closer to a uniform flow profile (which gives a straight line) than the laminar profile.

The deviation of the ray path from a straight line will also influence on the upstream and downstream transit times of the path. This will again affect the flow velocity and sound velocity measured over the acoustic path, as shown in Fig. 8. The figure shows the deviation from Eq. (10) (left part) and Eq. (8) (right part) (which are used in flow meters today), when the transit times are calculated by ray theory using the non-uniform flow velocity profiles as input.

In the upper left part of Fig. 8, the deviation is shown for three different and purely axial flow profiles (no transversal flow present), for flow velocities up to 50 m/s. Today, multipath USMs for gas typically operate up to velocities in the range 30-40 m/s. This upper limit is continuously being pushed upwards, driven by market needs. It can be seen in the figure that the turbulent flow velocity profiles studied here may give a systematic deviation of about 0.1 % for flow velocities around 40 m/s. This means that the effect is of relevance when the total uncertainty of the meter should be around 0.5-0.7 %. The parabolic profile gives larger deviation to the uniform flow profile solution. However, the parabolic flow velocity profile is of most relevance at liquid flow metering of low flow velocities. Therefore, this deviation curve has been dotted for high flow velocities.

In the lower left part of Fig. 8, the effects of transversal flow velocity profiles are shown. In this case, the axial flow velocity profile is uniform, so that the effect of the transversal flow profiles can be studied separately. The flow velocity calculated from the transit times is compared to $\overline{v}_i = \overline{v}_{i,x} + \tan\phi_i \overline{v}_{i,z}$ which is obtained for uniform axial and transversal flow velocity profiles, cf. Eq. (10). It can then be seen that there are no significant effect of the non-uniformity of the transversal flow profile, for the selected flow profiles. This means that formulas assuming uniform transversal flow velocity profiles seem to be applicable also for typical flow velocity profiles in ultrasonic flow metering.

On the two right parts of Fig. 8, the flow profile effect on the estimated velocity of sound is calculated. In the upper right figure, transversal flow velocity components are set to zero, and therefore, the effect of varying axial flow velocity profiles are studied isolated. It can be seen that the selected turbulent flow velocity profile can give an error in the velocity of sound of up to 0.1 m/s for high flow velocities. An error of this magnitude is significant when applying the velocity of sound as input to density or calorific value estimation algorithms [10].

The lower right part of Fig. 8 shows the influence of transversal flow velocity components on the sound velocity. The axial flow velocity component is here set to uniform in order to be able to study the effect of transversal flow velocity components isolated. It can be seen that the appearance of a 10 % transversal flow velocity component (relative to the axial flow velocity component) will give an error in the estimate of the velocity of sound of around 0.5 m/s or more for large flow velocities. This effect can be described by an analytical formula (not shown here). There is not observed significant differences in the error of the sound velocity estimate from *non-uniform* transversal flow velocity profiles, relative to the error of the sound velocity estimate due to the *uniform* transversal flow velocity profile, for the same average transversal flow velocity over the acoustic path.

6. Conclusions and future perspectives

A ray theory model has been developed and used to study the accuracy of the traditional expressions in current use for measurement of the average flow velocity and sound velocity at each acoustic path in an ultrasonic flow meter (USM). The ray tracing method has in addition the potential of improving these methods in current use.

With respect to axial flow velocity profiles, the effects of non-uniformity in such profiles are shown to be relatively small for low flow velocities. In such applications, the traditional USM expressions for flow velocity and sound velocity, Eqs. (10) and (8), respectively, should be sufficient. However, at higher flow velocities, typically 30 m/s and higher (Mach number > 0.08), the results indicate that the axial flow profile effects may be more significant, giving a systematic effect.

With respect to transversal flow velocity profiles, no significant effects of non-uniformity of such profiles have been found. Transversal flow velocity profiles may then be treated as being uniform. For this simplified case, improved expressions for the flow velocity and the velocity of sound (relative to the traditional expressions) have been derived (not given here).

Further work in this field should include a more extensive investigation with respect to flow velocity profiles. For instance, CFD-calculated flow profiles should be used directly into the ray theory model, as an improvement relative to the analytical profiles used here. The acoustic propagation model should preferably be extended to a 3-dimensional description of flow velocity (and not 2-dimensional as in the present work). Probably more important: - the flow profile effects in straight pipes should be analysed as a function of Reynolds number (and not solely as a function of flow velocity as made here, cf. Fig. 8).

The ray tracing approach used here is restricted, due to the high-frequency approximation inherent in that methodology (cf. Section 4), giving an infinitely thin acoustic ray, and no description of diffraction and beam effects. To fully evaluate the systematic transit time effects discussed here, and other systematic effects (cf. e.g. [9, 15]), a more comprehensive analysis based on wave theory will be needed, accounting for acoustic diffraction effects, finite beam interaction with the flow, etc.

Acknowledgements

References

[1]   "The Daniel SeniorSonic gas flow meter", Brochure, Daniel Flow Products, USA (2000).

[2]   "MPU 1200 ultrasonic gas flow meter", Brochure, Kongsberg Offshore AS, Norway (2000).

[3]   "Ultrasonic gas flow meters", Brochure, Instromet International N.V., Belgium (2000).

[4]   "Regulations relating to fiscal measurement of oil and gas etc.", Norwegian Petroleum Directorate, Stavanger, Norway (January 20, 1997).

[5]   "Measurement of gas by multipath ultrasonic meters". Transmission Measurement Committee, Report no. 9, American Gas Association (A.G.A.) (June 1998).

[6]   "Measurement of fluid flow in closed conduits- Methods using transit time ultrasonic flowmeters". ISO Technical Report ISO/TR 12765:1997, Genéve, Switzerland (1997).

[7]   **Boer, A. H.:** "Testresults Krohne 8" ultrasonic flowmeter", Proc. of the North Sea Flow Measurement Workshop 1997, Kristiansand, Norway, 27-30 October 1997.

[8]   **Folkestad, T.:**, "Proving a fiscal 5-path ultrasonic liquid meter with a small volume ball prover. Can it be done?", Proc. of the 17th North Sea Flow Measurement Workshop, Oslo, Norway, 25-28 October 1999.

[9]   **Lunde, P., Frøysa, K.-E. and Vestrheim, M. (editors):** *GERG project on ultrasonic gas flow meters, Phase II.* GERG Technical Monograph TM 11 2000, Groupe Européen de Recherches Gazières (VDI Verlag, Düsseldorf, 2000).

[10]   **Lunde, P., Frøysa, K.-E., Fossdal, J. B. and Heistad, T.:** "Functional enhancements within ultrasonic gas flow measurement", Proc. of the 17th North Sea Flow Measurement Workshop, Oslo, Norway, 25-28 October 1999.

[11]   **Lunde, P., Frøysa, K.-E. and Vestrheim, M.:** "*GARUSO* - Version 1.0. Uncertainty model for multipath ultrasonic transit time gas flow meters". CMR Report No. CMR-97-F10014, Christian Michelsen Research AS, Bergen (August 1997).

[12]   **McCartney, M. L. Mudd, C. P. and Livengood, R. D.:** "A corrected ray theory for acoustic velocimetry". *J. Acoust. Soc. Am.* **65**, 50-55 (1979).

[13]   **Hallanger, A. and Johnsen, F.:** "CFD simulations of turbulent gas flow in pipes with bends", CMR Report no. CMR-99-F10085, Christian Michelsen Research AS, Bergen (December 1999). (Confidential.)

[14]   **Hallanger, A., Frøysa, K.-E. and Lunde, P.:** "CFD simulations and installation effects for ultrasonic flow meters in pipes with bends", Paper to be presented at the conference *MekIT'01 - Nasjonalt seminar i bergningsorientert mekanikk*, Trondheim, 3-4 May 2001.

[15]   **Lunde, P., Frøysa, K.-E. and Vestrheim, M.:** "Challenges for improved accuracy and traceability in ultrasonic fiscal flow metering", Proc. of the 18th North Sea Flow Measurement Workshop, Gleneagles, Scotland, 24-27 October 2000.

[16]   **Lygre, A., Lunde, P., Bø, R. and Vestrheim, M.:** "High-precision ultrasonic gas flowmeter. Sensitivity study. Volumes I and II," CMI report 871429-1, Christian Michelsen Research, Bergen (1988) (Confidential).

[17]   **Pierce, A.D.:** Acoustics. An Introduction to Its Physical Principles and Applications (McGraw-Hill, New York, 1981).

[18]   **Lighthill, J.:** *Waves in Fluids* (Cambridge University Press, 1978).

[19]   **Frøysa, K.-E., Furset, H. and Baker, A.:** "Density and ultrasonic velocity calculations for natural gas", CMR report CMR-98-F1002, Christian Michelsen Research, Bergen (1998) (Confidential).

Leaky-mode and wavenumber-integration representations of grazing-ray diffraction

Sven Ivansson and Judith Bishop

Swedish Defence Research Agency (FOI), SE-17290 Stockholm, Sweden and
Naval Undersea Warfare Center (NUWC), Newport, RI 02841-1708, USA
Email: sveni@foi.se and bishopjl@npt.nuwc.navy.mil

There are many instances in acoustics, seismics and electromagnetics when it is useful to represent wave fields, including diffraction, in terms of traveling-wave or directional expansions. Field components with a well defined angle-time arrival structure are produced in this way. For definiteness, we consider mono-frequency acoustic wave propagation with time dependence $e^{-i\omega t}$, ω being angular frequency. Denoting horizontal slowness by p,

$$P(r,z) = \frac{1}{2} \int_{-\infty}^{\infty} G(z;p) \mathrm{H}_0^{(1)}(\omega pr) \omega^2 p \, dp \tag{1}$$

synthetizes the pressure field at range r and depth z in a laterally homogeneous medium from its wavenumber components [1]. By introducing a specification depth where the medium is artificially considered to be locally homogeneous, cf. [2, ch. 6] and [3, sec. 1], we may introduce p-dependent reflection coefficients γ_A and γ_B for upward and downward going plane waves, respectively. The Green's function $G(z)$ in (1) can be written

$$G(z) = (1 - \gamma_A \gamma_B)^{-1} \sum_{i=1}^{4} G_{i,0}(z) = \sum_{i=1}^{4} \sum_{j=0}^{\infty} G_{i,j}(z) \tag{2}$$

where the $G_{i,j}(z) = (\gamma_A \gamma_B)^j G_{i,0}(z)$ are component Green's functions.

A standing-wave (normal mode) expansion appears as the residue contributions from the p such that $\gamma_A \gamma_B = 1$ (e.g., [3]), whereas a traveling-wave expansion [4] appears by applying the geometric series for $(1 - \gamma_A \gamma_B)^{-1}$ as indicated. The index i is intended to separate upgoing and downgoing waves at source as well as receiver, whereas the index j is thought of as a cycle number. The implied decomposition of $P(r,z)$ becomes

$$P(r,z) = \sum_{i=1}^{4} \sum_{j=0}^{\infty} P_{i,j}(r,z) \quad , \quad P_{i,j}(r,z) = \frac{1}{2} \int_{-\infty}^{\infty} G_{i,j}(z;p) \mathrm{H}_0^{(1)}(\omega pr) \omega^2 p \, dp . \tag{3}$$

It is tempting to regard the $P_{i,j}$ as 'generalized rays' and consider the decomposition (3) as an exact extension of ray theory to finite frequencies. The traveling-wave expansion has typically been utilized in

this way (e.g., [5]), and this works well in the propagating regime for which the WKBJ approximation [6, Box 9.3] in conjunction with the stationary-phase and related approximations [7, Appendix] indicate dominant contributions from the neighborhoods of certain well-defined p values. Cf. classical ray theory with Airy-function corrections at smooth caustics [8, sec. 9-4].

Here, we consider the traveling-wave expansion for modeling low-level creeping-wave diffraction fields, which turns out to be much more delicate. In [9], we elucidated the importance of the evanescent regime of wavenumbers in this context. It turns out, however, that the integrals (over p) that appear in (3) do not in general converge at infinity. Hence, the decomposition is not even well defined!

As it stands, the decomposition (3) is thus not useful for modeling grazing-ray diffraction beyond boundary-produced caustics. For single grazing-ray diffraction, with only one interaction with the boundary, Pierce [8, sec. 9-5] has described how the shadow-zone field can be represented as a residues series whose leading term can be interpreted physically as ray shedding by a creeping wave. Application of this residues series to aeroacoustics can be found in [10], for example.

In [11] and [12], and references therein, we proposed recombinant (or reduced) traveling-wave expansions which can be used for exact modeling of single as well as multiple grazing-ray diffraction. The convergence criteria are relaxed, allowing specification-depth location at the point of minimum sound speed in the medium, by which trapped modes are avoided. Physically, ray contributions arise from points p of stationary phase while ray shedding in the shadow zone arises from leaky modes.

We limit ourselves to an example with a sound channel according to Fig. 1a with source and receiver depths at 10 m and 50 m, respectively. The subbottom below 80 m is a homogeneous fluid half-space with density 2 kg/dm^3, velocity 2.0 km/s and absorption 0.7 dB/wavelength. Transmission loss curves (re 1 m) for component fields $P_{12,j}$ are shown in Fig. 1b. The recombinant-type quantity $P_{12,j}$ agrees with the sum of $P_{1,j}$ and $P_{2,j}$ whenever the latter are well defined.
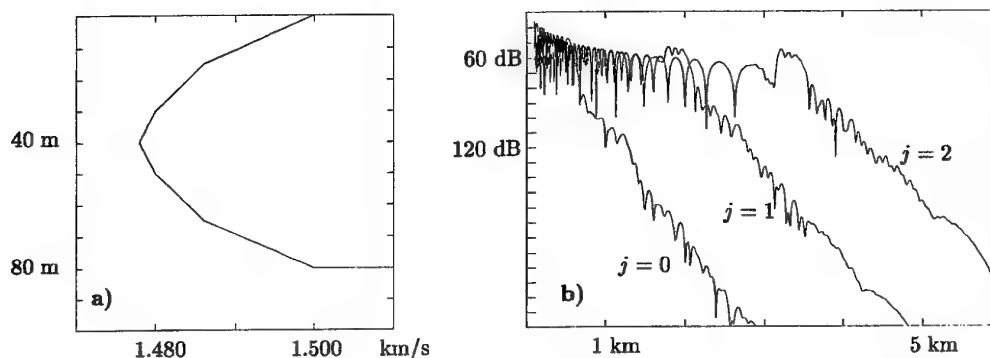

Figure 1: **a)** Sound-speed profile. **b)** Recombinant-type field components $P_{12,j}$ at 3 kHz. •

Just as for the downward refracting example studied in [12], the recombinant-type field decomposition does a good job of isolating physical ray energy to the term with the appropriate cycle number j. The grazing rays that start upwards from the source and reach the receiver from above (type $i=2$ according to [5]) get the range of 0.613, 2.119, and 3.624 km for the cycle numbers $j=0$, 1, and 2, respectively. These ranges are clearly related to the shadow-zone ranges in Fig. 1b, beyond which the pertinent $P_{12,j}$ components decrease steadily.

Individual leaky-mode contributions for our sound-channel medium example are studied in Fig. 2, and also in Fig. 3a. In this case, it is mode 21 (as numbered from the right in Fig. 2a) that is closest to the slowness 1/1.5 s/km of the surface-grazing ray, but the imaginary mode slowness parts have an increasing trend already from mode 1. Although mode 1 must dominate the very weak $P_{12,0}$ field at very long ranges, modes close to the surface-grazing ray slowness will indeed be important at

moderate ranges. In Fig. 2b, mode 20 provides the largest contribution at $r = 0.3$ km, whereas mode 17 dominates at $r = 0.6, 0.9$, and 1.2 km. The results in Fig. 3a confirm the suitability, for the purpose of computational efficiency, of classical ray theory at close ranges and representation with a limited number of leaky modes at a shadow boundary and beyond.
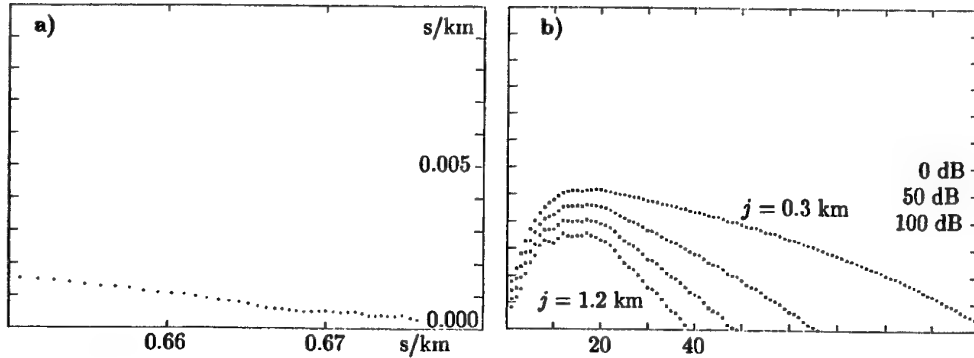

Figure 2: **a)** Mode slownesses in the complex slowness plane relevant to a leaky-mode representation of the $P_{12,0}$ field in Fig. 1b. **b)** Contributions of individual modes to the corresponding $P_{12,0}$ field at four different ranges r: 0.3, 0.6, 0.9, and 1.2 km. The horizontal axes are for mode number, according to decreasing real part of horizontal slowness. •

For components with cycle number $j > 1$, and also some with $j = 1$, the additional singularities from γ_A and γ_B cause higher-order poles. The corresponding residues will involve higher-order derivatives that do not seem to be easily computed. To be able to conveniently handle all field components under these circumstances, those with cycle number $j \geq 1$ in particular, we may use wavenumber integration along short paths in the complex p plane to capture the crucial leaky modes.

For our sound-channel example, the corresponding $P_{12,j}$ results are shown in Fig. 3b-d, along with exact results and classical ray-theory results. Again, it is apparent that ray theory is useful at close ranges, whereas leaky-mode Green's function expansion is appropriate at shadow boundaries and beyond.

References

[1] F. Jensen, W. Kuperman, M. Porter, and H. Schmidt. Computational Ocean Acoustics. AIP Press, New York (1994).

[2] B.L.N. Kennett. Seismic Wave Propagation in Stratified Media. Cambridge University Press, Cambridge (1983).

[3] E.K. Westwood, C.T. Tindle, and N.R. Chapman. A normal mode model for acousto-elastic ocean environments. J. Acoust. Soc. Am. 100, 3631-3645 (1996).

[4] D.V. Batorsky and L.B. Felsen. Ray-optical calculation of modes excited by sources and scatterers in a weakly inhomogeneous duct. Radio Science 6, 911-923 (1971).

[5] H. Weinberg. Application of ray theory to acoustic propagation in horizontally stratified oceans. J. Acoust. Soc. Am. 58, 97-109 (1975).

[6] K. Aki and P. Richards. Quantitative Seismology. Freeman, San Francisco (1980).

[7] C.T. Tindle. Ray calculations with beam displacement. J. Acoust. Soc. Am. 73, 1581-1586 (1983).

[8] A.D. Pierce. Acoustics. AIP Press, New York (1994).

[9] J.L. Bishop and S. Ivansson. Multipath field representation for seabed parameter extraction using backscatter data from shadow zones. In N.G. Pace, E. Pouliquen, O. Bergem and A.P. Lyons (ed.): High Frequency Acoustics in Shallow Water. SACLANTCEN Conference Proceedings CP-45, La Spezia 39-47 (1997). *Note*: Replace in Fig. 11 350 by 350/ln(10)≈152.0 and in Fig. 12 650 by 650/ln(10)≈282.3.

[10] S.J. Franke, R. Raspet, and C.H. Liu. Numerical predictions of atmospheric sound-pressure levels in shadow zones. J. Acoust. Soc. Am. 83, 816-820 (1988).

[11] S. Ivansson and J. Bishop. Extraction of traveling-wave field components by Green's function expansion. In U.R. Kristiansen (ed.): Proceedings of the 23rd Scandinavian Symposium on Physical Acoustics, Ustaoset 24-26 (2000).

[12] S. Ivansson and J. Bishop. Single and multiple grazing-ray diffraction as derived by Green's function expansion. In M.E. Zakharia (ed.): Proceedings of the fifth European Conference on Underwater Acoustics ECUA 2000, Lyon 21-26 (2000).
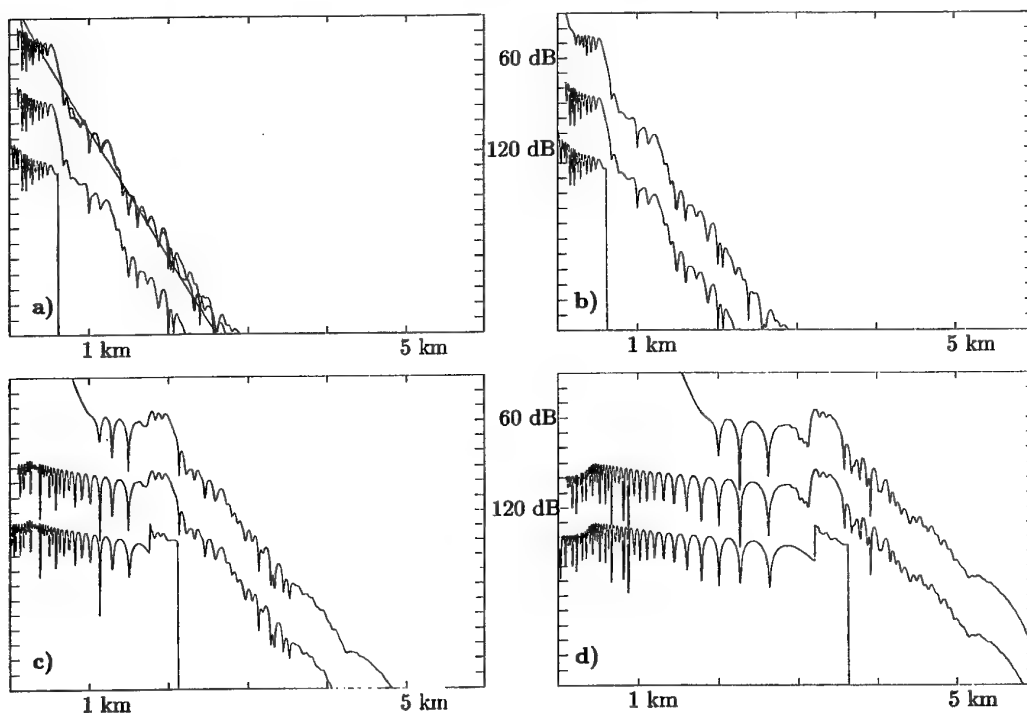
Figure 3: **a)** Transmission loss (re 1 m) for $P_{12,0}$ as in Fig. 1b, but only including certain leaky modes from Fig. 2. Three mode curves are given, with increasingly improved agreement to the complete $P_{12,0}$ field. They were obtained as coherent sums of the following mode fields: mode 17, modes 12-21, modes 1-100 in Fig. 2b. Two additional curves are given: the 'exact' result from Fig. 1b (displaced 40 dB downwards for clarity) and the classical ray-theory result (displaced 80 dB downwards). **b)-d)** Transmission loss (re 1 m) for $P_{12,0}$ (upper right), $P_{12,1}$ (lower left), $P_{12,2}$ (lower right), as obtained by wavenumber integration along a short path to enclose the horizontal slownesses of the crucial leaky modes. The corresponding 'exact' result from Fig. 1b (displaced 40 dB downwards) and the classical ray-theory result (displaced 80 dB downwards) are also shown in each case. ●

Practical applications of resonance vibration of liquid-filled cylinders

I.Bjørnø and L. Bjørnø

UltraTech Holding
Stendiget 19
Dk-2630 Tåstrup
Denmark

INTRODUCTION.

The aim of the present work is to demonstrate the practical applications of a high-power ultrasound transducers mounted on a filtering spiral module. This construction has been tested in a vine production plant for preventing the blocking of microfilters by organic materials and for increasing the flow rate through the filters and the time between the filter cleanings. A numerical, FE and BE based model for calculation of the resonance vibrations of a liquid filled spiral module formed the basis for the design of the transducer attachment construction. During the laboratory experiments the resonance response of the filter module was measured carefully and compared with theoretical predictions. The properties of the filtering spiral module and the results of the tests are discussed in details. This work was financed through the EU Project WAMBIO PL96-3257 (FAIR Programme).

BACKGROUND FOR THE RESEARCH.

In vine filtering processes a spiral filtering module is commonly used. In order to find the optimum solution for design of the attachment of ultrasound transducers to the filtering module careful choice of the attachment point should be made. The aim of such a construction is to excite the natural vibration modes of the filter housing (which is shaped as a cylinder with closed ends) as a whole, where flexural vibrations can travel along the cylindrical tube.

THEORETICAL MODEL

In our case the simplest model for the spiral wound filter is the cylindrical tube with two closed ends. In agreement with the technical specification the length of the steel tube is 960mm, with a inner diameter of 104 mm and a wall thickness of h=2,5 mm. Tube mean radius is 53,25 mm. Young modulus E of the tube material is $20 \cdot 10^{10}$ N/m^2; the shear modulus G is $7.69 \cdot 10^{10}$ N/m^2 and the Poisson's ratio $\nu = 0.245$. Figure 1 shows a sketch of the flexural waves travelling along the cylindrical tube.
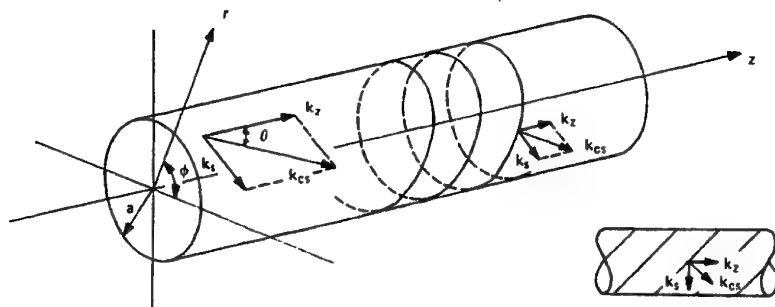
Figure 1. Flexural wave propagation on a thin-walled cylindrical tube.

Two important parameters for the definition of the resonance properties of the cylindrical tube are:
- The nondimentional frequency $\Omega=\omega a/c_1$, where ω is the angular frequency, a is the mean radius of the tube and c_1 is the longitudinal wave speed.
- The nondimentional thickness parameter $\beta=h/(\sqrt{12})a$

The first parameter indicates the frequency at which an antisymmetric resonance mode can occur (n is the mode number)

If we suppose, that the thickness of the tube wall is small enough compared to the mean radius, (i.e. h « a), then the frequency equation for the antisymmetric resonance modes of the cylindrical tube will be:

$$\Omega^2_n=\beta^2 n^4[1-0.5\ (1/(1-\nu)\{(4-\nu)/n^2-(2+\nu)/\ n^4\})].$$

Simple calculations will give us all resonance frequencies corresponding to the different mode numbers.

For   n=5 $\Omega_n=\beta\cdot 23,76=0.0751$ $\omega=8808$ and   f=1402 Hz
For   n=10 $\Omega_n=\beta\cdot 97,53=0.3082$ $\omega=36155$ and   f=5754 Hz
For   n=19   f=21223 Hz
For   n=20   f= 23525 Hz
For   n=21   f=25945 Hz
For   n=22   f=28483 Hz
For   n=23   f=31140 Hz .

Note, that our model tube is empty (if filled with water the resonance frequencies will be reduced).
If a flange is introduced (as it is in the case of a spiral filter), the resonance frequencies will be increased.

EXPERIMENTAL TESTS

From the theoretical investigations of the vibration modes of the simple model of a steel tube, it was concluded that the excitation of the steel tube as a whole (also comprising the spiral filter module) can potentially be used for obtaining the necessary high levels of ultrasound intensity inside the filter unit and that a frequency around 25-27 kHz could be used.

Experimental set-up

A 94 cm x 10 cm filter module containing a standard plastic microfilter membrane MPPS-U002 was assembled, filled with water and tested in the laboratory. A RESON standard TC 5003 transducer was used to excite the tube vibrations. An approx. 25 kHz continuous sinusoidal signal was generated by a TCE 7702 signal generator and the signal was amplified in a HVPA-01 power amplifier.

The flexural vibrations were picked up by a B&K accelerometer and monitored by a HP 54602A oscilloscope.

The accelerometer was fixed to the outside tube wall using bee wax, and a working line for transducer excitation was drawn from the accelerometer to the end of the tube.

The head part of the TC 5003 transducer had a diameter of 60 mm, while the local resonance points of the tube was expected to have a size of only 5 mm. Therefore, the ultrasonic vibrations were applied to the steel tube by turning the transducer around and by pressing the transducers bolt head vertically against the tube wall.

Registration of the tube wall vibration modes

Each local maximum response location was recorded. The schematic picture below shows the experimental set-up used during the measurement of the resonance response along the tube module with the indication of the position of the transducer and the positions of the recorded maximum of the response signals. The dimensions correspond to a working frequency of 27 KHz

Spiral filter modul
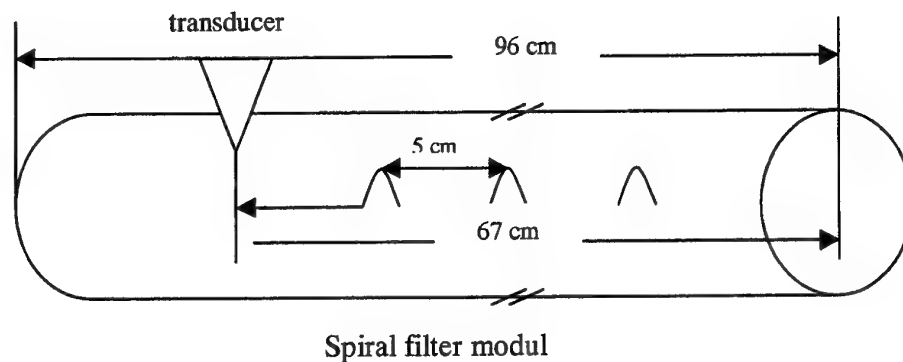
During the tests the accelerometer was fixed in five different positions on the inlet /outlet side of the tube, and the whole measurement procedure was repeated for each accelerometer position.

The procedure was repeated for 3 different frequencies: 24 kHz, 25 kHz and 27 kHz with both transducer and accelerometer operating at the opposite side of the inlet/outlet side of the tube.

DISCUSSIONS OF THE EXPERIMENTAL RESULTS AND THE CONCLUSIONS

Careful analysis of experimental data allowed us to draw several conclusions:

1. The best performance was obtained using a 27 kHz signal to excite the filtering module. The tube response signal detected by accelerometer have had a more or less periodic structure with the repetition rate of the maximum value of the response signal after every 5 cm. The amplitude level at maximum response was about the same along the whole tube, around 240-280 mV. It means that it was possible to excite the vibration mode of the full spiral filtering module by propagation of flexural wave signals along the module.

2. The tested frequency of 25 kHz shows a periodical structure for the maximum signal response in the axial direction of the tube with a repetition rate of approx. 4 cm between the maximum values. Maximum amplitude for the response signal was recorded to 140 mV (only half of the amplitude measured at 27 kHz).

3. For the 24 kHz signal no periodic behaviour was founded. A maximum response accelerometer signal of 100 mV was recorded.

4. Calculation of the resonance frequencies using the simple model for the spiral wound filter shown earlier gives the value for the eigen-frequency of the empty tube to be 28483 Hz. If we take into account that the simple model can only give an indication of the magnitude of the actual flexural wave frequency, the experimental value of the best performance frequency of 27 kHz, is very close to the theoretically predicted one. The reduction from the calculated empty tube frequency of 28.48 kHz to the measured 27 kHz for optimal operation should be expected due to the presence of liquid and filter module in the tube during the experiments.

5. Efficient transducer attachments to the spiral wound filter housing for the excitation of the flexural vibration modes of the tube wall thus leading to an ultrasonic cleaning effect on the filter module can be achieved.

6. Several technical problems should, however, be solved before a successful application of the ultrasound transducers to the cleaning of the filter module can be carried out:

    •   New construction for the attachment of the transducer to the cylindrical filter surface should be considered for maximum transfer of power to the tube wall.
    •   Optimisation of the transducer performance should be considered as an alternative as calculations have shown, that the use of lower frequencies could lead to a more efficient excitation of the tube wall vibration.
    •   Losses at high frequencies, which are about 90%, may be reduced by using low frequency transducers (fundamental frequency of about 1,5 kHz) and by improving the attachment procedure.

Sound radiation from unbaffled loudspeakers

Peter Svensson, Asbjørn Krokstad

Dept of Telecommunications, NTNU, 7491 Trondheim

Abstract

The near-field of an unbaffled loudspeaker is studied. A model employing edge diffraction is used, and this gives an analytic expression for the impulse response of a circular piston taking the direct sound and the first-order diffraction into account. Higher-order diffraction is approximated by a rest function. Results show that, as expected, an unbaffled loudspeaker element gives a less homogeneous sound field for movements along the symmetry axis than a baffled loudspeaker element does. On the other hand, the unbaffled loudspeaker also leads to a lower crosstalk between the two ears of a listening person sitting very close to the loudspeaker element than a baffled loudspeaker does.

Introduction

Loudspeakers are usually placed in baffles or enclosures in order to transform their inherent dipolar operation into a monopolar operation with its higher efficiency. For some applications, however, unbaffled loudspeakers might be used. A recently presented active noise control system for the creation of a so-called Silent Zone around a person's head, see Fig. 1 [1], uses unbaffled loudspeakers. For such applications the nearfield of the unbaffled loudspeaker must be analyzed. The purpose of this paper is to study using a model of a vibrating, free circular piston. An impulse response method using the edge diffraction concept is used for the study [2]. First, the edge diffraction impulse response method is reviewed briefly. Then the case of a piston is modelled as a superposition of point sources and numerical results are presented for this case.

Analytic edge sources

The scattering from an object with rigid, plane surfaces can be formulated as a sum of geometrical acoustics components, i.e., the direct sound and specular reflections, and edge diffraction components. Edge diffraction is caused by the waves that are scattered off the straight or curved edges of the finite surfaces and can be represented by secondary sources placed along the edges [2,3]. These sources radiate spherically in addition to a directivity function which depends on the angle of the incident wave from the point source towards the edge point (angles α and θ_S in Fig. 2), and also on the radiation angle (angles γ and θ_R in Fig. 2). The decomposition can be expressed as a line integral along the edge of the wedge so that the sound pressure IR is

$$h(t) = -\frac{cv}{2\pi}\int \delta\left(t - \frac{m-l}{c}\right)\frac{\beta}{ml}dz, \tag{1}$$

where c is the speed of sound, v is the so-called wedge index which equals π/θ_w, and m and l are the distances to and from a point z along the edge as indicated in Fig. 2. The factor β is a directivity function which has the form

$$\beta = \sum_{\pm\mp}\frac{\sin\left[v(\pi \pm \theta_S \mp \theta_R)\right]}{\cosh\left(v\cosh^{-1}\frac{1 - \sin\alpha\sin\gamma}{\cos\alpha\cos\gamma}\right) - \cos\left[v(\pi \pm \theta_S \mp \theta_R)\right]}. \tag{2}$$

The summation includes four terms, with all possible combinations of the two signs indicated in the sine and cosine factors, and with the sign combinations in the numerator and denominator being the same. It is clear that β can be interpreted as a directivity factor since it includes only the incidence angles α and θ_S, and the reradiation angles γ and θ_R. For an IR as in Eq. (1), the source signal quantity is $\rho_0 \cdot A(t)/(4\pi)$ where ρ_0 is the density of the fluid and $A(t)$ is the volume acceleration of the point source. This choice of source signal gives a free-field IR which is $h_{ff}(t) = \delta(t-R/c)/R$.

The expressions in Eqs. (1) and (2) can be extended to curved edges as long as the integration variable z is interpreted as running along the curved edge. Also, finite wedges can be handled directly by carrying out the integration over the range of z which corresponds to the finite wedge. Furthermore, the extension to higher orders

FIG. 1 Illustration of an active noise control system implementing a silent zone around a person's head [1]. The loudspeaker elements are unbaffled.
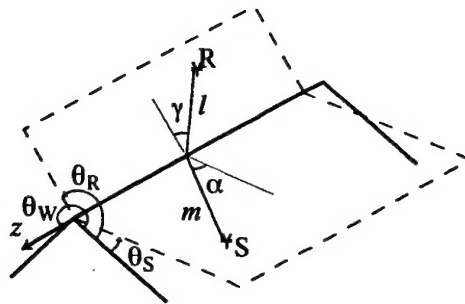
FIG. 2 Illustration of the various parameters for the diffraction from a point source S via a point along the edge of a wedge to a receiver point R. The two fictive planes created by the edge and the source and the receiver, respectively, are indicated by the dashed lines.

of edge diffraction, which might be needed to include in many situations, is relatively straightforward, see [2]. It should be noted that wedges which have one or two pressure-release planes, rather than two rigid planes, can be handled simply by changing the sign of one or more of the four terms in the sum in Eq. (2). Having access to analytical directivity functions for the secondary edge sources offers the possibility to derive analytical expressions for the edge diffraction IR if the angles in Eq. (2) can be expressed in terms of the integration variable z. This is demonstrated in the next Section for the case of a circular piston. Finally, the expression in Eq. (1) is very well suited for numerical implementation since the integrand is well behaved. Consequently, first-order diffraction can be calculated numerically for arbitrary geometries with high accuracy and very little computational effort. It should be noted that this is exactly what the so-called Wedge Assemblage (WA) method does, [4]. The WA method is based on Medwin's interpretation of the Biot-Tolstoy method, [5], and Medwin's method in [3] is, numerically, identical with the presented method for first-order diffraction but is approximate for higher-order diffraction.

The unbaffled piston

A vibrating piston can be modelled as a rigid thin disc and a continuous distribution of point sources on both sides of the scattering disc, with opposite polarity. The total sound field can then be described by an impulse response which is a sum of the direct sound IR (from the frontal side of the disc), and the edge diffraction IR:s for increasing orders. This is a special case with $v = 1/2$ and $\theta_S = 0$. For that case, illustrated in Fig. 3, the directivity function can be simplified into

$$\beta = \frac{8\cosh(v\eta)\cos\dfrac{\theta_R}{2}}{\cosh^2(v\eta) - \sin^2\dfrac{\theta_R}{2}} = \frac{8\sqrt{2}\,\cosh(v\eta)\sqrt{1 + \cos\theta_R}}{2\cosh^2(v\eta) - 1 + \cos\theta_R} \tag{3}$$

where

$$\cosh(v\eta) = \cos\frac{\alpha - \gamma}{2}\bigg/\sqrt{\cos\alpha \cdot \cos\gamma}\ . \tag{4}$$

In Eq. (3), the effect of the sources on the rear side of the disc, with opposite polarity, have been taken into account since their contribution is exactly the same as the sources on the frontal side. For a continuous distribution of sources, the edge diffraction component can be derived by integrating the contributions from all source positions,

$$h_{tot,D1}(t) = \frac{1}{S}\int_S h_{D1}(t)dS \tag{5}$$

where S is the piston's area, and $h_{D1}(t)$ is the first-order diffraction IR for each source position. If we study only on-axis receiver positions, this integral can be solved analytically and the result is

$$h_{tot,D1}(t) = -\frac{4c\sqrt{a+l}}{\pi a^2\sqrt{l}}\left\{\frac{\pi}{2}\left(1 - \sqrt{\frac{l}{a+l}}\right) - \sin^{-1}\sqrt{\frac{ct-l}{2a}} + \sqrt{\frac{l}{a+l}}\tan^{-1}\left(\sqrt{\frac{a+l}{l}}\sqrt{\frac{ct-l}{2a-ct-l}}\right)\right\}w(t), \tag{6}$$

where the receiver is at a height z, which gives $l = \sqrt{a^2 + z^2}$, a being the radius of the piston. The function $w(t)$ is a window function which is zero before the first possible arrival of sound via an edge point, and zero after the last possible arrival of sound. Between those two points in time, $w(t) = 1$.
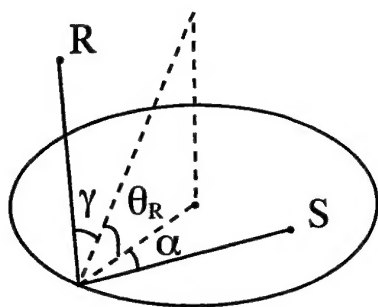
108

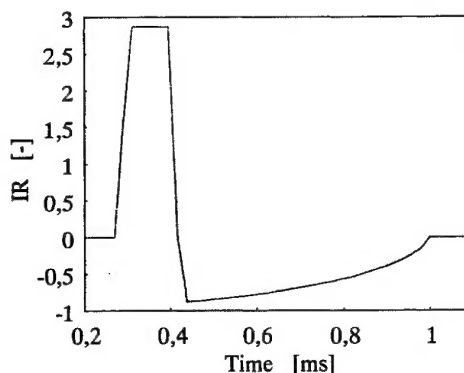FIG. 3 A circular disc with a source point S on the disc's surface and a receiver point off-axis.

FIG. 4 IR for an unbaffled piston of radius 0.1 m and a receiver on-axis (i.e., with $\gamma = 0$) at a height of 0.1 m.
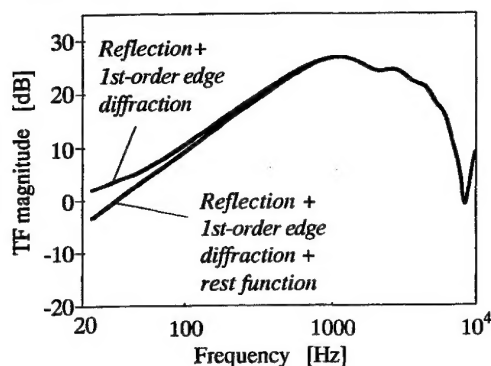

FIG. 5 The transfer function of the IR in Fig. 4, but with half the positive pulse in Fig. 4 removed.
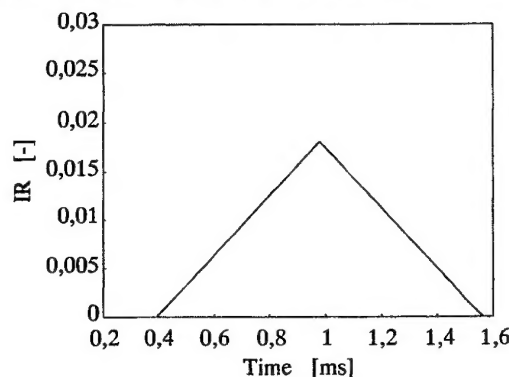

FIG. 6 The rest function, which replaces second- and higher-order diffraction.

Fig. 4 illustrates the IR which includes the direct sound of the piston, and the edge diffraction IR according to eq. (6). Second- and higher diffraction components can not be derived analytically so numerical integration is necessary. Here, a simplified approach has been chosen where the second- and higher-order diffraction is replaced by an approximate "rest function". A reasonable estimate of this rest function can be found since we know that the total impulse response from the piston must asymptotically go towards free-field radiation for very low frequencies. In Fig. 4, the first positive rectangular pulse is the baffled piston radiation, given by radiation into 2π, and thus with twice the amplitude of free-field radiation. The sum of half the first rectangular pulse, plus all orders of diffraction must then be a high-pass filter. Fig. 5 illustrates this. Stated another way, the scattering of a rigid disc must be a high-pass filter, and here we have a scattering case with a free-field radiating distribution of point source immediate close to the rigid disc. We can choose a rest function which is shaped as in Fig. 6 since this shape should match the second-order diffraction quite closely. It is clear at which times the second-order diffraction must start and stop- The area of the rest function is chosen so that the total response of reflection + first-order diffraction (eq.(6)) and the rest function is 0 at 0 Hz. This is clearly a very simplified approach but it can give very useful estimates of the transfer function also at low frequencies and uses explicit simple expressions.

Numerical examples

For an application such as in Fig.1, three aspects of the near-field are especially interesting: how homogeneous the sound field is if the listener moves the head, how strong the cross-talk is (from the nearest to the furthest ear) and how efficient an unbaffled piston is compared to a baffled piston. These points were studied in the free-field in front of the unbaffled piston, i.e., the reflecting/scattering of the head was ignored. At low frequencies this assumption is quite acceptable.

The homogeneity in front of the piston is important in an active noise control system since such a system aims at supplying an out-of-phase sound wave with a specific amplitude and phase controlled as accurately as possible. This can be accomplished only in a single point but if the sound field is homogeneous, the controlled/silent zone will be larger. Fig. 7 shows the transfer function (TF) magnitude for the frequency of 94 Hz,
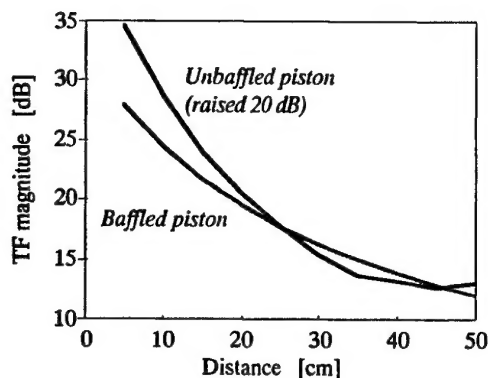
109

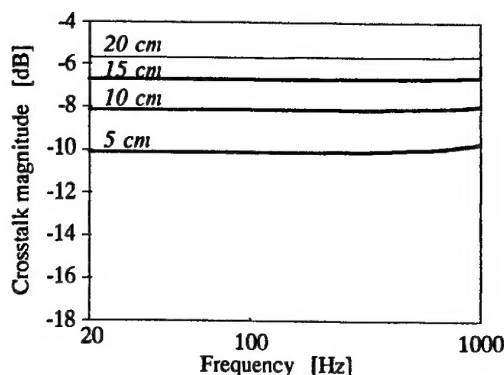FIG. 7   The TF magnitude at 94 Hz for a circular piston of 20 cm diameter with the receiver on-axis.

FIG. 8   The TF magnitude difference for a baffled piston and with two on-axis receiver positions 20 cm apart. Parameter is the distance between the piston and the closest microphone.
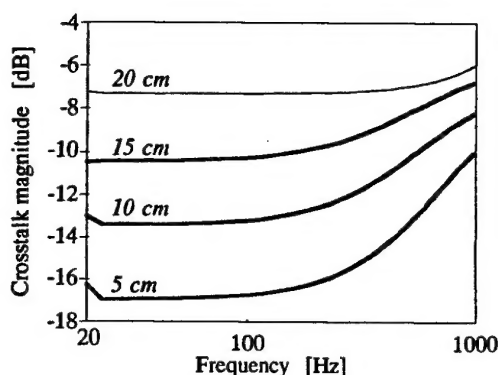

FIG. 9   Same as in Fig. 8 but for an unbaffled piston.

as function of distance from the piston, for receiver positions on-axis. Results are shown for both a baffled and an unbaffled piston. As can be seen, a baffled piston does actually give a sound field which is varying less for distances around 10-20 cm from the piston. It is also clear that the baffled piston gives around 20 dB more output than the unbaffled piston. This is an important issue as well since the loudspeaker element might need to produce high levels of noise cancelling sound.

An active noise control system might use two independent channels or use some kind of coupled control of the two silent zones around the two ears. The crosstalk is an all-important parameter for this; if one loudspeaker gives a strong contribution both to its own ear and to the ear across the head, the system might have to use a coupled control. On the other hand, if the crosstalk is very low, independent channels should be perfectly adequate. Figs. 8 and 9 show the magnitude of the crosstalk for the baffled and the unbaffled piston, respectively. The crosstalk was calculated simply by comparing the TF magnitude for two receiver positions 20 cm apart, on-axis. This corresponds approximately to the distance between the ears if one takes into account the longer sound path around the head. In reality, the crosstalk might be different than this since the head does have some, if weak, shadowing effect. At the same time, the other loudspeaker might act as a reflector and thus increase the crosstalk magnitude. Ignoring these effects as a first approximation, it can be seen that the crosstalk for the baffled piston, in Fig. 8, is quite much stronger than for the unbaffled piston, in Fig. 9. This is especially true if the closest ear is very close to the loudspeaker. At high frequencies, the unbaffled and the baffled piston behave identically.

The crosstalk also has important consequences in binaural sound reproduction over loudspeakers. So-called crosstalk cancellation filters are needed if the crosstalk is strong, and such filters are quite sensitive to the listening person's head size and positioning of the head. Consequently, a reproduction system using closely mounted unbaffled loudspeakers would not need any cross-talk cancellation filter.

Conclusions

The near-field of an unbaffled loudspeaker has been studied and compared with that of a baffled loudspeaker. An edge diffraction model was used for the numerical examples. It was shown that, as expected, the dipolar nature of the unbaffled loudspeaker element gives a less homogeneous nearfield, but with a sigificantly lower crosstalk

between two ear positions than a baffled loudspeaker would have given. The output of the unbaffled loudspeaker might be 20 dB lower than the baffled loudspeaker around 100 Hz, or 14 dB lower than a loudspeaker in a small enclosure.

The calculation model used gave an analytic expression for the first-order diffraction and an approximate rest function replacing the higher orders lead to a very efficient numerical method.

References

[1] Silence International A/S, www.silence.no.

[2] U.P. Svensson, R. I. Fred, J. Vanderkooy, "Analytic secondary source model of edge diffraction impulse responses," J. Acoust. Soc., **106**, 2331-2344 (1999).

[3] H. Medwin, E. Childs, G. M. Jebsen, "Impulse studies of double diffraction: A discrete Huygens interpretation," J. Acoust. Soc. Am. **72**, 1005-1013 (1982).

[4] R. S. Keiffer, J. C. Novarini, "A time domain rough surface scattering model based on wedge diffraction: Application to low-frequency backscattering from two-dimensional sea surfaces," J. Acoust. Soc. Am. **107**, 27-39 (2000)

[5] M. A. Biot, I. Tolstoy, "Formulation of wave propagation in infinite media by normal coordinates with an application to diffraction," J. Acoust. Soc. Am. **29**, 381-391 (1957).

[6] A. Sæbø, " Crosstalk cancelled binaural reproduction and the effect of reflections," Ph.D. thesis (in preparation), Norwegian University of Science and Technology, Dept. of Telecommunications, Trondheim (2001).